Université de Provence (Aix–Marseille I)
Physique et Science de la matière
Observatoire Astronomique de Marseille–Provence,
Laboratoire d' Astrophysique de Marseille
FRANCE
and
University of Patras
Department of Mathematics
Division of Applied Analysis
GREECE

A Study of Hamiltonian Dynamics with Applications to Models of Barred Galaxies

Ph. D. Thesis

Athanasios MANOS

Marseille – Patras
2008

To my parents
and
in memory of one
of my best friends,
Thanasis Tserpes.

“Parable.–Those thinkers in whom
all stars move in cyclic orbits are not the most profound:
whoever looks into himself as into vast space
and carries galaxies in himself also
knows how irregular all galaxies are;
they lead into the chaos and labyrinth of existence.”

Joyful Science
Frederick Nietzsche

This thesis has been approved and judged by the:

1. **ATHANASSOULA, Evangelie** (Supervisor)
   Astronome au Laboratoire d'Astrophysique de Marseille,
   Observatoire Astronomique de Marseille–Provence,
   Université Aix–Marseille I

2. **BOUNTIS, Anastasios** (Supervisor)
   Professor of the Department of Mathematics,
   University of Patras

3. **AMRAM, Philippe** (member of jury of the thesis)
   Professeur au Laboratoire d'Astrophysique de Marseille (CNRS),
   Université Aix–Marseille I

4. **PNEVMATIKOS, Spyros** (member of jury of the thesis)
   Professor of the Department of Mathematics,
   University of Patras

AKNOWLEDGEMENTS

In attempting to summarize these last few years, during which this thesis was written, I should first declare that I feel quite fortunate that I had the chance to do this under the common supervision of scientists of the *University of Aix Provence I* (France) and the *University of Patras* (Greece). Without exaggeration and beyond the formality of this kind of acknowledgement, I wish to gratefully thank both my supervisors, Professor Tassos Bountis and Professor Evangelie Athanassoula who prompted me to begin this project and put much effort to help me overtake several obstacles that appeared during these years.

Professor Tassos Bountis introduced me to the field of Nonlinear Dynamics, Chaos theory and Complexity and taught me much of what I know, not only through undergraduate and graduate courses that he taught but also in the several summer schools and conferences that I had the opportunity to attend. He is for me the teacher that initially linked my "popular" scientific interests about chaos and astronomy to actual mathematical and physical research interests and inspired me in following these tracks. I thank him for his untiring patience in answering all my questions on these topics and for his understanding in general, during all these years.

My sincere thanks also go to Professor Evangelie Athanassoula who, after a first visit for collaboration within a *Marie Curie Fellowship* program, proposed that we should continue working together towards a Ph.D. thesis. Her extensive expertise in Astronomy and Galactic Dynamics, was a great help in my efforts to learn and work on the fundamental problem I was always interested in, i.e. the detailed study of the presence of *chaos in the galaxies.* I learned a lot from her during these years and she was always available for all my persistent and sometimes "naive" questions.

I also thank a lot the two members of the judging committee: Professor Spyros Pnevmatikos for all he taught me about Hamiltonian systems while I was in Patras and Professor Philippe Amram for his support and many helpful remarks and comments about the content of my thesis.

I would also like to thank particularly Dr. Charalampos Skokos for all the fruitful scientific discussions and collaborations that we have had during this period. He was kind enough to help me solve a lot of my problems, when I was starting my thesis and later worked closely with me in applying the SALI and GALI methods that he had developed with the Nonlinear Dynamics group of the University of Patras. I express my thanks also the "Institut de Mécanique Céleste et de Calcul des Éphémérides" (IMCCE) of the Observatory of Paris which hosted me in June 2006, when I collaborated with Dr. Ch. Skokos.

The computing assistance offered to me repeatedly by the computer administrator of our group, Jean–Charles Lambert, was truly significant. He taught me a lot about improving my codes and managing larger clusters of computers. I can't recall any single computing or system problem that he wasn't able to solve almost as soon as it appeared. Dr. Chris Antonopoulos has also helped me a lot at the University of Patras, especially when I was starting my Master's thesis. I would like to thank him for our discussions about programming and several numerical analysis issues that he showed me how to deal with. The postgraduate student Michael Epitropakis of the Division of Computational Mathematics at Patras is also acknowledged here for helping us set up a mini computer cluster in their laboratory. Finally, I wish to thank the postgraduate student of Mathematics Eleni Christodoulidi for our collaboration and many discussions at the University of Patras and Dr. Emmanuel Nezri for his help in the amelioration of the french text of the thesis.

The assistance of my parents, Stavroula and Leftheris, during all these years has been remarkable. They supported my efforts by all their means. I want to reassure them that I appreciate greatly that they helped me do something that I love without trying to influence my ideals and believes in life and in my studies. I also want to thank my sister Dafni for her understanding throughout this period.

I am especially grateful to my friends, researchers and office mates (in a random order): Mercè Romero–Gómez, Inma Martínez–Valpuesta, Izbeth Hernández and Rubens Machado, close allies and colleagues in my life in Marseille, helping me overcome several technical everyday office and research issues and assisting me with several administrative issues that they arranged on my behalf when I was away from Marseille. I similarly thank Professor Albert Bosma of the Laboratoire d'Astrophysique de Marseille (LAM) and the postgraduate students and colleagues of the Department of Mathematics, Grigoris Protsonis and Stavros Anastasiou, for helping me continuously fight with the bureaucracy at Marseille and Patras respectively. Special thanks go to my friend Ben Loeillet who hosted me in his home during one of my visits in Marseille. I shouldn't forget to mention the hospitality and kindliness of Avgeris Fakkiris and Katerina Fakkiri. We really spent nice time together in Aix–en–Provence and in music nights they organized several times. There were also plenty of other friends that helped and supported me in many ways during all these years, I thank them too.

Finally, I feel I should say a few words about Dr. Angelos Missiriotis who passed away recently. He was one of the first persons I met in Marseille and the one who initially oriented me, not only in the new (at that time) environment in Marseille but also in the new scientific field that I was about to enter. His advice was always most useful for me and I will always remember our discussions and times we shared together in either sharing a house, in conferences or playing music and climbing.

A close and important friend that I will always remember and I wish to acknowledge is Thanasis Tserpes. Thanasis was an excellent friend and passed away when I was about to start my Ph.D. thesis. He was one of the most interesting, sharp and talented persons I have ever met. A great musician with clear and strict criterion. There were often times that our discussions about music were lasting all night long and many hours spent playing music together. I will not forget one of his greatest wills and goals: to keep improving our musical sense and knowledge in order to compose and play the kind and quality of music (in the higher possible level) that makes us become better and better in all (if possible) aspects of our interests as time passes.

Besides the scientific part of the thesis, I would like to end with some remarks about the whole experience in working at the two above institutes. It was for me a great chance to live and work with two different groups possessing different ways of thinking: The mathematical point of view of the Department of Mathematics of the University of Patras and the physical point of view of the Department of Astronomy of the University of Marseille. Their combination made me often more flexible in approaching a problem and reaching its solution. Living in France and particularly in Marseille part of this period gave me the opportunity to learn a different way of life and mentality. Making new friendships from all over the world was also a great benefit. Last but not least, since Marseille and Patras are both ports and both Mediterranean cities, I was able to live near the third love of my life, after science and music, which is the sea.

Part of this thesis was supported by the "Karatheodory" graduate student fellowship No B395 of the University of Patras (Principal Investigator: Associate Professor V. Papageorgiou) and other research funding offered to me by Professor T. Bountis. During my visits in Marseille, travel and accommodation funds were also provided by the Marie Curie fellowship No HPMT–CT–2001-00338. Visits between the team members were partially funded by the region PACA. This work was partially supported by grant ANR–06–BLAN–0172.

Athanasios MANOS

Marseille–Patras
October, 2008

CONTENTS

- **Papers in Refereed International Journals before the thesis**

  1. C. Efthymiopoulos, T. Bountis and **T. Manos**, “Explicit Construction of First Integrals with Quasi – monomial terms from the Painlevé Series”, 2004, *Regular and Chaotic Dynamics*, Vol. 9, 3, 385 – 398.

- **Papers in Refereed International Journals related to the thesis**

  1. **T. Manos**, Ch. Skokos, E. Athanassoula and T. Bountis, “Studying the global dynamics of conservative dynamical systems using the SALI chaos detection method”, 2006. Nonlinear Phenomena in Complex Systems, vol. 11, 2, 171 – 176.
  2. T. Bountis, **T. Manos** and H. Christodoulidi, “Application of the GALI Method to Localization Dynamics in Nonlinear Systems”, 2008, *Journal of Computational and Applied Mathematics*, (in press).
  3. **T. Manos** and E. Athanassoula, “Exploring the distribution of regular and chaotic orbits in barred galaxies I.”, 2008, *MNRAS*, (preprint to be submitted for publication).
  4. E. Athanassoula and **T. Manos**, “Exploring the distribution of regular and chaotic orbits in barred galaxies II.”, 2008, *MNRAS*, preprint to be submitted for publication).

- **Papers in International Conference Proceedings before the thesis**

  1. Ch. Antonopoulos, **T. Manos** and Ch. Skokos, “SALI: An Efficient Indicator of Chaos with Application to 2 and 3 Degrees of Freedom Hamiltonian Systems”, 2004. In Proceedings of the 1$^{\text{st}}$ International Conference “From Scientific Computing to Computational Engineering”, 1$^{\text{st}}$ IC – SCCE, ed. D.T. Tsahalis, *Patras Univ. Press*, Vol. III, (electronic version).
  2. C. Efthymiopoulos, T. Bountis and **T. Manos**, “Explicit Algorithmic Construction of Polynomial First Integrals from the Painlevé - Laurent Series”, 2004. In Proceedings of the 1$^{\text{st}}$ International Conference “From Scientific Computing to Computational Engineering”, 1$^{\text{st}}$ IC – SCCE, ed. D.T. Tsahalis, *Patras Univ. Press*, Vol. III, (electronic version).

- **Papers in International Conference Proceedings related to the thesis**

  1. **T. Manos** and E. Athanassoula, “Detecting chaotic and ordered motion in barred galaxies”, 2005. In Proceedings of the SF2A-2005: Semaine de l’Astrophysique Francaise, eds. F. Casoli, T. Contini, J. M. Hameury and L. Pagani, *EDP-Sciences, Conference Series*, 631 – 632.
  2. **T. Manos** and E. Athanassoula, “Chaos and the dynamical evolution of barred galaxies”, 2005. In Proceedings of the 5th International Cosmology Conference: The Fabulous destiny of galaxies: Bridging past and present, eds. V. Le Brun, A. Mazure, S. Arnouts, D. Burgarella, *Frontier Group*, 541 – 542.
  3. **T. Manos** and E. Athanassoula, “Barred Galaxies: Studying the Chaotic and Ordered Nature of Orbits”, 2006. In Proceedings of the AIP Conference Proceedings, Recent Advances in Astronomy and Astrophysics: 7th International Conference of the Hellenic Astronomical Society, ed. N. Solomos, Vol. 848, 662 – 668.

4. **T. Manos**, Ch. Skokos and T. Bountis, "Application of the Generalized Alignment Index (GALI) method to the dynamics of multi–dimensional symplectic maps", 2008. In Proceedings of the International Conference *Chaos, Complexity and Transport: Theory and Applications,*, eds. C. Chandre, X. Leoncini and G. Zaslavsky, *World Scientific Publishing*, 356 – 364.
5. **T. Manos**, Ch. Skokos and T. Bountis, "Global dynamics of coupled standard maps", 2008. In Proceedings of the International Conference *Chaos in Galaxies*, eds. G. Contopoulos and P. Patsis, *Springer–Verlag* (in press).
6. **T. Manos** and E. Athanassoula, "Dynamical study of 2D and 3D barred galaxy models", 2008. In Proceedings of the International Conference *Chaos in Galaxies*, eds. G. Contopoulos and P. Patsis, *Springer–Verlag* (in press).

Abstract

This thesis addresses questions and presents results that require the combination of two disciplines: on the one hand, we wish to develop and understand fundamental tools of Hamiltonian systems and, on the other hand, we plan to use them to study the dynamics of certain basic models of barred galaxies.

For this reason we shall start by investigating some important dynamical phenomena concerning the stability of periodic oscillations in N degree of freedom Hamiltonian systems and N coupled symplectic maps. Furthermore, we will extend our study to the vicinity of such motions and analyze quasiperiodic orbits aiming to find conditions under which they break down and chaotic behavior settles in. This will be accomplished by computing the GALI indices along every reference orbit. If the central periodic orbit is stable, the GALI method can be used to determine the dimensionality of the tori surrounding this orbit in the $2N$–dimensional phase space. Furthermore, it can be applied to detect regimes where such tori cease to exist and most choices of initial conditions lead to chaotic orbits. We shall do this by studying a system of N coupled standard maps, searching for stable periodic motion surrounded by of tori beyond which there is chaos. In order to achieve this goal, we choose two different types of initial conditions: a) localized in real space, exciting a "small" number of particles (called a breather) and studying their regular or chaotic motion and b) localized in Fourier space (called q–breather), exciting a "small" number of normal modes and studying recurrence phenomena.

We then turn to the detailed study of orbital star motion in galactic potentials which constitutes a fundamental aspect of dynamical astronomy and is the second major theme of this thesis. Starting with models that describe galaxies and their star motion, it is well–known that the analysis of periodic orbits, and their stability, can provide very useful information about galaxy evolution. Stable periodic orbits are associated with regular motion, since they are surrounded by quasi–periodic tori. A fundamental question that arises therefore is what is the extent of these stability regions? Another recent result in galactic dynamics is that there are also several chaotic orbits that can support galaxy features, like rotating bars. The phenomenon of "stickiness" ("sticky" orbits) is also very common in this kind of Hamiltonian systems, i.e. orbits that their chaotic nature takes a long time to be revealed.

Several new chaos detection methods have been introduced and applied in the last years for the detection of chaotic and regular motion in galaxy models, either by studying the behavior of deviation vectors or by analyzing time series constructed by the coordinates of each orbit. In this thesis, we shall focus on a Ferrers' barred galaxy model and study not only the distinction between regular, sticky and chaotic solutions but also the significance of these findings over time interval that have a physical meaning, i.e. roughly a Hubble time.

To accomplish this we will use the method Generalized Alignment Indexes (GALI) for the distinction between the chaotic and regular motion as well as new ways of interpreting Fourier spectra and momentum distribution. Combining all these we achieve two goals: First, we are able to detect fast and efficiently the true nature of the orbits and second, we can distinguish between chaotic orbits with different types of orbital diffusion in real space. We find that there are chaotic orbits that behave in a "regular–like" manner for long enough times that their characteristics are not yet revealed from an observational point of view. Finally, we present some results concerning several regular orbits with regard to their orbital complexity, in terms of torus dimensionality.

Résumé

Cette thèse aborde des questions et présente de résultats qui exigent la combinaison des deux disciplines: d'une part, nous souhaitons comprendre et développer des outils fondamentaux des systèmes hamiltoniens et d' autre part nous envisageons de les utiliser pour étudier la dynamique de certains modèles de galaxies barrées.

Pour cette raison, nous allons commencer par étudier d'importants phénomènes dynamiques concernant la stabilité des oscillations périodiques dans les systèmes hamiltoniens à N degrés de liberté ainsi que les applications N–symplectiques couplées. Ensuite, nous allons étendre notre travail au voisinage de ces regions et analyser les orbites quasiperiodiques pour trouver des conditions dans lesquelles ces phénomènes disparaissent et pour lesquelles le comportement devient chaotique. Ceci sera effectué, en calculant les indices de GALI le long de chaque orbite de référence. Si l'orbite est périodique stable, la méthode GALI peut être utilisée pour déterminer la dimensionnalité du tore autour de cette orbite dans l'espace des phases á $2N$–dimensions. Cette méthode peut alors être appliqué pour détecter les régimes où ces tores n'existent plus et où la plupart des choix de conditions initiales conduisent à des orbites chaotiques. Nous étudierons donc un système de N–applications standard couplées et en cherchant des orbites périodiques stables limitées par le tore au–delà duquel le chaos apparait. Afin d' atteindre cet objectif, nous choisissons deux types de conditions initiales : a) localisées dans l' espace réel, en excitant un "petit" nombre de particules (appelé "breathers") et en étudiant leur mouvement régulier ou chaotique et b) localisées dans l' espace de Fourier (appelé q–"breather"), en excitant maintenant un "petit" nombre de modes normaux et en étudiant les phénomènes récurrents.

Nous passons ensuite au second thème principal de cette thèse en étudiant en détails un problème fondamental de dynamique astrophysique : les orbites d'étoiles dans le potentiel galactique. À partir de modèles qui décrivent des galaxies et leur mouvement d'étoiles, il est bien - connu que l' analyse des orbites périodiques et leur stabilité, peut fournir des informations très utiles sur l'évolution des galaxies. Les orbites périodiques stable sont associées á un mouvement régulier, puisqu' ils sont entourés d'un tore quasi–périodique. Une question fondamentale qui se pose alors est l'étendue de ces régions de stabilité. Un autre résultat en dynamique galactique est la présence de plusieurs orbites chaotiques comportant des caractéristiques de galaxies, comme la rotation de barre. Le phénomène de "stickiness"(orbites "collantes") est également très fréquent dans ce genre de systèmes Hamiltoniens, c' est-à-dire que leurs orbites révèlent leur nature chaotiques lentement.

Plusieurs nouvelles méthodes de détection du chaos ont été introduites et appliquées au cours des dernières années pour la détection de mouvement chaotique ou régulier dans des modèles de galaxies, soit en étudiant la comportement des vecteurs deviation ou par l' analyse de séries chronologiques construites par les coordonnées de chaque orbite. Dans cette thèse, nous nous consacrons au modèle de galaxies barreé de Ferrers et nous étudions non seulement la distinction entre les solutions régulières, "sticky" ou chaotiques, mais aussi l' importance de ces conclusions sur un intervalle de temps ayant un sens physique, c'est-à-dire environ un temps de Hubble.

Pour accomplir cela, nous utiliserons la méthode de "Generalized Alignment Indexes" (GALI) pour la distinction entre mouvement chaotique ou régulier ainsi que de nouvelles manières d' interprétation des spectres de Fourier et de la distribution de vitesse ou de quantité de mouvement. La combinaison de tout cela nous permet d'atteindre deux objectifs : Tout d' abord, nous pouvons détecter rapidement et efficacement la véritable nature des orbites et d' autre part, nous pouvons distinguer entre orbites chaotiques de diffusion orbitale dans l'espace réel différente. Nous avons montré qu' il existe des orbites chaotiques se comportant de manière "réguliere" suffisamment longtemps pour que leur caractéristiques n' aient pas encore été révélées du point de vue observa-

tionnel. Nous donnons enfin quelques résultats sur des orbites régulières concernant leur complexité orbitale, en termes la dimension du tore.

Περίληψη

Η παρούσα διατριβή θέτει προβληματισμούς και παρουσιάζει αποτελέσματα που απαιτούν συνδυασμό δύο επιστημονικών κλάδων και κατευθύνσεων. Αφ΄ ενός επιθυμούμε να κατανοήσουμε και να αναπτύξουμε τα θεμελιώδη εργαλεία των Χαμιλτονιανών συστημάτων και αφ΄ ετέρου σκοπεύουμε να τα χρησιμοποιήσουμε, για να μελετήσουμε τη δυναμική ορισμένων βασικών μοντέλων ραβδωτών γαλαξιών.

Για τον λόγο αυτόν θα αρχίσουμε με την μελέτη μερικών σημαντικών δυναμικών φαινομένων σχετικά με τη ευστάθεια των περιοδικών ταλαντώσεων Χαμιλτονιανών συστημάτων N βαθμών ελευθερίας και N–συνδεμένων συμπλεκτικών απεικονίσεων. Επιπλέον, θα επεκτείνουμε τη μελέτη μας στην περιοχή τέτοιων κινήσεων και θα αναλύσουμε τις οργανωμένες τροχιές, στοχεύοντας να βρούμε συνθήκες κάτω από τις οποίες αυτές διαλύονται και εμφανίζεται χαοτική συμπεριφορά. Αυτό θα επιτευχθεί με τον υπολογισμό των δεικτών $GALI$ κατά μήκος κάθε τροχιάς. Εάν η κεντρική περιοδική τροχιά είναι σταθερή, η μέθοδος $GALI$ μπορεί να χρησιμοποιηθεί για να καθορίσει τη διαστατικότητα των τόρων που περιβάλλουν αυτήν την τροχιά μέσα στον $2N$–διάστατο χώρο φάσεων. Επιπλέον, μπορεί να εφαρμοστεί για να ανιχνευθέι από ποιο σημείο και μετά, παύουν να υπάρχουν οι τόροι και οι περισσότερες επιλογές των αρχικών όρων οδηγούν σε χαοτική αυμπεριφορά. Προκειμένου να επιτευχθεί αυτός ο στόχος, επιλέγουμε δύο διαφορετικούς τύπους αρχικών συνθηκών: α) εντοπισμένες στο πραγματικό χώρο, διεγείροντας έναν 'μικρό' αριθμό σωματιδίων (γνωστών ως *πνοές*) και μελετώντας την κανονική ή χαοτική κίνησή τους και β) εντοπισμένες στο χώρο *Fourier* (γνωστές ως *q–πνοές*), διεγείροντας τώρα έναν 'μικρό' αριθμό *κανονικών τρόπων ταλάντωσης* και μελετώντας *φαινόμενα επανάληπτικότητας*.

Στη συνέχεια επικεντρωνόμαστε στη λεπτομερή μελέτη της κίνησης τροχιών αστεριών σε γαλαξιακά δυναμικά που αποτελεί μια από τις θεμελιώδες πτυχές της δυναμικής αστρονομίας και αποτελεί το δεύτερο σημαντικό θέμα αυτής της διατριβής. Ξεκινώντας με μοντέλα που περιγράφουν την κίνηση αστεριών σε ενα γαλαξία, είναι γνωστό ότι η ανάλυση των περιοδικών τροχιών, και η ευστάθειά τους, είναι χρήσιμες πληροφορίες για την εξέλιξη αυτών. Οι ευστάθείς περιοδικές τροχιές συνδέονται με οργανωμένη κίνηση, δεδομένου ότι είναι κοντά σε σχεδόν–περιοδικούς τόρους. Ένα θεμελιώδες ζήτημα που προκύπτει επομένως είναι ποια είναι η έκταση αυτών των περιοχών ευστάθειας· Ένα άλλο πρόσφατο αποτέλεσμα στη γαλαξιακή δυναμική είναι ότι υπάρχουν επίσης διάφορες χαοτικές τροχιές που μπορούν να υποστηρίξουν τα χαρακτηριστικά γνωρίσματα γαλαξιών, όπως στη περίπτωση περιστρεφόμενων ράβδων. Το φαινόμενο '*stickiness*' (*κολλώδεις* τροχιές) είναι επίσης πολύ κοινό σε τέτοιου είδους Χαμιλτονιανά συστημάτα, δηλ. τροχιές των οποίων η χαοτική φύση τους καθυστερεί να αποκαλυφθεί.

Νέες μέθοδοι ανίχνευσης χάοτικής συμπεριφοράς έχουν εισαχθεί και έχουν εφαρμοστεί τα τελευταία χρόνια για τον διαχωρισμό μεταξύ της χαοτικής και κανονικής κίνησης σε μοντέλα γαλαξιών, είτε μέσω της μελέτη της συμπεριφοράς διανυσμάτων απόκλισης είτε μέσω της ανάλυσης χρονοσειρών συντεταγμένων κάθε τροχιάς. Στην παρούσα διατριβή, εστιάζουμε σε μοντέλα ραβδωτών γαλαξιών '*Ferrers*' και μελετούμε όχι μόνο τη διάκριση μεταξύ των κανονικών και χαοτικών λύσεων αλλά και της σημασίας αυτών για χρονικές περιόδους με φυσική σημασία, δηλ. διαστήματα που προσεγγίζουν μια περιόδο *Hubble*.

Για να το επιτύχουμε αυτό θα χρησιμοποιήσουμε τη γενικευμένη μέθοδο δεικτών ευθυγράμμισης $GALI$ για τη διάκριση μεταξύ χαοτικών και κανονικών τροχιών καθώς επίσης και νέους τρόπους υπολογισμού φασμάτων *Fourier* και κατανομών ταχυτήτων. Συνδυάζοντας όλα αυτά επιτύγχάνουμε δύο στόχους: Κατ΄ αρχάς, είμαστε σε θέση να ανιχνεύσουμε γρήγορα και αποτελεσματικά την αληθινή φύση των τροχιών και δεύτερον, μπορούμε να διακρίνουμε μεταξύ χαοτικών τροχιών, εκείνες που εμφανίζουν διαφορετικού τύπου διαχύση στον χώρο κίνησης. Έτσι ανακαλύπτουμε ότι υπάρχουν χαοτικές τροχιές που συμπεριφέρονται για αρκετά μεγάλους χρόνους με 'οργανωμένο–τρόπο'. Τέλος παρουσιάζουμε μερικά αποτελέσματα για οργανωμένες τροχιές, που σχετίζονται με τη διαστατικότητας των τόρων, επάνω στους οποίους πραγματοποιείται η κίνησή τους.

CHAPTER 1

INTRODUCTION

Classical chaos is by now fairly well understood in low–dimensional Hamiltonian systems. Since Poincaré proved that the 3–body gravitational system is not integrable, much insight has been gained about regular and chaotic dynamics in more general Hamiltonian systems. The essential feature of a chaotic system is its sensitivity to initial conditions. A slight change in one of its variables may result in an entirely different time evolution. A dynamical system may be *deterministic*, in the sense that its equations of motion are known, and yet its solutions may become completely unpredictable after relatively short time intervals.

Astronomy is the science that deals with the origin, evolution, composition, location and motion of all bodies and scattered matter in the universe. It includes Astrophysics, which focuses on the physical properties and structure of cosmic bodies and celestial matter and exploits the principles and methods of Physics to model astronomical systems and understand the processes taking place in them. In recent decades, a new approach has been introduced and applied to a variety of disciplines, in which dynamical systems are used as mathematical models. It is the theory of *nonlinear dynamics and chaos* and has evolved from the study of dynamical systems which behave unpredictably and exhibit complex characteristics, despite their seeming simplicity and deterministic nature. The complex behavior of such systems is attributed to their extreme of sensitivity to initial conditions, whereby two initial states differing only by a minute amount, rapidly deviate exponentially away from each other in phase space. This theory has been most fruitful in almost all fields of Physics, but it is important to recall that its first paradigms were actually deeply rooted in Astronomy and in particular in the stability of the solar system.

A large number of astronomical problems are theoretically modelled by nonlinear dynamical systems. The application of the ideas and methods of chaos and complexity to Astrophysics thus seems to be natural. Indeed, these methods have already been exploited to study systems on a vast variety of scales – from planetary satellites through pulsating stars and up to the large scale phenomena in structure of the universe. The main importance of these approaches lies in their ability to provide new analytical insights into the intricate physical processes taking place in cosmic matter, shaping the various astronomical objects and causing the prominent observable phenomena that occur in them.

Planetary systems, star clusters of various richness, galaxies and galaxy clusters and super–clusters (clusters of clusters) can be approached most directly by considering the *gravitational N–body problem* (*GNBP*). In this approach all other interactions, save the gravitational one, are neglected, and the bodies are considered to be point masses. This model is viable, at least approximately, when the distances between the bodies are much larger than their typical size and any scattered matter between the bodies has only a very small effect on the dynamics. The GNBP is one of the paradigms of classical dynamics, whose development originated in Newton's laws and through the implementation of techniques of mathematical analysis (mainly by Lagrange in his work Analytical Mechanics, published in 1788) and finally acquired a powerful abstract formulation in terms of the canonical variables of Hamiltonian Mechanics.

Hamiltonian systems, that is, dynamical systems that obey Hamilton's equations, are endowed with important conservation properties linked to symmetries of the Hamiltonian, a function that completely describes the system. This function is defined in the phase space (spanned by the generalized coordinates and momenta) and the time coordinate. A Hamiltonian system that does not explicitly depend on time, conserves phase volume and perhaps other quantities also, (such as the total energy or angular momentum), as is the case of the GNBP. Hamilton's equations consist of two ordinary differential equations (ODEs) for each of the N degrees of freedom, thus the GNBP in three–dimensional (3D) physical space yields $6N$ equations, which in general are quite formidable to solve. Of course, if there are N constants of the motion (like the energy, the angular momentum, etc.) the system may be completely integrable and even solvable in terms of known functions. Such cases, however are extremely rare and are associated with completely regular dynamics. As is very well–known today most Hamiltonian systems are not integrable and possess wide domains of chaos.

The $N = 2$ case of the GNBP is reducible to an equivalent one–body problem, known as the Kepler problem. The complete solution of this problem was first given by Johann Bernoulli in 1710, quite long before the Lagrange–Hamilton formalism was introduced. The gravitational two–body problem has been successfully applied to various astrophysical systems, e.g. the motion of planets and their satellites, as well as the dynamics of binary stars. The quest for a similar reduction for systems with $N > 2$, was immediately undertaken by several great mathematicians. The side benefit of these studies, conducted for almost two centuries, was a significant progress in mathematics (mainly in the theory of ODEs), but definite answers were found only in some very particular cases.

Attempts to treat even the simplest problem of this kind, the restricted, planar, three–body problem (where one of the bodies is so light that its gravity has no effect on the other two and all orbits are restricted on a plane) ended in a failure. All general perturbative approaches invariably led to diverging terms because of the appearance of "small divisors" in the perturbation series. The first real breakthrough came in the 1880s, when Henri Poincaré worked on the GNBP and won a prize, set by King Oscar II of Sweden. Poincaré did not provide a solution of the problem, but managed to understand why it is so hard to solve. By ingenious arguments, he showed that the orbits of the restricted three–body problem are too complicated to be described by explicit formula mathematical analysis.

In more technical terms, Poincaré showed that this system (and therefore the general GNBP) is non–integrable. He did so by introducing a novel idea, now called a Poincaré section [97], with the help of which he was able to visualize the geometry of the dynamics by means of a two–dimensional area preserving map. Remarkably, Poincaré was able to visualize such a structure without the aid of computer graphics. The non–integrability of the GNBP naturally prompted the question of the stability of the Solar system. Of course, no definite answer to this problem could be reasonably expected on the basis of Poincaré's work. Before electronic computers became available, work was largely based on perturbation theory or mean field methods. Despite all difficulties, these efforts yielded new and deep insights in the chaotic behavior of Hamiltonian systems and produced many important mathematical results after intensive work of nearly 50 years.

First and foremost among them is the celebrated KAM theorem, which has elucidated the mathematical process by which an integrable Hamiltonian system develops chaotic behavior as a result of losing its integrability, when a suitably defined control parameter (e.g. the relative size of the non–integrable perturbation to an integrable Hamiltonian) is gradually made different from zero. In particular, the crucial role of resonant tori in this process has been recognized, starting with the increasing distortion of these tori. Resonant tori become ultimately corrugated on all scales, acquiring a fractal shape that allows orbits to diffuse in the regions between the surviving non–resonant tori.

Twenty years after the formulation of the KAM theorem, Boris Chirikov suggested a diagnostic criterion for the onset of chaos in Hamiltonian systems. He studied numerically the standard map

$$\begin{aligned} I_{j+1} &= I_j + K \sin \Theta_j \\ \Theta_{j+1} &= \Theta_j + I_j \end{aligned} \tag{1.1}$$

a particular area preserving transformation of the plane onto itself, where I and Θ are "action" and "angle" variables and K is a constant. Thus (1.1) represents an excellent example of a periodically driven Hamiltonian system of one degree of freedom which is analogous to a system with $N = 2$. He showed that fully–spread chaos arises when $K > 1$ and found that this happens because resonances overlap. In addition the basic defining property of deterministic chaos (i.e. the divergence of initially nearby phase space trajectories) is quantified by the positivity of the largest Lyapunov exponent.

In Hamiltonian systems of N degrees of freedom a hierarchy of different types of chaotic motion is available [3, 2]. As the Hamiltonian system is driven farther into the chaotic regime, the motion becomes more strongly irregular, in the sense that its trajectories in phase space explore wider and wider regions. Hamiltonian dynamical systems with bounded motion may also be recurrent, i.e., their trajectories return infinitely many times arbitrarily close to the initial point. Indeed according to the famous Poincaré recurrence theorem in a chaotic region, this is true for almost all orbits and almost all points.

If every initial phase space volume (or distribution of initial conditions) eventually spreads over the whole space, then the chaotic system is said to have the property of mixing. In a globally chaotic regime, a Hamiltonian system is said to become a K–system (after Kolmogorov). This happens when all trajectories in a connected neighborhood diverge exponentially on the average and every trajectory has a positive Lyapunov exponent. One of the first Hamiltonian systems, relevant to astrophysics, which was shown to exhibit deterministic chaos was the one studied by Hénon & Heiles in 1964 [54]. They numerically investigated the orbits of a point mass (a star) in a mean field model approximating an axially symmetric galaxy. Casting the gravitational influence of all other masses into a potential of cubic polynomial type and computing the orbits of a point mass is significantly easier than a full N–body simulation, which has always been one of the primary techniques of galactic dynamics.

The question addressed in this study involved the possible existence of a third isolating integral, which would guarantee integrability in that case. The fact that the motion in the azimuthal (with respect to the symmetry axis) direction can be separated out and that total energy and angular momentum are two independent integrals of motion leaves out a 3D subspace that is accessible to the system. A third isolating (i.e., independent of the other two) integral would thus guarantee motion on a two–dimensional surface, only, which would be the tori of an integrable system. Using, therefore, a model axisymmetric potential, whose non–dimensional form

$$V(x, y) = \frac{1}{2}(x^2 + y^2) + (x^2 y - \frac{y^3}{3}) \tag{1.2}$$

clearly contains a simple higher order nonlinear part in addition to the harmonic one, Hénon and Heiles [54] integrated the Hamilton equations of motion for several values of the non–dimensional energy parameter, E.

By examining the Poincaré section in each case, they found that the system looks integrable and its trajectories lie mostly on tori as long as E is small enough. For larger values of E, however, some of the tori are destroyed and a large chaotic "sea" appears, while finally, at higher values of E, almost all tori are destroyed and chaos becomes widespread. These results largely follow the scenario set forth by the *Kolmogorov–Arnold'–Moser* (KAM)–theorem. They also settle the issue that a third integral of motion of galactic dynamics does not exist in general. The implications of these findings have since then been thoroughly investigated, primarily by George Contopoulos and his collaborators. Of course, the pioneering work of Hénon and Heiles cannot directly predict the properties of the stellar orbits and their distribution in some particular galaxy. It has, however, remained to this day a fundamental contribution to the theory of Hamiltonian dynamical systems. The Hénon and Heiles system is perhaps the simplest and most intriguing astrophysical realization of the GNBP, involving the motion of bodies in the solar system. There exists today ample theoretical evidence, based largely on series of gradually improving numerical studies, that chaos permeates the solar system and can be found essentially everywhere one looks.

The qualitative distinction between chaotic and regular motion in symplectic maps and in systems of differential equations is a fundamental problem of nonlinear dynamics. This distinction is in general, a non trivial task and becomes more difficult as the number of degrees of freedom N increases. For this reason, over the years, several methods distinguishing regular from chaotic motion in conservative dynamical systems have been proposed and applied, with varying degrees of success.

One important application of Hamiltonian systems theory concerns the dynamics of localized oscillations about stable periodic orbits. In particular, localized oscillations in one–dimensional nonlinear lattices constitute, for the past 15 years, one of the most active areas of research in Mathematical Physics. Of primary interest has been the discovery of certain exact periodic solutions in such lattices, called discrete breathers, which are exponentially localized *in real space*. It is known that when these solutions are stable, there are domains around them in phase space, where orbits oscillate quasiperiodically for very long times, even though the presence of linear dispersion is expected to lead to delocalization away from the discrete breather. How long do they stay, however, in that vicinity and what is the dimensionality of the tori on which they lie? Furthermore, how large are these regular regions and at what initial conditions (or parameter values) does chaotic behavior begin to arise?

Similar questions can also be posed about another form of localization *in Fourier space*, which has been very recently proposed as an explanation of the famous recurrence phenomena known to occur near linear normal modes of Hamiltonian lattices, since the famous studies of Fermi, Pasta and Ulam (FPU) in the early 1950s [38, 14, 40, 41]. Clearly, the interest in such localization lies in its ability to prevent wave propagation and energy equipartition expected from the theory of statistical mechanics. Our main purpose, however, in studying models of Hamiltonian systems in the form of coupled 2–D symplectic maps is two–fold: First, we establish the generality of the above phenomena, by showing that they do not occur only in lattices and second, we use this as an opportunity to test and further develop the dynamical techniques we apply to the study of barred galaxies, which is the main focus of this thesis.

Thus, we concentrate on the study of orbits of celestial bodies represented as points $(\vec{x}(t), \vec{p}(t))$ of unit mass in 6D phase space where $\vec{x}(t) = (x(t), y(t), z(t))$, $\vec{p}(t) = (p_x(t), p_y(t), p_z(t))$, are the position and momentum coordinates and t is the time. They obey Hamilton's equation of motion

$$\dot{\vec{x}}(t) = \frac{\partial H}{\partial \vec{p}(t)}, \qquad \dot{\vec{p}}(t) = -\frac{\partial H}{\partial \vec{x}(t)}, \tag{1.3}$$

where the Hamiltonian H contains, besides the kinetic part, a potential function $V(x, y, z)$

$$H = \frac{1}{2}(p_x^2 + p_y^2 + p_z^2) - \Omega_b(xp_y - yp_x) + V(x, y, z), \tag{1.4}$$

which represents the mean gravitational field of a galaxy rotating in the (x, y)–plane with angular frequency Ω_b. Our particular model contains a "bulge" component in the center, a "disc" and a "bar". Such models are referred in the literature as "barred galaxy" models. In recent years, many researchers have work in this field, obtaining many useful results about the galactic dynamics and particularly about the barred galaxies [29, 30, 27, 24, 28, 90, 9, 117] while a nice summary of all this work can be found in [25, 33].

Our primary goal in this thesis is to use the arsenal of Hamiltonian dynamics in order to estimate the role of chaos and order in barred galaxy systems described by Eq. (1.3) and (1.4). More specifically, we aim to shed new light on the general location and extent of chaotic regions in the configuration (or 3D space) x, y, z, so as to make direct comparisons between our models and N–body simulations or, even, astronomical observations. In addition, we plan to examine in what way (and how much) the relative proportions of regular and chaotic domains vary, as we change the basic parameters of the model.

We wish to emphasize that the main difficulty with distinguishing order from chaos in our systems is that our integration time cannot exceed the age of the universe. This means that we don't have the luxury to follow our solutions arbitrarily long in order to characterize them as regular or chaotic. We must therefore, develop dynamical tools that are efficient and sharp enough to differentiate between *weak and strong chaos* and divide our orbits in well defined categories which are best suited for comparison with simulations and observations.

The thesis consists of the following chapters:

- In Chapter 2, we present the preliminary notions and concepts that constitute the theoretical background of the following chapters. The fundamentals of Hamiltonian systems are described and an introduction is given about the dynamics of our barred galaxy model. We then introduce recently developed methods and tools used to distinguish order from chaos in Hamiltonian systems.

- In Chapter 3, we apply the main dynamical tool of this thesis, i.e. the Generalized Alignment Index (GALI) method, to two types of dynamics, which are related to the distinction between regular and weakly chaotic phenomena in coupled symplectic maps representing multi–dimensional Hamiltonian systems: The first type refers to quasiperiodic oscillations in the vicinity of what is known as *discrete breathers*, or exact periodic solutions, which are exponentially localized in real space. The second concerns localization in *Fourier space* and is evidenced by the persistence of quasiperiodic recurrences in the neighborhood of normal mode oscillations of nonlinear lattices, observed for example in the famous numerical experiments performed by Fermi, Pasta and Ulam (FPU) in the early 1950's. The novelty of our results is primarily to establish the *universality* of these phenomena by showing that they also arise in chains of coupled symplectic maps. The second and more important aspect of our study is to use these models as a testing ground to investigate the sensitivity of out methods in categorizing systematically different types of ordered and chaotic motions in barred galaxies.

- In Chapter 4, we turn to the most important part of the thesis and present our results on the distinction of various types of regular and chaotic motion in Ferrers' barred galaxy models using the methods of Chapters 2 and 3. First we present quantitative results about the amount of chaotic and regular motion among various barred galaxy models, depending on their different shapes. Then, we attempt to relate the information gained from our dynamical study with "real" observational data (or N–body simulations) and manage to characterize the structure of different galaxies by the specific distribution of regular and chaotic orbits they support, for different initial conditions and parameter values of the problem.

- Finally in Chapter 5, we recall all the significant results of the thesis and discuss some perspectives which we believe that future work on this topic should address qualitatively and quantitatively.

CHAPTER 2

CONCEPTS AND METHODS OF HAMILTONIAN SYSTEMS

2.1 Hamiltonian Dynamical Systems

Dynamical systems are physical, biological, economic or social entities, whose components evolve in time. They are described (see e.g. [25]) by a single state variable $\vec{x}(t) \in \mathbb{R}$ that obeys either a system of differential equations of the form

$$\dot{\mathbf{x}} = \mathbf{f}(\mathbf{x}, t), \tag{2.1}$$

if t is a continuous variable, $t \in \mathbb{R}$, $\mathbf{x}(t) = (x_1(t), x_2(t), ..., x_N(t))$ is an N–dimensional vector, and dots ($\dot{}$) denote derivatives with respect to t, i.e. $\dot{\mathbf{x}} = d\mathbf{x}/dt$. Dynamical systems are also described by maps (or mappings) of the form

$$\mathbf{x}_{n+1} = \mathbf{f}(\mathbf{x}_n) \tag{2.2}$$

if $t \in \mathbb{Z}$ is discrete $\mathbf{x}_n = (x_{n1}, x_{n2}, ..., x_{nN})$. These systems are called *smooth* if the vector function $\mathbf{f} = (f_1, f_2, ..., f_N)$ consists of $f_i \in \mathcal{C}^1(D)$, $i = 1, 2, ..., N$, that are continuous and (at least once) continuously differentiable over some domain $D \in \mathbb{R}^N$. This guarantees the existence and uniqueness of their solutions.

The above systems (2.1) and (2.2) are called deterministic if $\mathbf{f}$ is known explicitly and share many common properties. Their many similarities often allow the use of very simple maps to illustrate the properties of generic dynamical systems described by differential equations. Map calculations are much simpler and faster than the solutions of differential equations. Thus, maps have been used extensively in the last decades in order to understand chaotic dynamics and distinguish it from regular dynamics. In fact, systems of differential equations can also be represented by maps on the so–called Poincaré surfaces of section which possess many common characteristics with the original system.

Both maps and differential equations can be used to describe conservative and dissipative dynamical systems. Conservative systems preserve volume in phase space, while in dissipative systems this volume decreases on the average and the dynamics is called attracting. Non–conservative systems also exist where phase space volume generally grows as t increases and hence gives rise to expanding dynamics.

An important class of conservative dynamical system are those whose equations (2.1) are derived from a Hamiltonian function, with conjugate variables $\mathbf{q} = (q_1, q_2, ..., q_N)$ and $\mathbf{p} = (p_1, p_2, ..., p_N)$ that satisfy the equations

$$\dot{\mathbf{q}} = \frac{\partial H}{\partial \mathbf{p}}, \qquad \dot{\mathbf{p}} = -\frac{\partial H}{\partial \mathbf{q}}. \tag{2.3}$$

Every conjugate pair $(q_i, p_i), i = 1, ..., N$ constitutes one degree of freedom of the system, while the Hamiltonian function

$$H = H(\mathbf{q}, \mathbf{p}, t) \tag{2.4}$$

is generally assumed to belong to the class $H \in \mathcal{C}^2(D)$. The space of the variables $\mathbf{q}$ and $\mathbf{p}$ is called phase space. The phase space of a system of differential equations (2.1), or a map like (2.2), is N–dimensional, while that of a Hamiltonian system is $2N$–dimensional. A change of variables $(\mathbf{q}, \mathbf{p}) \to (\mathbf{q}', \mathbf{p}')$ is called canonical if the equations of motion in the new variables are also of the form (2.3). Such a transformation may be written in the form

$$\mathbf{X}' = \mathbf{F}(\mathbf{X}) \tag{2.5}$$

where $\mathbf{X} = (\mathbf{q}, \mathbf{p})$ and $\mathbf{X}' = (\mathbf{q}', \mathbf{p}')$ have $2N$ components and $\mathbf{F}$ represents $2N$ functions $(F_1, F_2, ..., F_{2N})$ in terms of which the new Hamilton's equation may by easier to solve.

Many physical problems are called autonomous, since the Hamiltonian function does not depend explicitly on time. In such cases, H is an integral of motion, equal to the energy

$$H(\mathbf{q}, \mathbf{p}) = H(\mathbf{q}_0, \mathbf{p}_0) = h \tag{2.6}$$

where $(\mathbf{q}_0, \mathbf{p}_0)$ are the initial condition of the orbit.

A linear canonical transformation can be written in the form

$$\mathbf{X}'^T = M\mathbf{X}^T \tag{2.7}$$

where $\mathbf{X}^T$ is a column vector and M is a $2N \times 2N$ symplectic matrix, i.e. a matrix that satisfies the condition

$$M^T \Omega M = \Omega \tag{2.8}$$

where Ω is the $2N \times 2N$ matrix

$$\Omega = \begin{bmatrix} 0 & I_N \\ -I_N & 0 \end{bmatrix}, \tag{2.9}$$

with I_N the $N \times N$ unit matrix and $(^T)$ denote the transpose matrix. A nonlinear canonical transformation is called symplectic if the Jacobian matrix

$$DF = (\frac{\partial F_i}{\partial X_j}) \tag{2.10}$$

has the symplectic property.

Hamiltonian systems generate symplectic maps on Poincaré surfaces of section, which are very useful because they are much faster to compute than Hamiltonian systems. It can be easily shown that 2–dimensional (2D) maps which are area preserving also have the symplectic property and represent excellent models for analyzing the dynamics of 2–degree–of–freedom (2DOF) Hamiltonian systems. However, 4D maps, or maps of higher dimensions, may not be symplectic, even if they are volume preserving.

2.1.1 Properties of phase space motion in continuous time

Let us consider the equations of motion given by equations (2.3). Associated with these equations are $2N$ constants of motion that are the initial coordinates and momenta in the N degrees of freedom. These uniquely determine the subsequence motion of a point through a $2N$–dimensional space. Let us assume that we can solve equations (2.3) for $\mathbf{q}$ and $\mathbf{p}$ as functions of time. This means that we can follow the trajectories from an initial time t_1, corresponding to initial coordinates $\mathbf{q}_1$ and $\mathbf{p}_1$, to some other values $\mathbf{q}_2$ and $\mathbf{p}_2$ at a later time t_2. We call this ($\mathbf{q}$,$\mathbf{p}$) the *phase space* of the system (see e.g. [70]). The following important properties of this space must be obeyed at all times:

1. Trajectories in phase space *do not intersect* at any given instant of time. This is evident from the fact that the initial conditions uniquely determine the subsequent motion and is true for all time, if the system is autonomous. If the Hamiltonian does depend on time, the trajectories in phase space cannot cross in phase space at the same time, but may pass by the same $(\mathbf{q},\mathbf{p})$–point at different times.

2. A boundary in phase space C_1, which bounds a group of initial conditions at $t = t_1$ transforms into a boundary C_2 at t_2, which bounds the same group of initial conditions. This property follows directly from the one above, since any motion inside the boundary may approach the boundary, but not cross it, as this would mean its intersection with one of the orbits that continuously form the boundary. This property has far–reaching consequences in that the motion of a large group of initial conditions can be followed by monitoring a much smaller class of initial conditions lying on the boundary.

3. Consider an ensemble of initial conditions each representing a possible state of the system. We express the probability (or density distribution) of a given ensemble of system points in phase space as
$$\tau = \tau(\mathbf{p}, \mathbf{q}, t). \tag{2.11}$$
If we normalize τ such that[1]
$$\int_{\text{all space}} \tau \prod_i dp_i dq_i = 1, \tag{2.12}$$
then $dP = \tau \prod_i dp_i dq_i$ is the joint probability that at time t, the ensemble has an initial condition associated with the i^{th} coordinates, with position between q_i and $q_i + dq_i$ and momentum between p_i and $p_i + dp + i$. The rate of change of the number of phase points, $dP = \tau dV$, within the infinitesimal phase space volume
$$dV = \prod_i dp_i dq_i, \tag{2.13}$$
is obtained from the continuity equation
$$\frac{\partial \tau dV}{\partial t} + \sum_{i=1}^{n} [\frac{\partial}{\partial p_i}(\tau dV \dot{p}_i) + \frac{\partial}{\partial q_i}(\tau dV \dot{q}_i)] = 0, \tag{2.14}$$
where by, dividing out the volume dV, we obtain the rate of change of density at a fixed position in phase space
$$\frac{\partial \tau}{\partial t} + \sum_{i=1}^{n} [\dot{p}_i \frac{\partial \tau}{\partial p_i} + \tau \frac{\partial \dot{p}_i}{\partial p_i} + \dot{q}_i \frac{\partial \tau}{\partial q_i} + \tau \frac{\partial \dot{q}_i}{\partial q_i}] = 0. \tag{2.15}$$

---

[1] This normalization cannot be performed if the phase space is infinite, but is not essential.

From Hamilton's equations (2.3) for $\dot{p}_i$ and $\dot{q}_i$ the second and fourth terms of the summation cancel yielding

$$\sum_i (\dot{p}_i \frac{\partial \tau}{\partial p_i} + \dot{q}_i \frac{\partial \tau}{\partial q_i}) + \frac{\partial \tau}{\partial t} = 0. \tag{2.16}$$

which is a statement of the *incompressibility* of the flow in phase space. This result, known as Liouville's theorem, is a powerful tool for studying the dynamics of Hamiltonian systems.

Integral Invariants. Because of the above properties, the phase space representation offers considerable simplifications in treating dynamical problems. In particular, it follows immediately from equation (2.16) that

$$\int \prod_i dp_i dq_i \tag{2.17}$$

is an invariant of the motion, where the $2N$–dimensional integral is evaluated at a fixed time t. A hierarchy of such integral invariants, with successive members of increasing dimensionality in the phase space, was first studied by Poincaré (1892) [97]. A general derivation of these invariants can be found in Whittaker (1964) [127]. They are fundamental to the theory of Hamiltonian flows and constitute the basis of the Classical Mechanics as described by Arnol'd (1979) [6]. Let us examine the first member of that hierarchy [of which (2.17) is the N^{th} and final member]

$$\int \int \sum_i dp_i dq_i = \text{const.} \tag{2.18}$$

where the integral is over a two–dimensional surface in phase space at a fixed time t.

If we apply Stokes' theorem to equation (2.19), we obtain the invariant

$$\oint \sum_i p_i dq_i = \text{const.} \tag{2.19}$$

where the integration is now over a closed path in phase space at a fixed time t and is known as a relative integral invariant of the system. In general, the application of Stokes' theorem transforms an integral invariant over an arbitrary domain into a relative invariant over a closed domain and demonstrates how volume conservation in phase space implies area conservation on some chosen (q_i, p_i) surface of section.

2.1.2 Properties of phase space motion in discrete time

Let us define a $2n \times 2n$ matrix M (whose entries may be real or complex) as *symplectic* if it satisfies the condition

$$M^T \Omega M = \Omega\,. \tag{2.20}$$

where Ω is matrix 2.9. Note that Ω has determinant $+1$ and has an inverse given by $\Omega^{-1} = -\Omega$, i.e. is orthonormal.

Hamiltonian systems can be described by *symplectic maps* as follows. If we consider a mapping $\mathbb{R}^{2n} \to \mathbb{R}^{2n}$

$$\begin{aligned} x_i' &= f_{x_i}(x_i, y_i) \\ y_i' &= f_{y_i}(x_i, y_i) \end{aligned} \tag{2.21}$$

with $i = 1, ..., n$ and take $\mathbf{z} \in \mathbb{R}^{2n}$ with $z_{2i-1} = x_i$ and $z_{2i} = y_i$, (2.21) can be written as

$$\mathbf{z}' = \mathbf{f}(\mathbf{z}). \tag{2.22}$$

A map of this form is called symplectic, if the Jacobian matrix $J = \{J_{ij}\}$, with elements

$$J_{ij} = \frac{\partial f_i}{\partial z_j}, \tag{2.23}$$

and $i, j \in 1, ..., 2n$ is symplectic.

A symplectic map can describe the motion of dynamical system in discrete time steps that correspond to successive iterations

$$\mathbf{z}^{(n)} = \underbrace{f \circ ... \circ f}_{n\ times}(\mathbf{z}) = f^{(n)}(\mathbf{z}) \tag{2.24}$$

where n denotes these steps. The sequence of points $\mathbf{z}^{(n)}$, generated by the values of $\mathbf{z}$ as initial conditions is called a *trajectory* of the mapping. Stated otherwise, (2.24), yields the n^{th} iterate of the map starting from an initial point $z_0 = z$.

If it so happens that the m–th iterate of the map coincides with initial point, we call the sequence of points produced, i.e. $\hat{z}_1, \hat{z}_2, ..., \hat{z}_m$, a periodic orbit of the map with period m. If $m = 1$ we obtain the so–called fixed points of the map f, while any period m–orbit may be considered as a fixed point of the map f^m.

The next most important concept concerns the (linear) stability of these points, i.e. their response under infinitesimally small perturbations. Let us consider such a perturbation of a fixed point $\mathbf{z} = \hat{\mathbf{z}} + \mathbf{u}$. Keeping up to linear terms in $\mathbf{u}$, we obtain from (2.22), $\mathbf{u}' = J(\hat{\mathbf{z}})\mathbf{u}$, where J is the Jacobian matrix evaluated at the fixed point $\mathbf{z} = \hat{\mathbf{z}}$. This point will therefore be called stable if *no eigenvalue* λ of J has $|\lambda| > 1$. Regarding periodic orbits with period T, i.e. $\hat{\mathbf{z}} = \hat{\mathbf{z}}(t) = \hat{\mathbf{z}}(t + T)$, we know from Floquet theory that their (linear) stability is studied by solving the associated linearized problem $\mathbf{u}' = J(\hat{\mathbf{z}})\mathbf{u}$ as follows: First, we obtain a fundamental matrix of linearly independent solutions of the equation, $\Phi(t)$, with $\Phi(0) = I$, and form the so–called monodromy matrix $M = \Phi(T)$ [16].

Due to the symplectic condition (2.20) and due to the fact that the coefficients of M are real, the eigenvalues of the matrix M have the following properties: if λ is an eigenvalue then $1/\lambda$ is also an eigenvalue, and if λ is an eigenvalue, the complex conjugate λ^* is also an eigenvalue. These properties show that the eigenvalues $\lambda = 1$ and $\lambda = -1$ are always double eigenvalues and that complex eigenvalues with modulus not equal to 1 always appear in quartets. When all the eigenvalues are on the unit circle the corresponding periodic orbits is stable. If there exist eigenvalues not on the unit circle the periodic orbit is unstable. The stability of periodic orbits of Hamiltonian systems and symplectic maps has been studied by several authors, e.g. [53, 49, 57, 105]

2.1.3 Constants of the motion and integrability

The most general definition of integrability is given in terms of the *integrals of motion* (or *constants of motion*)[2]. A function $I(\mathbf{x}, \mathbf{y}, t)$ in a Hamiltonian system is called an *integral of motion* [25] if it

---

[2] Some authors (e.g. Binney and Tremaine, 1987 [15]) distinguish between *constants* of motion and *integrals* of motion. In a *autonomous* Hamiltonian, a constant of motion is a function of $\mathbf{x}, \mathbf{y}$ and t, that remains constant in time, while an integral of motion is a function of the *phase–space variables* only, i.e. $I(\mathbf{x}, \mathbf{y})$, that remains constant in time.

remains constant along any orbit, i.e. its total derivative is zero

$$\frac{dI}{dt} = \frac{\partial I}{\partial \mathbf{x}}\frac{\partial \mathbf{x}}{\partial t} + \frac{\partial I}{\partial \mathbf{y}}\frac{\partial \mathbf{y}}{\partial t} + \frac{\partial I}{\partial t} = \frac{\partial I}{\partial \mathbf{x}}\frac{\partial H}{\partial \mathbf{y}} - \frac{\partial I}{\partial \mathbf{y}}\frac{\partial H}{\partial \mathbf{x}} + \frac{\partial I}{\partial t} = 0 \tag{2.25}$$

where a summation is implied over conjugate variables. The quantity

$$[I, H] = \frac{\partial I}{\partial \mathbf{x}}\frac{\partial H}{\partial \mathbf{y}} - \frac{\partial I}{\partial \mathbf{y}}\frac{\partial H}{\partial \mathbf{x}} = \sum_{i=1}^{N}(\frac{\partial I}{\partial x_i}\frac{\partial H}{\partial y_i} - \frac{\partial I}{\partial y_i}\frac{\partial H}{\partial x_i}) \tag{2.26}$$

is called the *Poisson bracket* between the functions I and H.

From equation (2.25), we find that an integral of motion I satisfies the equation

$$[I, H] + \frac{\partial I}{\partial t} = 0. \tag{2.27}$$

The equations of motion (2.3), are the corresponding system to the partial differential equation

$$\frac{df}{dt} = \frac{\partial f}{\partial \mathbf{x}}\frac{\partial H}{\partial \mathbf{y}} - \frac{\partial f}{\partial \mathbf{y}}\frac{\partial H}{\partial \mathbf{x}} + \frac{\partial f}{\partial t} = 0 \tag{2.28}$$

This equation is called the “collisionless Boltzmann equation” in Stellar Dynamics [15]. In the case of 3 degrees of freedom the phase space is called μ–space and it has 6 dimensions. In the case of N particles the phase space is $6N$–dimensional (Γ–space) and the equation (2.28) is called Liouville’s equation.

In the case of a system of N degrees of freedom we may consider (2.28) as representing a flow of an incompressible fluid in $2N$ dimensions. If we write

$$f = \frac{dn}{dV}, \tag{2.29}$$

where dn is the number of particles within a volume dV, the number dn does not change in the course of time thus the volume dV also remains constant,

$$dV = dv_0. \tag{2.30}$$

Thus, (2.28) represents the conservation of volumes in phase space.

If the equations (2.3) have k and only k independent integrals of motion $I_1, I_2, ..., I_k (k \leq N)$ then the most general solution of (2.28) is an arbitrary function of these integrals

$$f = f(I_1, I_2, ..., I_k) \tag{2.31}$$

or

$$f = f(\mathbf{I}). \tag{2.32}$$

If $k = N$ (number of degrees of freedom) then the system is called integrable. In the particular case that H is time independent, an integral I satisfies the equation

$$[I, H] = 0. \tag{2.33}$$

If I_i are a set of integrals of motion, we say that they are *in involution* if

$$[I_k, I_m] = 0, \tag{2.34}$$

for all k and m.

An autonomous Hamiltonian H is called *Liouville integrable* if it has N independent integrals in involution (Arnol'd 1978 [6]). It is important to recall, however, that among all Hamiltonian systems, very few have been proved to be integrable. We also remark that there is no general method for identifying integrable Hamiltonian systems. The analytical methods that have been used so far to provide necessary conditions for integrability are:

1. Singularity analysis of the solutions in the complex time plane (Painlevé analysis) [99]
2. Search for local or global symmetries of the equations [87]
3. Substitution of integrals in the form of series and determination of the coefficients [55, 35]

Since most Hamiltonian systems, however, are non–integrable, we limit ourselves to the study of individual orbits of Hamiltonian systems that are of a particular interest. A multitude of indicators have been developed in recent years to characterize such reference orbits as ordered or chaotic. The inspection of successive intersections of an orbit with a Poincaré surface of section (PSS) [70] has been particularly useful in 2D maps and 2 DOF Hamiltonian systems. Some of the most important ones, based on the analysis of a time series constructed by the coordinates of the orbit under studied, are the following:

The frequency map analysis of Laskar [65, 66, 67, 68], the "0–1" test [50, 51], the method of the low frequency spectral analysis [125, 63], the "patterns method" [102, 103], the recurrence plots technique [128, 129] and the information entropy index [86]. One could also refer to several ideas presented by various authors that could be used in order to distinguish between chaoticity and regularity, like the differences appearing for regular and chaotic orbits in the time evolutions of their correlation dimension [43], in the time averages of kinetic energies related to the virial theorem [56] and in the statistical properties of the series of time intervals between successive intersections of orbits with a PSS [62].

While some of the most important ones, based on the study of the behavior of deviation vectors, are the following:

The Fast Lyapunov indicator (FLI) [44, 48, 47, 45, 42, 52] and its variants [10, 11], the Smaller ALignment Index (SALI) [104, 109, 108] and its generalization, the so–called Generalized ALignment Index (GALI) [106, 107], the Mean Exponential Growth of Nearby Orbits (MEGNO) [22, 23], the Relative Lyapunov Indicator (RLI) [100, 101], the Average Power Law Exponent (APLE) [72], as well as methods based on the study of spectra of quantities related to these vectors like the stretching numbers [44, 71, 118, 126, 91], the helicity angles (the angles of deviation vectors with a fixed direction) [31], the twist angles (the differences of two successive helicity angles) [32], or the study of the differences between such spectra [69, 120].

A systematic and detailed comparative study of the efficiency and reliability of the various chaos detection techniques has not been done yet, although comparisons between some of the existing methods have been performed sporadically in studies of particular dynamical systems [104, 108, 115, 114, 64, 72].

The most important ones for us in this thesis are the last two and are described in detail later in this chapter.

2.2 Basic Principles of the Structure and Dynamics of Galaxies

As is well–known, the three fundamental components of a galaxy are *stars*, *gas* and *dust*. In recent decades of course, two more components have been added by astronomers, which may in fact turned out to be the most important: *black holes* at the center of galaxies and *dark matter* in the surroundings. In this thesis, we will restrict our attention to the motion of individual mass points (stars) moving in the mean field of all other components. Thus, we will be able to compare our results with the popular approach of integrating Newton's equations for N bodies

$$v_i = \frac{dx_i}{dt}, \qquad \frac{dv_i}{dt} = -\sum_{\substack{j=1 \\ j \neq i}}^{N} \frac{G m_i m}{|x_j - x_i|^3}(x_j - x_i), \quad i = 1, ..., N, \tag{2.35}$$

where the i^{th} star is moving under the gravitational attraction of its neighbors. The advantage of our mean field approach is that it is faster and more accurate than the other so–called N–body simulation scheme, which relies on first principles, yet makes heavy use of time–consuming and memory intensive computations.

2.2.1 Galaxy classification

There are many ways of classifying galaxies but by far the best known so far is the Hubble system [15], which was originally suggested by Hubble in his 1936 book, *The Realm of the Nebulae.* Galaxy classification is a topic of it's own right (see e.g. Sidney van den Bergh's *Galaxy Morphology and Classification*), so here we just remind readers of the basic classes and the difficulties encountered in any classification scheme. In Hubble's tuning–fork diagram (Fig. 2.1), on the left are the sequence of elliptical galaxies spanning the range from circular to highly elliptical systems. These are denoted by **E**n, where $n = 10(1 - b/a)$ is computed by measuring the axial ratio b/a of the ellipse formed on the sky. Note that these are measured from the projection on the sky, so that the intrinsic 3–dimensional distribution may be considerably different (in fact, in general elliptical galaxies are likely to be triaxial, and the axes can change as a function of radius). The elliptical systems are often further sub–divided into dwarf types (dE), although it is not clear if the dwarfs are simply small elliptical or form a class of their own. Dwarf spheroidals (dSph) are a closely related type, the primary difference being that they are even less luminous and more diffuse (they are an interesting target for dynamical studies because of their very high dark matter content). With the advent of new technology that permits detailed studies, the smallest galaxies have become a topical area of research. For a summary of known dwarf galaxies in the local group, see the article by Mateo et al. in the 1998 Annual Reviews of Astronomy and Astrophysics [83].

After the ellipticals, Hubble's diagram splits in two, with two parallel sequences differentiated by the presence (top sequence) or absence (bottom) of a stellar bar in the center. The first galaxies are the so-called *lenticular* or *spheroidal* galaxies, designed **S0** (or SB0 if there is a bar). These systems appear to be strongly oblate like a spiral system but without any clear spiral structure. Like ellipticals, they usually have little dust or gas content, although some systems can contain significant amounts of dust: the strength of the dust is sometimes signified by a subscript ranging from $S0_1$ (no dust) to $S0_3$ (prominent dust lane).

After the spheroidals come the spirals, designated **Sa**, **Sb** or **Sc** depending on three characteristics: the tightness of the spiral arms, the size of the central bulge and the definitions of the arms. Spirals with tight, well–defined arms and a strong central bulge are Sa, while Sc systems have loose, poorly defined spiral arms and little or no central spheroidal component. Note that while these three characteristics vary, exceptions exist which can make classification difficult. If the spiral has a bar, it is classified with SBa, SBb or SBc. Additions have been suggested to this system, including de Vaucouleurs addition of Sd and Sm spiral systems that include galaxies which are looser or have even more poorly defined arms than the Sc class.

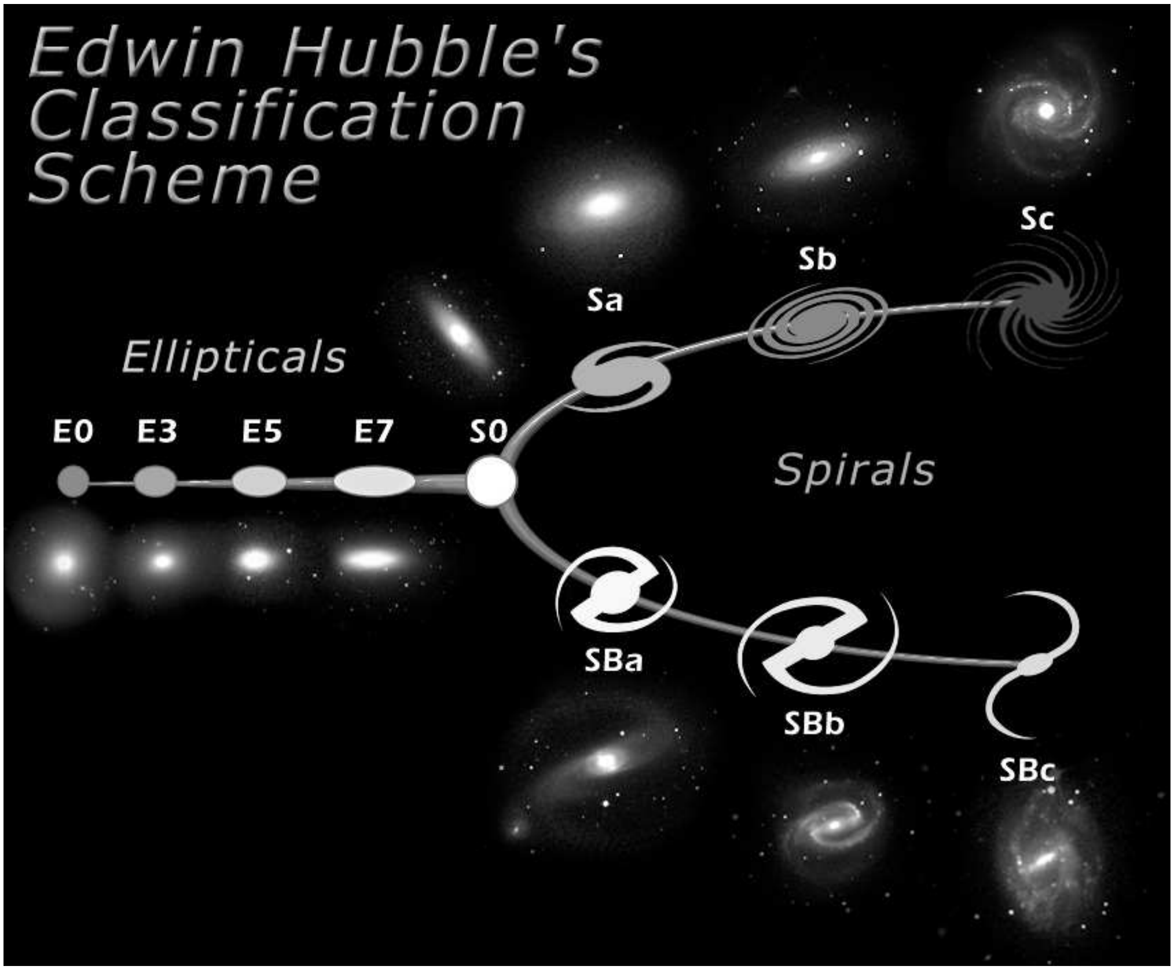

Figure 2.1: Fork diagram galaxy classification.

Hubble thought that galaxies evolved along his sequence, going from elliptical ("early") galaxies to spiral "late") galaxies. While this idea is no longer thought likely, the terminology has stuck. It is not uncommon to find a numerical **T** stage assigned to the Hubble type for the use in some forms of statistical analysis. This ranges from -5 (E0) to 0 (S0) to 6 (Sc) to 10 (Irr). Entirely outside of this sequence are the irregular galaxies **Irr** which lack symmetry or well-defined spiral arms, and the peculiar galaxies which may be undergoing a merger or interaction.

Galaxies are not uniformly distributed in space. While isolated field galaxies do exist, the majority of galaxies are found in groups or clusters. Very small groups, like the local group, consist of only a few large galactic systems. Large groups may have up to 100, while full–fledged clusters often have thousands of large galaxies. Galaxies of different types are not equally represented in different environments. In particular, ellipticals are much more likely to be found in dense cluster cores than in the field, while spirals show the opposite trend. This is most commonly called the **morphology–density** relation and is clearly telling us something about what sets galaxies morphology, but it is not clear whether spiral galaxies are transformed into ellipticals by the dense environments of clusters, or if such regions preferentially formed elliptical galaxies even before the cluster formed (clusters are thought, from both theoretical and observational evidence, to be younger than galaxies).

2.2.2 The gravitational potential

If we wish to follow the motion of a particle under the sole influence of gravity, then its acceleration is given as the sum of the inverse–square law forces from all the other particles present in its surroundings

$$\frac{d\mathbf{v}}{dt} = -\sum_i \frac{Gm_i}{|\mathbf{x}-\mathbf{x}_i|^3}(\mathbf{x}-\mathbf{x}_i) = -\int_V \frac{G\rho(\mathbf{x}')}{|\mathbf{x}-\mathbf{x}'|^3}(\mathbf{x}-\mathbf{x}')d^3\mathbf{x}', \tag{2.36}$$

where $\mathbf{x}$ and $\mathbf{v}$ are the location and velocity of the particle in 3D space. Note that in the equations above, we have transformed the sum into an integral by assuming that we can write down a smooth density distribution $\rho(\mathbf{x})$. The integral is over all space. We can write this in a simpler form if we use the following identity

$$\nabla_{\mathbf{x}} = -\frac{\mathbf{x}-\mathbf{x}'}{|\mathbf{x}-\mathbf{x}'|^3}, \qquad if \quad \mathbf{x} \neq \mathbf{x}' \tag{2.37}$$

which can be straightforwardly demonstrated by writing it out in cartesian coordinates. Note that the notation $\nabla_{\mathbf{x}}$ indicates that the differentiation is done with respect to $\mathbf{x}$ (as opposed to $\mathbf{x}'$). This lets us rewrite the right–hand side of equation (2.36) as

$$\frac{d\mathbf{v}}{dt} = \nabla_{\mathbf{x}} \int_V \frac{G\rho(\mathbf{x}')}{|\mathbf{x}-\mathbf{x}'|}d^3\mathbf{x}' = -\nabla_{\mathbf{x}}\Phi(\mathbf{x}) \tag{2.38}$$

We have been able to take the gradient operator out if the integration because the integration is over $\mathbf{x}'$, while the gradient is with respect to $\mathbf{x}$. This shows that the force can be written entirely as the gradient of some quantity (the potential $\Phi(\mathbf{x})$) instead of a force itself. This is true because of the gravitational force and its purely radial nature. Since a scalar field is much easier to think about and work with than a full vector field, we will mostly use the potential, which we write down here for completeness' sake

$$\Phi(\mathbf{x}) = -\int_V \frac{G\rho(\mathbf{x}')}{|\mathbf{x}-\mathbf{x}'|}d^3\mathbf{x}' \tag{2.39}$$

This is an important simplification, but we can write the potential in an even simpler way, that doesn't involve any integral at all. This requires some slightly contorted reasoning to prove (we follow [15] for this derivation). The first step is to apply $\nabla^2_{\mathbf{x}}$ to both sides of equation (2.39) to get

$$\begin{aligned}
\nabla^2_{\mathbf{x}}\Phi(\mathbf{x}) &= -\int_V \nabla^2_{\mathbf{x}} \frac{G\rho(\mathbf{x}')}{|\mathbf{x}-\mathbf{x}'|}d^3\mathbf{x}' \\
&= -\int_V \nabla_{\mathbf{x}} \frac{G\rho(\mathbf{x}')}{|\mathbf{x}-\mathbf{x}'|^3}(\mathbf{x}-\mathbf{x}')d^3\mathbf{x}' \\
&= -\int_V G\rho(\mathbf{x}')\left[\frac{3}{|\mathbf{x}-\mathbf{x}'|^3} - \frac{3(\mathbf{x}-\mathbf{x}')(\mathbf{x}-\mathbf{x}')}{|\mathbf{x}-\mathbf{x}'|^2|\mathbf{x}-\mathbf{x}'|^3}\right]d^3\mathbf{x}' \\
&= 0, \qquad if \quad \mathbf{x} \neq \mathbf{x}'
\end{aligned} \tag{2.40}$$

where we have used the identity in equation (2.37). This tells us that any contribution to the potential must come from a very small region around $\mathbf{x} = \mathbf{x}'$. If we restrict the volume integral to a small sphere with radius h around this point, where h can be made arbitrarily small. Since h is very small, the density can be assumed to be constant across this very small region and hence can be taken out of the integral. From equation (2.40), we get

$$\begin{aligned}
\nabla^2_{\mathbf{x}}\Phi(\mathbf{x}) &= -G\rho(\mathbf{x})\int_{|\mathbf{x}'-\mathbf{x}|\le h}\nabla_{\mathbf{x}}\left[\frac{\mathbf{x}-\mathbf{x}'}{|\mathbf{x}-\mathbf{x}'|^3}\right]d^3\mathbf{x}' \\
&= -G\rho(\mathbf{x})\int_{|\mathbf{x}'-\mathbf{x}|\le h}\nabla'_{\mathbf{x}}\left[\frac{\mathbf{x}-\mathbf{x}'}{|\mathbf{x}-\mathbf{x}'|^3}\right]d^3\mathbf{x}' \qquad (2.41)\\
&= -G\rho(\mathbf{x})\int_{|\mathbf{x}'-\mathbf{x}|=h}\frac{\mathbf{x}-\mathbf{x}'}{|\mathbf{x}-\mathbf{x}'|^3}d^2\mathbf{S}
\end{aligned}$$

The second step is permitted because $\mathbf{x}$ is arbitrarily close to $\mathbf{x}'$, and in the third step we have made use of the divergence theorem, which tells us that the volume integral of $\nabla\cdot\mathbf{f}$ can be written as a surface integral of $\mathbf{f}\cdot d^2\mathbf{S}$. The integral is over the sphere with radius h, and $d^2\mathbf{S}$ is the surface element on the sphere and points in a direction normal to the surface. The vector $\mathbf{x}-\mathbf{x}'$ is also normal to the surface and has a length h (since it lies on the surface of the sphere). This makes this integral easy to evaluate and we get simply 4π. The final result then in Poisson's equation for the potential

$$\nabla\Phi(\mathbf{x}) = 4\pi G\rho(\mathbf{x}) \qquad (2.42)$$

This result is particularly useful when we start looking at spherically symmetric systems for which the density profile depends only on radius r.

It is useful to invoke two of Newton's theorems about spherically symmetric systems which we simply state below (see [15] for a proof):

Newton I: Inside a spherical shell of uniform density, the net acceleration from that shell is zero. This also means that the potential is constant inside a shell.

Newton II: The acceleration outside a spherically symmetric shell of mass is the same as if all the mass is at the center. That is, we can treat a spherically symmetric object as if all of the mass inside a radius r is at the center – this simplifies calculations enormously, and is implicit in our usual method for determining the enclosed mass within $M(<r)$ in a galaxy with

$$u_c^2 = \frac{GM(<r)}{r} \qquad (2.43)$$

We can now write down a general expression for the potential of any symmetric distribution with density $\rho(r)$, by dividing the calculation into shells with $r'<r$ and shells with $r'>r$

$$\Phi(r) = -[\frac{GM(<r)}{r} + \int_0^\infty 4\pi G\rho(r')r'dr'] \qquad (2.44)$$

where by $M(<r)$ we mean the integrated mass within radius r.

2.2.3 Models of galaxy potentials

(i) **The Plummer sphere**

Plummer, in 1911, used the following potential–density pair to fit observations of global clusters

$$\Phi_P(r) = -\frac{GM}{\sqrt{r^2+b^2}}, \qquad (2.45)$$

from which, by direct differentiation we find

$$\nabla^2\Phi_P(r) = \frac{1}{r^2}\frac{d}{dr}(r^2\frac{d\Phi_P(r)}{dr}) = \frac{3GMb^2}{(r^2+b^2)^{5/2}}. \tag{2.46}$$

Thus from Poisson's equation we have that the density corresponding to the potential (2.45) is

$$\rho_P(r) = (\frac{3M}{4\pi b^3})(1+\frac{r^2}{b^2})^{-5/2} \tag{2.47}$$

The Plummer sphere provides a good fit also to dwarf spheroidal galaxy light distributions [15].

(ii) **The Kuzmin–Toomre model**
The Kuzmin/Toomre potential is given by

$$\Phi_K(R,z) = -\frac{GM}{\sqrt{r^2+(a+|z|)^2}}, \tag{2.48}$$

which represents a very flattened potential [15]. When we apply Gauss's theorem to a flat volume that contains a small portion of the plane $z=0$, we conclude that the surface density corresponding to this potential is

$$\Sigma_K(R) = -\frac{aM}{2\pi(R^2+a^2)^{\frac{3}{2}}}. \tag{2.49}$$

The particular potential–density pair was initially introduced by Kuzmin [1956] and later rederived by Toomre [1963], so it is known as the Kuzmin–Toomre potential–density pair.

(iii) **The Miyamoto-Nagai disc**
The Miyamoto–Nagai [84, 85] disc potential and density is given by

$$\Phi_M(R,z) = -\frac{GM}{\sqrt{R^2+(A+\sqrt{B^2+z^2})^2}}, \tag{2.50}$$

$$\rho_M(R,z) = (\frac{B^2M}{4\pi})\frac{AR^2+(A+3\sqrt{z^2+B^2})((A+\sqrt{z^2+B^2})^2}{[R^2+(A+\sqrt{z^2+B^2})^2]^{5/2}(z^2+B^2)^{3/2}}, \tag{2.51}$$

where the above density profile is an analytic solution of Poisson's equation in cylindrical coordinates: $\nabla^2\Phi(R,z) = 4\pi G\rho(R,z)$.

Notice that for $A \to 0$, potential (2.50) reduces to Plummer's sphere, having a scale length, B. For $B \to 0$ and $A \to 0$, we shrink the Plummer sphere to zero size and recover the potential due to a point mass (*Kepler's* potential). Finally, for $B \to 0$; $A \neq 0$ we form an infinitesimally thin Kuzmin disc. For this reason, the Miyamoto–Nagai disc is also often referred to as a Plummer–Kuzmin model. Notice that A sets a "scale height" and B a "scale length" for the disc. Thus, depending on the choice of the two parameters, $\Phi_M(R,z)$ can represent the potential of a wide family of systems from an infinitesimally thin disc to a sphere.

2.2.4 Equation of motion in rotating coordinates

We define two frames, S, which is stationary and S' which is rotating with fixed angular frequency Ω. At a particular instant the x and y axis of these two systems overlap. The velocity in the rotating frame is related to the velocity in the stationary frame $\mathbf{v}$ by

$$\frac{d\mathbf{x}}{dt} = \frac{d\mathbf{x}'}{dt} + \Omega\times\mathbf{x} \tag{2.52}$$

To find the equations of motion in the new frame we differentiate this expression to find

$$\begin{aligned} \frac{d^2\mathbf{x}}{dt^2} &= \frac{d}{dt}(\frac{d\mathbf{x}'}{dt}) + \Omega \times \frac{d\mathbf{x}}{dt} \\ &= \frac{d^2\mathbf{x}'}{dt^2} + \Omega \times \frac{d\mathbf{x}'}{dt} + \Omega \times (\frac{d\mathbf{x}'}{dt} + \Omega \times \mathbf{x}) \\ &= \frac{d^2\mathbf{x}'}{dt^2} + 2\Omega \times \frac{d\mathbf{x}'}{dt} + \Omega \times (\Omega \times \mathbf{x}) \end{aligned} \tag{2.53}$$

so the equation of motion changes from the simple $d\mathbf{v}/dt = -\nabla\Phi$ to

$$\frac{d\mathbf{v}'}{dt} = \nabla\Phi(\mathbf{x}) - 2\Omega \times \mathbf{v}' - \Omega \times (\Omega \times \mathbf{x}') \tag{2.54}$$

The second term on the right-hand side is the Coriolis force which is perpendicular to the direction of motion, and the third term is the centrifugal force. They are both fictitious forces, resulting only from the fact that we are working in a rotating coordinate system. As before, we would like to define an effective potential which brings us back to our simple equation of state. In this case, however, it is not possible because the Coriolis force cannot be written as the gradient of an effective potential. The best we can do is define an effective potential as

$$\Phi_{\text{eff}}(\mathbf{x}') = \Phi(\mathbf{x}') - \frac{1}{2}(\Omega \times \mathbf{x}')^2 \tag{2.55}$$

and this allows us to write the equation of motion in the simplified form

$$\frac{d\mathbf{v}'}{dt} = \nabla\Phi_{\text{eff}}(\mathbf{x}') - 2\Omega \times \mathbf{v}' \tag{2.56}$$

This is not as bad as it seems because the Coriolis force is perpendicular to the velocity and so it can do no work on the particle. In fact, we can define an energy–like quantity

$$E_J = \frac{1}{2}(\mathbf{v}')^2 + \Phi_{\text{eff}}(\mathbf{x}') \tag{2.57}$$

which is conserved in the rotating frame. Note that $E_J = E - \Omega \times \mathbf{L}$, where $\mathbf{L} = m\mathbf{x} \times \mathbf{v}$ is the angular momentum, and so is a combination of the energy and the angular momentum (neither of which are conserved in this frame separately).

Generally speaking, the main different kinds of orbits in galaxy models that we shall be interested in can be classified as follows:

(i) Periodic orbits: They can be (linearly) stable and unstable, depending on whether their *Floquet* multipliers (or, eigenvalues) of the associated monodromy matrix satisfy: $|\lambda_i| \leq 1$ for all i, or $|\lambda_i| > 1$ for at least one i respectively.

(ii) Quasiperiodic orbits: They are said to characterize "regular" motion since they lie on m–dimensional tori defined by m incommensurable frequencies ω_i.

(iii) Chaotic orbits: They are characterized by the fact that almost all orbits in their neighborhoods diverge from them exponentially, as time evolves.

2.3 Methods of Detecting Chaos

2.3.1 Poincaré surfaces of section (PSS)

The definition of a Poincaré surface of section lies at the heart of the treatment of Hamiltonian flows [70]. For an autonomous system with two degrees of freedom, the phase space is 4–dimensional.

Referring to Fig. 2.2, we choose a two–dimensional surface Σ_R in the phase space and label its two sides (say left and right). We then study the successive intersections of a trajectory with this surface. The intersections are generated each time the trajectory pierces the surface in a particular sense (say from left to right).

A particularly convenient choice for the surface of section Σ_R can be made as follows: We first note that the trajectory lies on a three–dimensional energy surface $H(q_1, q_2, p_1, p_2) = H_0$ in the four–dimensional phase space, Fig. 2.2b(1). This equation determines any of the four variables, say p_2, in terms of the other three

$$p_2 = p_2(q_1, q_2, p_1). \tag{2.58}$$

We are therefore led to consider the projection of the trajectory onto a 3–dimensional volume (q_1, q_2, p_1), Fig. 2.2b(2). If the motion is bounded, then the plane q_2 =const. within this volume may be repeatedly crossed by the trajectory. This plane, consisting of a single coordinate q_1 and its canonical momentum p_1, is a convenient choice for the surface of section. If we plot the successive intersections of the motion with the surface of section, they will in general occur anywhere within a bounded area of the plane, If a constant of the motion

$$I(q_1, q_2, p_i, p_2) = I_0 = const. \tag{2.59}$$

exists in addition to H_0, then equations (2.58) and (2.59) can be combined to yield

$$p_1 = P_1(q_1, q_2). \tag{2.60}$$

Thus the successive crossings of the motion with the surface of section must lie on a unique curve, given by (2.60) with q_2 =const. In this way we can determine the existence of constants of the motion by examining the intersection of a trajectory with a surface of section. Once this existence is established, the smooth curves can be examined for local stability and other interesting features.

It will be noted that the particular surface of section (q_1, p_1) is just the *reduced phase space* of the original Hamiltonian system. Furthermore, successive crossings are obtained from one another by a canonical transformation generated by Hamilton's equations. Thus the area bounding a closed curve in the surface of section is conserved on successive crossings of the surface. This important property can be shown directly as follows: we write general differential relations

$$\begin{aligned} d\lambda &= \frac{\partial \lambda}{\partial q} dq + \frac{\partial \lambda}{\partial \mu} d\mu \\ dp &= \frac{\partial p}{\partial q} dq + \frac{\partial p}{\partial \mu} d\mu, \end{aligned} \tag{2.61}$$

where the λ and μ may be thought of as the initial position and momentum taken in a surface of section. Substituting for the partial derivatives in terms of the generating function $F_2(\lambda, p)$, and solving for dp and dq in terms of $d\lambda$ and $d\mu$, we have

$$\begin{aligned} dq &= (F_{\lambda p} - \frac{F_{pp} F_{\lambda\lambda}}{F_{\lambda p}}) d\lambda + \frac{F_{pp}}{F_{\lambda p}} d\mu \\ dp &= -\frac{F_{\lambda\lambda}}{F_{\lambda p}} d\lambda + \frac{1}{F_{\lambda p}} d\mu, \end{aligned} \tag{2.62}$$

where the notation $F_\lambda = \frac{\partial F_2}{\partial \lambda}$ has been used for compactness. The determinant of the coefficients of equation (2.62), which is equivalent to the Jacobian of the transformation from (λ, μ) to (p, q)

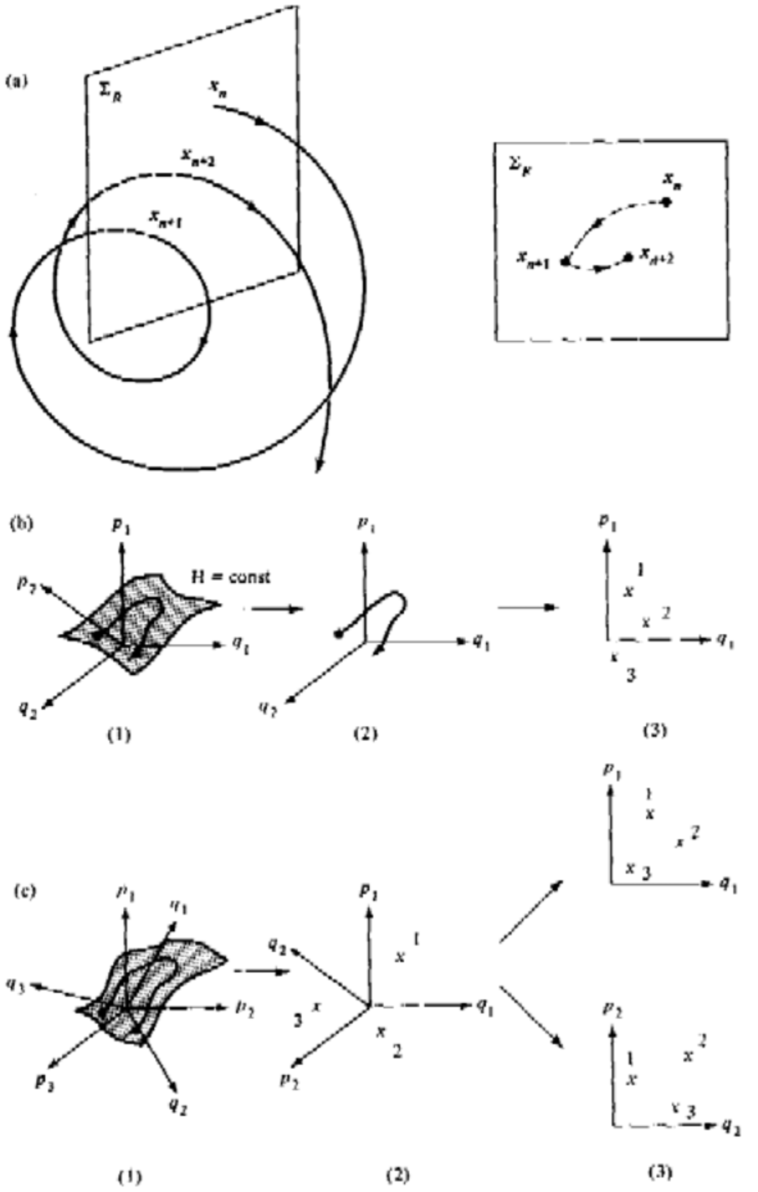

Figure 2.2: Motion in phase space and definition of the Poincaré surface of section. (a) Intersections of a trajectory with the surface of section. (b) Two degrees of freedom showing: (1) four–dimensional phase space with the trajectory on a three- dimensional energy surface; (2) projection of the trajectory onto the (q_1, q_2, p_1) volume; and (3) successive intersections of the trajectory with the two-dimensional surface of section $q_2 = \text{const}$. (c) Three degrees of freedom showing: (1) six–dimensional phase space with trajectory on a five–dimensional energy surface; (2) three successive intersections of the trajectory with the four–dimensional surface of section $q_3 = \text{const}$.; and (3) projections of these intersections of the surface of section on the (q_1, p_1) and (q_2, p_2)–planes. (Image from Lichtenberg & Lieberman (1992))

variables, is equal to one, proving the area-preserving nature of the transformation[3]. The area–preserving property of a two–dimensional surface of section in a 4–dimensional phase space will be very important in subsequent chapters, both for numerically looking for constants of the motion and for determining the stability of the linearized motion near a periodic solution. The concept of a surface of section can be generalized to systems with $N > 2$ degrees of freedom. For a time–independent Hamiltonian with N degrees of freedom, the energy surface in phase space has dimensionality $2N - 1$, Fig. 2.2c(1). As previously done, we project out a single generalized coordinate, say p_N, and consider the successive intersection of the trajectory with the$(2N - 2)$–dimensional surface of section q_N =const. with coordinates $p_1, .., p_{N-1}, q_1, ..., q_{N-1}$ [Fig. 2.2c(2)]. As before, the surface of section is a reduced phase space in which the volume–preserving property holds.

If one or more constants of the motion exist, then the intersections of the trajectory with the surface will all lie on a unique surface of dimensionality less than $2N-2$; otherwise the intersections will fill a $(2N - 2)$–dimensional volume within the section. For multidimensional systems, if the motion in each degree of freedom is approximately separable, the $N - 1$ projections of the surface of section onto the (q_i, p_i)–planes, shown in Fig. 2.2c(3), are a useful way to visualize the motion of the trajectory point. For a regular trajectory, which is exactly separable in the (q_i, p_i)–coordinates, the motion in each (q_i, p_i)–plane is area–preserving, a constant of the motion exists in the ith degree of freedom, and the trajectory intersections lie on a smooth curve in the (q_i, p_i)–plane. However, for a system with more than two degrees of freedom, even for regular trajectories, the trajectory intersections with the surface of section, projected onto an arbitrary (q_i, p_i)–plane, do not generally lie on a smooth curve, but rather fill an annulus of finite area, whose thickness is related to the nearness to exact separability in the (q_i, p_i)–coordinates. In this case, the intersections with the surface of section lie in an $(N - 1)$–dimensional surface, whose projection onto a (q_i, p_i)–plane is a region of finite area.

2.3.2 The spectrum of Lyapunov Exponents Spectrum

The Lyapunov Characteristic Exponents (LCEs) or Lyapunov Characteristic Numbers (LCN) are very important for the study of dynamical systems, for distinguishing between regular and chaotic behavior of orbits in phase space [70, 12, 13]. In practice, the LCEs describe the rate of separation of infinitesimally close trajectories.

Let us consider a flow $\mathbf{x}(t)$, generated by an autonomous first-order system

$$\frac{d\mathbf{x}(t)}{dt} = V(\mathbf{x}(t)) \tag{2.63}$$

and a trajectory in the M-dimensional phase space and a nearby trajectory with initial conditions $\mathbf{x_0}$ and $\mathbf{x_0} + \Delta\mathbf{x_0}$ respectively. These evolve with time yielding the tangent vector $\Delta\mathbf{x}(\mathbf{x_0}, t)$ with its Euclidean norm:

$$d(\mathbf{x_0}) = \|\Delta\mathbf{x}(\mathbf{x_0}, t)\|.$$

Writing $\Delta\mathbf{x} = (\Delta x_1, ..., \Delta x_M) \equiv \mathbf{w}$, the time evolution for $\mathbf{w}$ if found by linearizing (2.63), to obtain

$$\frac{d\mathbf{w}}{dt} = J(\mathbf{x}(t))\mathbf{w}, \tag{2.64}$$

where

$$J(\mathbf{x}(t)) = \frac{\partial V}{\partial \mathbf{x}}$$

---

[3] For non–canonical coordinates some function of the coordinates, the measure is preserved, rather than the area.

is the Jacobian matrix $V(\mathbf{x})$. The mean exponential rate of divergence of two initially close trajectories is

$$\sigma(\mathbf{x}_0, w) = \lim_{t\to\infty}(\frac{1}{t})\ln\frac{d(\mathbf{x}_0,t)}{d(\mathbf{x}_0,0)}. \tag{2.65}$$

It can be shown that σ exists and is finite. Furthermore, there is an M-dimensional basis $\hat{e}_i$ of $\mathbf{w}$ such that for any $\mathbf{w}$, σ takes one of the M (possibly non-distinct) values

$$\sigma_i(\mathbf{x}_0) = \sigma(\mathbf{x}_0, \hat{e}_i), \quad \forall i = 1, 2, ..., M,$$

which are the Lyapunov characteristic exponents. These can be ordered by size,

$$\sigma_1 \geq \sigma_2 \geq ... \geq \sigma_M.$$

The LCEs are independent of the choice of metric for the phase space [88]. A flow has as many Lyapunov exponents, as the the number of the differential equations of the system. For a Hamiltonian flow, $\mathbf{x} = (q,p)$, the vector field V is

$$V(\mathbf{x}) = (-\frac{\partial H}{\partial q}, \frac{\partial H}{\partial p})$$

In this case, the Lyapunov exponents have a particular symmetry:

$$\sigma_i = -\sigma_{2n-i+1}, \quad \forall i = 1, 2, ..., M,$$

where $M = 2n$ and n is the number of the degrees of freedom.

This is how the Lyapunov exponents of the vectors $\mathbf{w}$ (which are also called Lyapunov exponents of order 1) are calculated. Generalizing the above concept, we can calculate the mean exponential growth of a p-dimensional volume in the tangent space, where $p \leq M$. We use the operator notation

$$V_p = \mathbf{w}_1 \wedge \mathbf{w}_2 \wedge ... \wedge \mathbf{w}_p.$$

for the volume V_p of a p-dimensional parallelepiped whose edges are the vectors $\mathbf{w}_1, ..., \mathbf{w}_p$. Then, the Lyapunov exponent of order p is defined by

$$\sigma^{(p)}(\mathbf{x}_0, V_p) = \lim_{t\to\infty}(\frac{1}{t})\ln\frac{\|V_p(\mathbf{x}_0,t)\|}{\|V_p(\mathbf{x}_0,0)\|} \tag{2.66}$$

σ^p is given as the sum of p Lyapunov exponents of order 1

$$\sigma^{(p)} = \sigma_1^{(p)} = \sigma_1 + \sigma_2 + ... + \sigma_p, \tag{2.67}$$

This equation is used to compute numerically the Lyapunov exponents. For $p = M$, we obtain the mean exponential rate of growth of the phase space volume as

$$\sigma^M = \sum_{i=1}^{M} \sigma_i(\mathbf{x}_0). \tag{2.68}$$

For a measure-preserving flow (like Hamiltonian systems), we see that

$$\sum_{i=1}^{M} \sigma_i(\mathbf{x}_0) = 0, \tag{2.69}$$

while for a dissipative system, this sum must be negative.

Calculation of the Maximum Lyapunov Exponent σ_1

For the calculation of the Maximum Lyapunov Exponent, we choose an initial tangent vector $\mathbf{w}_0$ and calculate the $\mathbf{w}$ by the (2.86) with respect to $\mathbf{w}$ along an orbit $x(t)$, obtaining numerically the quantity

$$d(t) = \|\mathbf{w}(t)\|, \tag{2.70}$$

where for convenience the initial norm d_0 is chosen to be unity. The difficulty is that if the norm of $\mathbf{w}$ increases exponentially with t, this leads to overflow and other computation errors. To circumvent this problem, we choose a small fixed time interval τ and we renormalize $\mathbf{w}$ to a norm of unity every τ seconds. Thus, we iteratively compute the values

$$d_k = \|\mathbf{w}_{k-1}\|, \tag{2.71}$$

$$\mathbf{w}_k(0) = \frac{\mathbf{w}_{k-1}(\tau)}{d_k}, \tag{2.72}$$

where $\mathbf{w}_k(\tau)$ is obtained by integrating Eq. (2.86), with the initial value $\mathbf{w}_k(0)$, along the trajectory from $\mathbf{x}(k\tau)$ to $\mathbf{x}((k+1)(\tau))$. From Eq. (2.65), we can define the quantity

$$\sigma_n = \frac{1}{n\tau} \sum_{i=1}^{M} \ln d_i. \tag{2.73}$$

For τ not too large, it can be shown that

$$\sigma_\infty = \lim_{t\to\infty} \sigma_n = \sigma_1 \tag{2.74}$$

exists and is independent of τ. In the regular regions of near-integrable systems $\sigma_\infty = 0$, while in a connected chaotic region, σ_∞ is always positive and independent of the initial value of x. Since, τ is arbitrary, Eq. (2.73) can be applied to calculate Lyapunov exponents for maps as well as flows.

Calculation of all the Lyapunov Exponents

In order to calculate all the Lyapunov Exponents for a M-dimensional flow, instead of choosing the tangent vector $\mathbf{w}$ into alignment with $\hat{e}_2, \hat{e}_3, ...,$, which will fail due to numerical error (it eventually brings $\mathbf{w}(t)$ into alignment with $\hat{e}_1$), we choose an initial set of p orthonormal tangent vectors and numerically calculate the p-dimensional volume $V_p(t)$ defined by these vectors. The Lyapunov exponent $\sigma_1^{(p)}$ of order p is then found using Eq. (2.66). Doing this for $p = 1, 2, ..., M$, we use Eq. (2.65) to find the Lyapunov exponents $\sigma_1, \sigma_2, ..., \sigma_M$. As the tangent vectors evolve, the angle between any two vectors generally becomes too small for the numerical computations. Thus, in addition to renormalizing $\mathbf{w}$ after each time interval τ, we must replace the evolved vectors by a new set of orthonormal vectors. These new vectors must be chosen to span the same subspace as the evolved set.

The above procedure can be systematized to calculate the evolution of all p–dimensional volumes at one time by computing the evolution of M vectors and making the special choice of orthonormalizing by means of Gram-Schmidt procedure. Recall $\mathbf{w}_{k-1}(\tau)$ is the evolved tangent vector $\mathbf{w}_{k-1}(0)$ along the trajectory from $\mathbf{x}((k-1)(\tau))$ to $\mathbf{x}(k\tau)$. Using this, we first calculate for each time interval τ the quantities

$$d_k^{(1)} = \|\mathbf{w}_{k-1}^{(1)}\|, \tag{2.75}$$

$$\mathbf{w}_k^{(1)}(0) = \frac{\mathbf{w}_{k-1}^{(1)}(\tau)}{d_k^{(1)}} \tag{2.76}$$

and then successively derive, for $j = 2, ..., M$

$$\mathbf{u}_{k-1}^{(j)}(\tau) = \mathbf{w}_{k-1}^{(j)}(\tau) - \sum_{i=1}^{j-1}[\mathbf{w}_{k-1}^{(i)}(0)\cdot\mathbf{w}_{k-1}^{(j)}(\tau)]\mathbf{w}_k^{(i)}(0), \tag{2.77}$$

$$d_k^{(j)} = \|\mathbf{u}^{(j)}(\tau)\|, \tag{2.78}$$

$$\mathbf{w}_k^{(j)}(0) = \frac{\mathbf{u}_{k-1}^{(j)}(\tau)}{d_k^{(j)}}. \tag{2.79}$$

During the $(k-1)$st time interval, the volume V increases by a factor of $d_k^{(1)}, d_k^{(2)}, ..., d_k^{(p)}$. The definition (2.66) then implies

$$\sigma_n = \lim_{t\to\infty}\frac{1}{n\tau}\sum_{i=1}^{n}\ln(d_k^{(1)}d_k^{(2)}...d_k^{(p)}). \tag{2.80}$$

Subtracting $\sigma_1^{(p-1)}$ from $\sigma_1^{(p)}$ and using the Eq. (2.65, we obtain the p^{th} Lyapunov exponent

$$\sigma_p = \lim_{t\to\infty}\frac{1}{n\tau}\sum_{i=1}^{n}\ln d_i^{(p)}. \tag{2.81}$$

This is the relation that was actually used in our numerical calculations.

We emphasize here that it is not known a priori how to know the exact number of iterations or the total evolution time of a trajectory and its tangent vectors $\mathbf{w}$ that are necessary for the exact calculation of the Lyapunov exponents. For this reason it is required and useful to use other supplementary methods for distinguishing chaotic or regular behavior of a trajectory.

2.3.3 The Smaller ALigment Index (SALI)

Let us consider the N - dimensional phase space of a conservative dynamical system, which could be a symplectic map or a Hamiltonian flow. We consider also an orbit in that space with initial condition $P(0) = (x_1(0), x_2(0), ..., x_N(0))$ and two deviation vectors $\vec{\nu}_1(0)$, $\vec{\nu}_2(0)$ from the initial point $P(0)$. In order to compute the SALI for a given orbit, one has to follow the time evolution of the orbit with initial condition $P(0)$ and also of two deviation vectors $\vec{\nu}_1(t), \vec{\nu}_2(t)$ which initially point in two different directions. The evolution of these deviation vectors is given by the variational equations for a flow and by the tangent map for a discrete-time system. At every time step the two deviation vectors $\vec{\nu}_1(t)$ and $\vec{\nu}_2(t)$ are normalized by setting

$$\hat{\nu}_i(t) = \frac{\vec{\nu}_i(t)}{\|\vec{\nu}_i(t)\|}, \quad i = 1, 2 \tag{2.82}$$

and the SALI is then defined as [104]

$$\mathrm{SALI}(t) = min\left\{\|\hat{\nu}_1(t) + \hat{\nu}_2(t)\|\,,\|\hat{\nu}_1(t) - \hat{\nu}_2(t)\|\right\}. \tag{2.83}$$

The properties of the time evolution of the SALI clearly distinguish between ordered and chaotic motion as follows: In the case of Hamiltonian flows or dimensional symplectic maps with $n \geq 2$, the SALI fluctuates around a non-zero value for ordered orbits, while it tends to zero for chaotic orbits. In the case of 2D maps the SALI tends to zero both for ordered and chaotic orbits, following however completely different time rates, which again allows us to distinguish between the two cases.

In 2 and 3 degrees of freedom Hamiltonian systems the distinction between ordered and chaotic motion is easy because the ordered motion occurs on a 2D or 4D torus respectively on which any initial deviation vector becomes almost tangent after a short transient period. In general, two different initial deviation vectors become tangent to different directions on the torus, producing different sequences of vectors, so that SALI does not tend to zero but fluctuates around positive values. On the other hand, for chaotic orbits, any two initially different deviation vectors tend to coincide on the direction defined by the nearby most unstable manifold and hence either coincides with each other, or become opposite. This means that the SALI tends to zero when the orbit is chaotic and to a non-zero value when the orbit is ordered. Thus, the completely different behavior of the SALI helps us to distinguish between ordered and chaotic motion in Hamiltonian systems with 2 and 3 degrees of freedom and in general in dynamical systems of higher dimensionality.

In an autonomous Hamiltonian system of N degrees of freedom having a Hamiltonian function

$$H(q_1, ..., q_N, p_1, ..., p_N) = h = constant, \tag{2.84}$$

q_i and p_i, $i = 1, ..., N$ are the generalized coordinates and conjugate momenta respectively. An orbit in this system is defined by a vector $\vec{x}(t) = (q_1, ..., q_N, p_1, ..., p_N)$, with $x_i = q_i$ and $x_{i+N} = p_i$, $i = 1, ..., N$. The time evolution of this orbit is governed by the Hamilton equations of motion:

$$\frac{d\vec{x}}{dt} = \vec{V}(\vec{x}) = \left(\frac{\partial H}{\partial \vec{p}}, -\frac{\partial H}{\partial \vec{q}}\right) \tag{2.85}$$

while the time evolution of an initial deviation vector $\vec{\nu}(0) = (dx_1(0), ..., dx_{2N}(0))$ from the $\vec{x}(t)$ solution of (2.85) obeys the variational equations

$$\frac{d\vec{\nu}}{dt} = \mathbf{M}(\vec{x}(t))\vec{\nu} \tag{2.86}$$

where $\mathbf{M} = \partial\vec{V}/\partial\vec{x}$ is the Jacobian matrix of $\vec{V}$.

The SALI method has been applied successfully on different dynamical systems [104, 110, 109, 108, 3, 5, 89, 18, 77, 76, 78, 81, 80, 82, 79, 19, 116], frequently also by the name Alignment Index (AI) [121, 119, 123, 124, 122, 59, 60, 58] and confirmed to be a fast and easy to compute indicator of chaotic or regular motion.

2.3.4 The Generalized ALigment Index (GALI)

Let us consider the $2N$–dimensional phase space of a conservative dynamical system, which may be represented by a Hamiltonian flow of N degrees of freedom or a $2N$–dimensional system of coupled symplectic maps. In order to study whether an orbit is chaotic or not, we examine the asymptotic behavior of k initially linearly independent deviations from this orbit, denoted by the vectors $\overrightarrow{\nu}_1, \overrightarrow{\nu}_2, ..., \overrightarrow{\nu}_k$ with $2 \leq k \leq 2N$. Thus, we follow the orbit, using Hamilton's equations (or the map equations) of motion and solve in parallel the variational equations about this orbit to study the behavior of solutions located in its neighborhood.

The Generalized Alignment Index of order k is a generalization of the Smaller Alignment Index (SALI) and is defined [106] as the norm of the wedge (or exterior) product of k associated unit deviation vectors

$$\mathrm{GALI}_k(t) = \| \hat{\nu}_1(t) \wedge \hat{\nu}_2(t) \wedge ... \wedge \hat{\nu}_k(t) \| \tag{2.87}$$

representing *the volume of the parallelepiped*, whose edges are these k vectors. We note that the hat ($\hat{}$) over a vector denotes that it is of unit magnitude and that t represents again the continuous or discrete time.

In the case of a chaotic orbit, all deviation vectors tend to become *linearly dependent*, aligning in the direction of the eigenvector corresponding to the maximal Lyapunov exponent and GALI_k tends exponentially [106]: to zero following the law

$$\mathrm{GALI}_k(t) \propto e^{-[(\sigma_1-\sigma_2)+(\sigma_1-\sigma_3)+...+(\sigma_1-\sigma_k)]t}, \tag{2.88}$$

where $\sigma_1 > \ldots > \sigma_k$ are approximations of the first k largest Lyapunov exponents of the dynamics. In the case of regular motion, on the other hand, all deviation vectors tend to fall on the $N-$dimensional tangent space of the torus, where the motion is quasiperiodic. Thus, if we start with $k \leq N$ general deviation vectors, these will remain *linearly independent* on the $N-$dimensional tangent space of the torus, since there is no particular reason for them to become aligned. As a consequence, GALI_k in this case remains practically constant for $k \leq N$. On the other hand, for $k > N$, GALI_k tends to zero, since some deviation vectors will eventually become *linearly dependent*, following power laws that depend on the dimensionality of the torus. In the particular case, that there are s ($s \leq k$) of deviation vectors initially tangent to this torus the GALIs are given [106] by

$$\mathrm{GALI}_k(n) \propto \begin{cases} constant & \text{if } 2 \leq k \leq N \\ \frac{1}{n^{2(k-N)-s}} & \text{if } N < k \leq 2N \text{ and } 0 \leq s < k-N \\ \frac{1}{n^{k-N}} & \text{if } N < k \leq 2N \text{ and } s \geq k-N \end{cases} . \tag{2.89}$$

The formula for the calculation of the GALI_k, associated with quasiperiodic orbits lying on l–dimensional tori (following [21, 107]) is

$$\mathrm{GALI}_k(n) \propto \begin{cases} constant, & \text{if } 2 \leq k \leq l \\ \frac{1}{t^{k-l}}, & \text{if } l < k \leq 2N-l \\ \frac{1}{t^{2(k-N)}}, & \text{if } 2N-l < k \leq 2N \end{cases} . \tag{2.90}$$

An efficient way to compute the GALI_k, especially in cases where the dimension of the system N becomes large, based on the Singular Value Decomposition (SVD) [98], was proposed in [4, 107].

CHAPTER 3

APPLICATIONS OF DYNAMICAL INDICATORS TO SYSTEMS OF SYMPLECTIC MAPS

3.1 Introduction

In this chapter, we apply the Generalized Alignment Index (GALI) method to two types of dynamical behaviors, which are related to localization phenomena in multi–dimensional Hamiltonian systems, as well as symplectic maps. The first type refers to quasiperiodic oscillations in the vicinity of what is known as *discrete breathers*, or exact periodic solutions of multi–dimensional systems, which are exponentially localized in (real) space. The second class of phenomena concerns localization in Fourier space and is evidenced by the persistence of quasiperiodic recurrences in the neighborhood of normal mode oscillations of nonlinear lattices, observed for example in the famous numerical experiments performed by Fermi, Pasta and Ulam (FPU) in the early 1950's [38, 14, 40, 41, 2].

In the next section, we review the dynamics of the celebrated 2D standard map and then couple 2 and 3 of them together to form a system, on which we can test the effectiveness of our dynamical indicators (SALI and GALI) and verify the validity of the various asymptotic formulas for identifying ordered as well as chaotic motion. Then, in section 3.3, we form a system of N coupled standard maps and give evidence for the existence of both types of localization metioned above. First, starting with initial conditions localized in real space, we find low–dimensional quasiperiodic motion, which persists for very long times. We also study in this discrete model recurrences of its (linear) normal mode oscillations and find that, in contrast with the FPU model, the tori associated with them are not always low–dimensional. This may be due to the fact that, unlike the FPU example, each map contains on site nonlinear terms, which depend on its individual variables.

The standard map, also referred to as the Chirikov–Taylor map [75, 20], is an area preserving map, which appears in many physical problems. It is defined by the equations

$$\begin{aligned} x_{n+1} &= x_n + y_{n+1}, \\ y_{n+1} &= y_n + K\sin(x_n), \end{aligned} \tag{3.1}$$

where both variables are taken modulo one in the unit square. This map describes the motion of a simple mechanical system called a kicked rotator. It may be thought of as representing a pendulum rotating on a horizontal frictionless plane around a fixed axis and being periodically kicked by a nonlinear force at the other end, at unit time intervals. The variables x_n and y_n determine, respectively, the angular position of the pendulum and its angular momentum after the nth kick. The constant K measures the intensity of the nonlinear "kicks".

The standard map describes many systems occurring in the fields of mechanics, accelerator physics, plasma physics, and solid state physics. However, it is also interesting from a fundamental point of view, since it is a very simple model of a Hamiltonian system of 2 degrees of freedom that displays order chaos.

The Hamiltonian function of a system described by the standard map can be expressed as an infinite sum

$$H = \frac{1}{2}I^2 - K\cos\theta \sum_{n=-\infty}^{\infty} \delta(\frac{t}{T} - n). \tag{3.2}$$

This represents a model whose unperturbed Hamiltonian

$$H_0 = \frac{1}{2}I^2, \tag{3.3}$$

is affected by a periodic sequence of "kicks" (δ–pulses) with period

$$T = 2\pi/\nu. \tag{3.4}$$

Expression (3.3) corresponds either to a particle's free motion, $I = p$, $\theta = x$, or to a free rotator when the variable θ is cyclic, that is, $\theta \in (0, 2\pi)$. Let us consider the latter case. By using the identity

$$\sum_{-\infty}^{\infty} \delta(\frac{t}{T} - n) = \sum_{n=-\infty}^{\infty} \cos(2\pi n \frac{t}{T}), \tag{3.5}$$

we rewrite (3.2) in the following form

$$H = \frac{1}{2}I^2 - K\cos\theta \sum_{n=-\infty}^{\infty} \cos(m\nu t). \tag{3.6}$$

The Hamiltonian (3.6) can also be considered as a particular case of a more general Hamiltonian

$$H = \frac{1}{2}p^2 - \sum_m V_m \cos(k_m x - \omega_m t), \tag{3.7}$$

when $k_m = 1(\forall m)$, $V_m = V_0 = -K(\forall m)$, $\omega_m = m\nu$ and the sum in (3.7) is performed over $m \in (-1, 1)$. Thus, the Hamiltonian (3.2) corresponds to a particle motion in a periodic wave packet with an infinite number of harmonics of equal amplitude. The equations of motion derived from (3.2) have the form

$$\begin{aligned} \dot{I} &= -K\sin\theta \sum_{n=-\infty}^{\infty} \delta(\frac{t}{T} - n) \\ \dot{\theta} &= I \end{aligned} \tag{3.8}$$

Between two δ–pulses, $I = const$ and $\theta = It + const$. At each step, or "kick", the variable θ remains continuous and the action I changes by the value $-K\sin\theta$, which can be obtained by integrating

(3.8) with respect to time in a small vicinity of the δ–pulse. Let us assume that (I, θ) are the values of the variables just before the n^{th} kick, and that (I', θ') are the same values before the next $(n+1)^{th}$ "kick". It follows that the map, derived from (3.8), is

$$\begin{aligned} I' &= I - K\sin\theta \\ \theta' &= I' \end{aligned} \qquad (3.9)$$

which is equivalent to the equations of motion in (3.1).

For $K = 0$, there is no perturbation and the solution of (3.9) is trivial

$$I_n = const. = I_0, \qquad \theta = \theta_0 + nI_0. \qquad (3.10)$$

It describes a straight line in the phase plane (I, θ). As soon as $K \neq 0$, however, the dynamics change dramatically: All straight lines of the $K = 0$ case, with I_0 rational multiple of 2π (i.e. $I_0 = 2\pi l/m$ turn to a pair of periodic orbits (composed of m points each and covering the interval $0 < \theta < 2\pi$ l times), one of which is (linearly) stable and the other unstable. On the other hand, most I_0 =irrational lines are preserved according to the KAM theorem. As we will see in the next section, the stable periodic orbit are surrounded by tori forming small ellipses of quasiperiodic motion in their immediate neighborhoods, while the unstable periodic points are of saddle type and possess chaotic orbits in their vicinity.

3.2 Global Dynamics of the $2N$–D Standard Map

As a simple 2D map which exhibits regular and chaotic behavior, we consider the well–known standard map [20, 61] in the form

$$\begin{array}{l} x_1^{'} = x_1 + x_2^{'} \\ x_2^{'} = x_2 + \frac{K}{2\pi}\sin(2\pi x_1) \end{array} \quad (mod\ 1)\ , \qquad (3.11)$$

where K is the strength of the nonlinearity of the system.

Before studying the global dynamics of map (3.11) let us examine in more detail the behavior of SALI for regular and chaotic orbits of a 2D map. In the case of a chaotic orbit, any two deviation vectors will be aligned to the direction defined by the largest Lyapunov exponent σ_1, and consequently SALI will tend to zero following an exponential decay of the form SALI $\propto e^{-2\sigma_1 n}$ (since SALI$\propto$GALI$_2$), with n being the number of iterations. As we have mentioned, in the case of regular orbits any two deviation vectors tend to fall on the tangent space of the torus on which the motion lies [104, 109, 107]. For a 2D map this torus is a 1–dimensional invariant curve, whose tangent space is also 1–dimensional and consequently the two deviation vectors will become aligned. Thus, even in the case of regular orbits in 2D maps the SALI tends to zero. This decay follows a power law having the form SALI $\propto 1/n^2$ [104, 107].

In Fig. 3.1 we see the different behavior of SALI for regular and chaotic orbits of the standard map (3.11). It is exactly this different behavior of the index that allows us to use SALI for a fast and clear distinction between regions of chaos and order in the 2–dimensional phase space of the standard map. From the results of Fig. 3.1 and the theoretical predictions for the evolution of SALI we see that after $n = 500$ iterations the value of SALI of a regular orbit becomes of the order of 10^{-6}, while for a chaotic orbit SALI has already reached extremely small values. Suppose now that we wish to estimate the percentage of chaotic orbits (as we will do for the galaxy models in the next chapter) for a given value of K. This can be computed as follows: We compute the

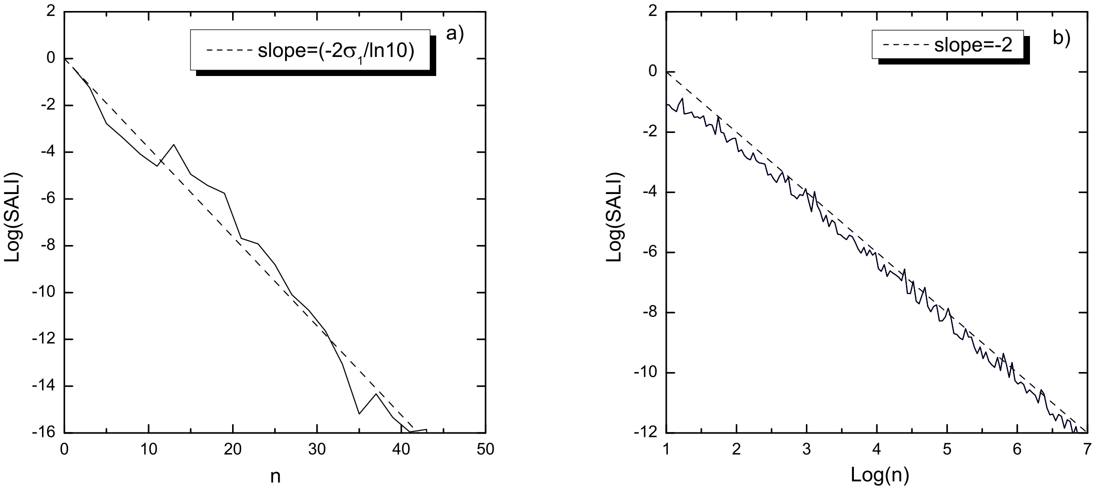

Figure 3.1: The evolution of SALI (solid lines) for a) the chaotic orbit with initial condition $x_1 = 0.2$, $x_2 = 0.2$ and b) the regular orbit with initial condition $x_1 = 0.4$, $x_2 = 0.8$ of the standard map (3.11) for $K = 2$, with respect to the number of iterations n. Note the different scales of the horizontal axis. The largest Lyapunov exponent of the chaotic orbit is $\sigma_1 \approx 0.438$. Dashed curves in panels a) and b) correspond to functions proportional to $e^{-2\sigma_1 n}$ and $1/n^2$ respectively. It is evident that the theoretical predictions for the evolution of SALI describe very well the numerical data.

evolution of orbits whose initial conditions lie on a 2–dimensional grid of 1000×1000 equally spaced points on the 2–dimensional phase space of the map (dividing in this way the (x_1, x_2)–plane in 10^6 squares) and register for each orbit the value of SALI after $n = 500$ iterations. All orbits having values of SALI significantly smaller than 10^{-6} (which correspond to the value SALI reaches after 500 iterations in the case of regular orbits), are characterized as chaotic. In practice as a good threshold for this distinction we consider the value 10^{-8}. Thus, all orbits having SALI $\leq 10^{-8}$ after $n = 500$ iterations are characterized as chaotic, while all others are considered as non–chaotic.

In Fig. 3.2a) we present the outcome of this procedure for $K = 2$. Chaotic orbits, having SALI $\leq 10^{-8}$ are colored black, while light gray color corresponds to regular orbits having high values of SALI. Thus, in Figure 3.2a) we can identify clearly even tiny regions of regular motion which are not easily seen in phase space portraits of the map (Fig. 3.2b)). Using the above–described method we were able to compute very fast and accurately the percentages of regular motion for large values of parameter K. In Fig. 3.3a) we plot the percentage of regular orbits for $180 \leq K \leq 200$ where K varies with a step $\delta K = 0.001$. A blow–up of the peak appearing close to $K = 188$ is seen in Fig. 3.3b).

In order to accelerate the numerical computation we applied the following technique: For each orbit we compute its SALI value at $n = 500$, keeping also track of the squares on the (x_1, x_2)–plane that the orbit visits in its evolution. Then, we attribute the same SALI value to all these squares. In this way we gain considerably in computational time, since it is not necessary to perform the same computation for the total number of the initial conditions. For each value of K a grid of 1000×1000 initial conditions were used, allowing us to detect extremely tiny regions of regular

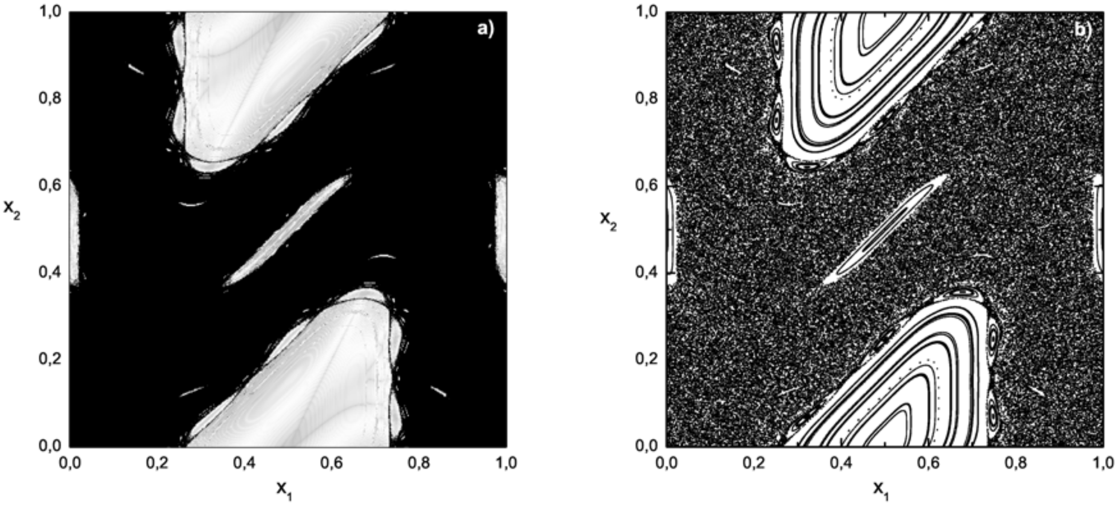

Figure 3.2: a) Regions of different values of SALI after $n = 500$ iterations of map (3.11) for $K = 2$. The gray color corresponds to regions of order while the black to chaotic. b) Phase space portrait of map (3.11) for the same value of K.

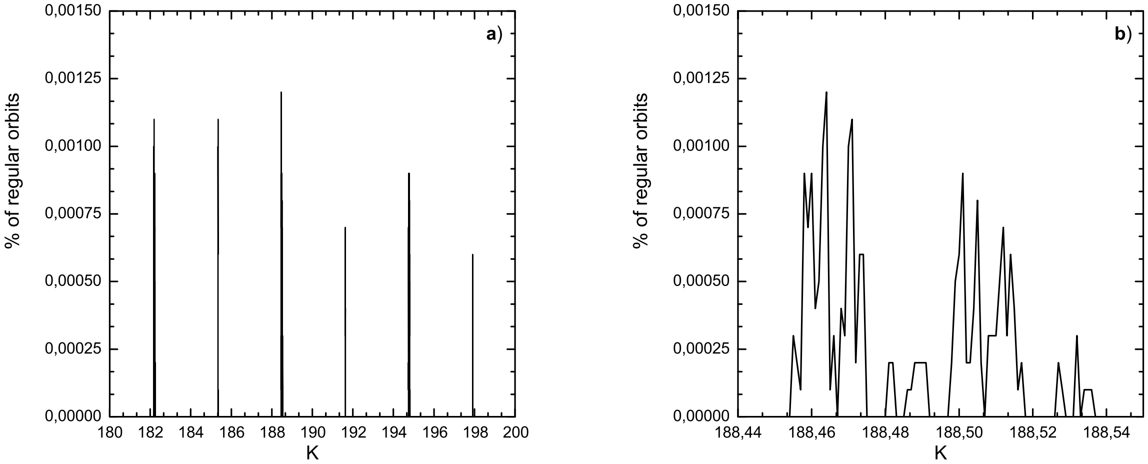

Figure 3.3: a) Percentages of regular orbits of map (3.11) as a function of the nonlinear parameter $K \in [180, 200]$, b) A zoom of panel a) in the region of $K \in (188.44, 188.55)$.

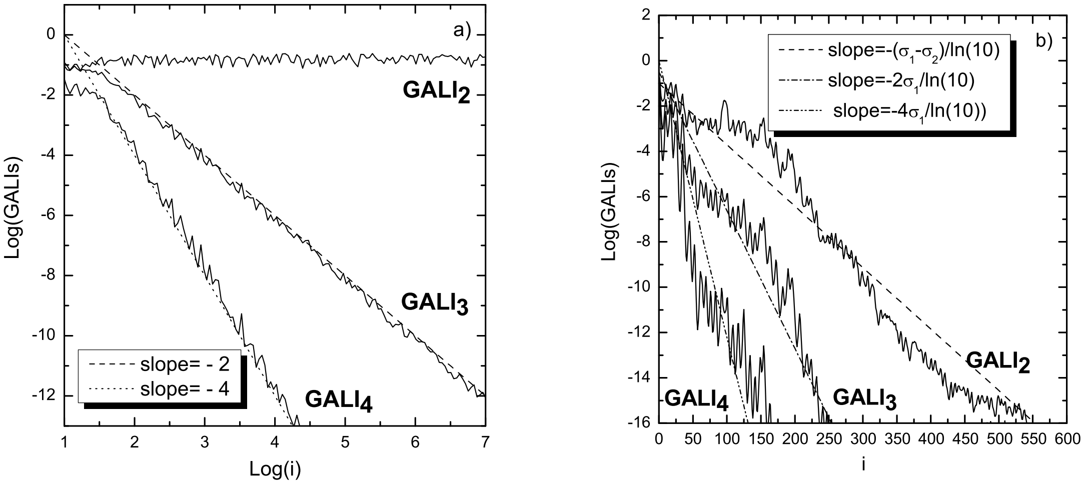

Figure 3.4: The evolution of GALI_k, $k = 2, 3, 4$, with respect to the number of iterations i for a) the regular orbit R and b) the chaotic orbit C. The plotted lines correspond to functions proportional to n^{-2}, n^{-4} in a) and to $e^{-(\sigma_1-\sigma_2)n}$, $e^{-2\sigma_1 n}$, $e^{-4\sigma_1 n}$ for $\sigma_1 = 0.070$, $\sigma_2 = 0.008$ in b).

motion (note that the percentages of regular orbits in Fig. 3.3 remain always less than 0.0015%!).

From the results of Fig. 3.3 we see a periodicity of period 2π in the appearance of islands of stability as K varies, in accordance to the results presented in [34]. In our study we were able to reproduce the results obtained in [34] but with considerably *less computational effort*. For example, for $K = 2$, instead of using all the 10^6 initial conditions of the 1000×1000 grid, it was efficient to compute the evolution of only 12425 initial conditions up to $n = 500$ iterations, for characterizing the total 10^6 points. Thus, for $K = 2$ we were able to determine the percentage of regular orbits on a 1000×1000 grid mesh by the computation of only $3 \times 500 \times 12425 \approx 2 \cdot 10^7$ iterations of the map (3.11) and its tangent map, instead for the $5 \cdot 10^9$ iterations needed for obtaining the same result in [34]. In particular for the computation of the data of Fig. 3.3 we needed only 27 hours of CPU time on an Athlon 64bit, 3.2GHz PC.

A similar study can also be implemented for the 4D standard map, described by the following equations

$$\begin{aligned} x_1' &= x_1 + x_2' \\ x_2' &= x_2 + \frac{K}{2\pi}\sin(2\pi x_1) - \frac{\beta}{\pi}\sin[2\pi(x_3 - x_1)] \\ x_3' &= x_3 + x_4' \qquad\qquad (mod\ 1), \\ x_4' &= x_4 + \frac{K}{2\pi}\sin(2\pi x_3) - \frac{\beta}{\pi}\sin[2\pi(x_1 - x_3)] \end{aligned} \tag{3.12}$$

where K is again the parameter of nonlinearity and β the so–called coupling parameter of the system.

In the first part of our study we fix the parameters of the map (3.12) to $K = 0.5$ and $B = 0.05$. In Fig. 3.4, we show the behavior of GALIs for two different orbits: a regular orbit R with initial conditions $(x_1, x_2, x_3, x_4) = (0.55, 0.10, 0.54, 0.01)$ (Fig. 3.4a), and a chaotic orbit C with initial

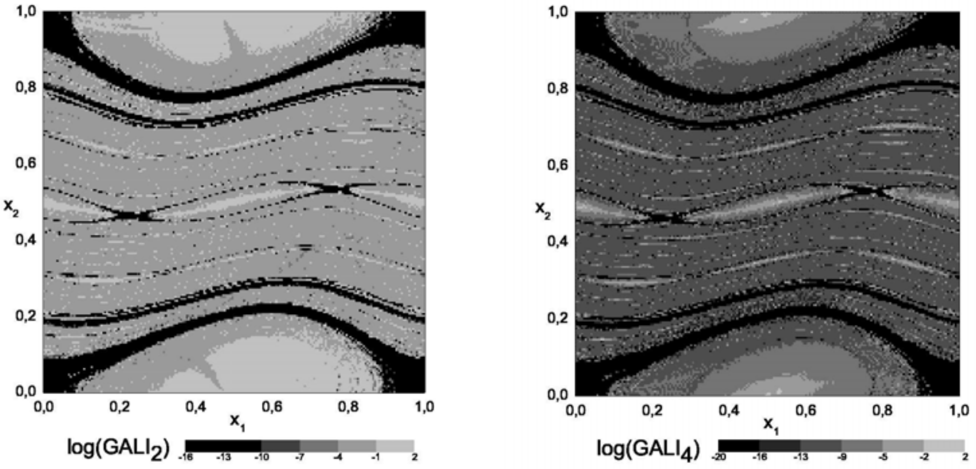

Figure 3.5: Regions of different values of the GALI_2 (left panel) and GALI_4 (right panel) for a grid of 500×500 initial conditions on the subspace $x_3 = 0.54$, $x_4 = 0.01$ of map (3.12) for $K = 0.5$ and $B = 0.05$.

conditions $(x_1, x_2, x_3, x_4) = (0.55, 0.10, 0.005, 0.01)$ (Fig. 3.4b). The positive Lyapunov exponents of orbit C were found to be $\sigma_1 \approx 0.070$, $\sigma_2 \approx 0.008$. From the results of Fig. 3.4 we see that the evolution of GALIs is described very well by the theoretically obtained approximations presented in Sect. 2.3.4. Let us now turn our attention to the study of the global dynamics of map (3.12). From the results Fig. 3.4 we conclude that in the case of 4D maps, GALI_2 has different behavior for regular and chaotic orbits. In particular, GALI_2 tends exponentially to zero for chaotic orbits ($\text{GALI}_2 \sim e^{-(\sigma_1-\sigma_2)n}$) while it fluctuates around non–zero values for regular orbits. This difference in the behavior of the index can be used to obtain a clear distinction between regular and chaotic orbits. Let us illustrate this by following up to $n = 4000$ iterations, all orbits whose initial conditions lie on a 2–dimensional grid of 500×500 equally spaced points on the subspace $x_3 = 0.54$, $x_4 = 0.01$, of the 4–dimensional phase space of the map (3.12), attributing to each grid point a color according to the value of GALI_2 at the end of the evolution. If GALI_2 of an orbit becomes less than 10^{-10} for $n < 4000$ the evolution of the orbit is stopped, its GALI_2 value is registered and the orbit is characterized as chaotic. The outcome of this experiment is presented in the left panel of Fig. 3.5.

But also GALI_4 can be used for discriminating regular and chaotic motion. From the theoretical predictions for the evolution of GALI_4, we see that after $n = 1000$ iterations the value of GALI_4 of a regular orbit should become of the order of 10^{-16}, since $\text{GALI}_4 \sim n^{-4}$, although the results of Fig. 3.4 show that more iterations are needed for this threshold to be reached, due to an initial transient time where GALI_4 does not decrease significantly. On the other hand, for a chaotic orbit GALI_4 has already reached extremely small values at $i = 1000$ due to its exponential decay ($\text{GALI}_4 \sim e^{-4\sigma_1 n}$). Thus, the global dynamics of the system can be revealed as follows: we follow the evolution of the same orbits as in the case of GALI_2 and register for each orbit the value of GALI_4 after $n = 1000$ iterations. All orbits having values of GALI_4 significantly smaller than 10^{-16} are characterized as chaotic, while all others are considered as non–chaotic. In the right panel of Fig. 3.5 we present the outcome of this procedure.

From the results of Fig. 3.5, we see that both procedures, using GALI_2 or GALI_4 as a chaos

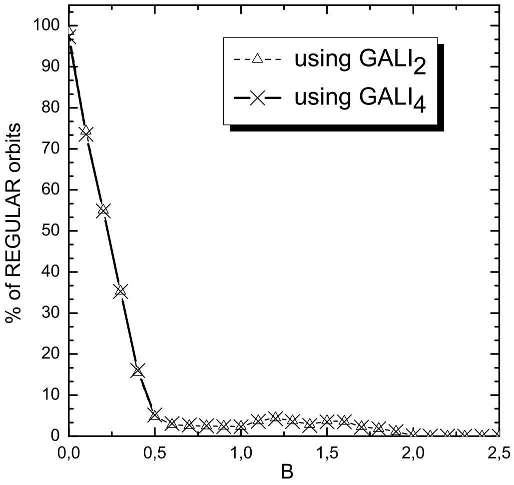

Figure 3.6: Percentages of regular orbits on the subspace $x_3 = 0.54$, $x_4 = 0.01$ of map (3.12) for $K = 0.5$, as a function of the parameter $B \in [0, 2.5]$.

indicator, give the same result for the global dynamics of the system, since in both cases 16% of the orbits are characterized as chaotic. These orbits correspond to the black colored areas in both panels of Fig. 3.5. One important difference between the two procedures is their computational efficiency. Even though GALI$_4$ requires the computation of four deviation vectors, instead of only two that are needed for the evaluation of GALI$_2$, using GALI$_4$ we were able to get a clear dynamical 'chart', not only for less iterations of the map (1000 instead of 4000 needed for GALI$_2$), but also in less CPU time. In particular, for the computation of the data of the left panel of Fig. 3.5 (using GALI$_2$) we needed 1 hour of CPU time on an Athlon 64bit, 3.2GHz PC, while for the data of the left panel of the same figure (using GALI$_4$) only 14 minutes of CPU time were needed.

Using the above–described method, both for GALI$_2$ and GALI$_4$, we were able to compute very fast and accurately the percentages of regular motion for several values of parameter β. In Fig. 3.6 we plot the percentage of regular orbits for $\beta \in [0, 2.5]$ where β varies with a step $\delta\beta = 0.1$. We see that the two curves practically coincide, but using GALI$_2$ we needed almost four times more CPU time. So, it becomes evident that a well–tailored application of GALI$_k$, with $2 < k$, can significantly diminish the CPU time required for the detailed 'charting' of phase space regions, compared with that for GALI$_2$.

In Fig. 3.7a),b), we present the evolution of the SALI both for regular and chaotic orbits, for $K = 3$ and $\beta = 0.1$. For the regular orbit of Fig. 3.7a) SALI fluctuates around a non–zero value, while for the chaotic orbit of Fig. 3.7b) SALI decays exponentially to zero reaching extremely small values after only a few iterations ($N \approx 150$), following the exponential law: SALI $\propto e^{-(\sigma_1 - \sigma_2)n}$, with σ_1, σ_2 being the two largest Lyapunov exponents of the orbit.

We were also able to measure the percentages of chaotic and regular orbits for the 4D standard map following a procedure similar to the one used in the case of the 2D map. We considered 10^6 initial conditions equally spaced in the 4–dimensional phase space of the system, producing in this way a fine grid of 4–dimensional hypercubes. Noting that in the case of chaotic orbits only a few hundreds of iterations are needed for SALI to reach the numerical accuracy of a computer, i.e. SALI $\approx 10^{-16}$ (in the case of the orbits of Fig. 3.7b) 150 iterations were sufficient), we started

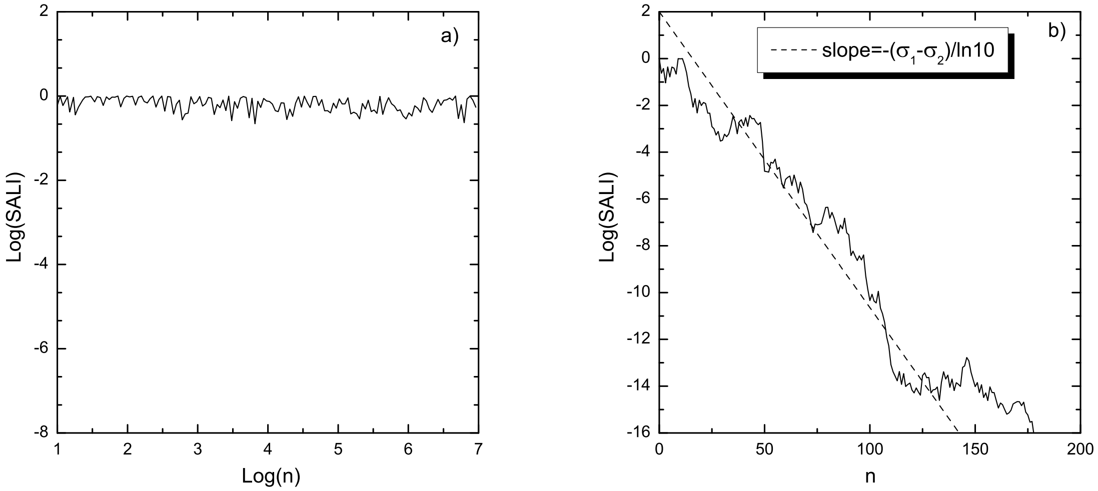

Figure 3.7: The evolution of the SALI for a) the regular orbit with initial condition $(x_1, x_2, x_3, x_4) = (0.55, 0.1, 0.62, 0.2)$ and b) the chaotic orbit with initial condition $(x_1, x_2, x_3, x_4) = (0.55, 0.3, 0.62, 0.2)$ of the 4D standard map with $K = 3$ and $\beta = 0.1$. We note that the SALI of the chaotic orbit decays exponentially to zero following the law $\propto e^{-(\sigma_1-\sigma_2)n}$, with $\sigma_1 \approx 0.744$, $\sigma_2 \approx 0.453$ being the two largest Lyapunov exponents of the orbit.

our computation by integrating orbits for only 500 iterations. For each orbit we also kept track of the 4–dimensional hypercubes it visited in its evolution. If the studied orbit was regular, i.e. its final SALI value was larger than 10^{-8}, its final SALI value was attributed to all the hypercubes visited by the orbit. If, on the other hand, the orbit was characterized as chaotic (i.e. its SALI value became $\leq 10^{-8}$), the evolution of the orbit (but not the evolution of the variational equations) was extended to 5000 iteration, allowing us to attribute the computed SALI value to many hypercubes. This procedure decreases significantly the CPU time needed for the reliable computation of the percentage of regular motion. In particular for $K = 3$ and $\beta = 0.1$ the percentage of regular motion was found to be 8, 7%, after only 1 minute of computations with the same computer used in the 2D case.

Finally, let us apply our dynamical indicators to study the global behavior of 3 coupled standard maps, described by the equations

$$\begin{array}{rcl} x_1' &=& x_1 + x_2' \\ x_2' &=& x_2 + \frac{K}{2\pi}\sin(2\pi x_1) - \frac{\beta}{2\pi}\{\sin[2\pi(x_5 - x_1)] + \sin[2\pi(x_3 - x_1)]\} \\ x_3' &=& x_3 + x_4' \\ x_4' &=& x_4 + \frac{K}{2\pi}\sin(2\pi x_3) - \frac{\beta}{2\pi}\{\sin[2\pi(x_1 - x_3)] + \sin[2\pi(x_5 - x_3)]\} \\ x_5' &=& x_5 + x_6' \\ x_6' &=& x_6 + \frac{K}{2\pi}\sin(2\pi x_5) - \frac{\beta}{2\pi}\{\sin[2\pi(x_1 - x_5)] + \sin[2\pi(x_3 - x_5)]\} \end{array} \qquad (3.13)$$

where again each coordinate is taken modulo 1 and we fix the parameters of the map (3.13) to $K = 3$ and $\beta = 0.1$.

In order to verify numerically the validity of equations (2.88) and (2.90) we consider two typical orbits of map (3.13), a chaotic one with initial condition $x_1 = x_3 = x_5 = 0.8$, $x_2 = 0.05$, $x_4 = 0.21$,

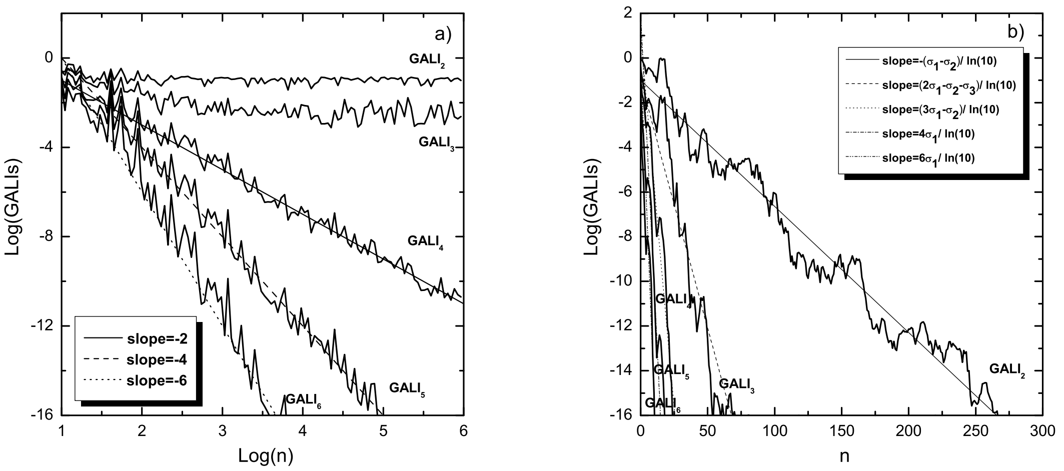

Figure 3.8: The evolution of GALI$_k$, $k = 2, \ldots, 6$, with respect to the number of iteration n for a) the regular orbit R1 and b) the chaotic orbit C1. The plotted lines correspond to functions proportional to n^{-2}, n^{-4}, n^{-6} in a) and proportional to $e^{-(\sigma_1-\sigma_2)t}$, $e^{-(2\sigma_1-\sigma_2-\sigma_3)t}$, $e^{-(3\sigma_1-\sigma_2)t}$, $e^{-4\sigma_1 t}$, $e^{-6\sigma_1 t}$ for $\sigma_1 = 0.70$, $\sigma_2 = 0.57$, $\sigma_3 = 0.32$ in b).

$x_6 = 0.01$ (orbit C1) and a regular one with initial condition $x_1 = x_3 = x_5 = 0.55$, $x_2 = 0.05$, $x_4 = 0.01$, $x_6 = 0$ (orbit R1). In Fig. 3.8 we see the evolution of GALI$_k$, $k = 2, \ldots, 6$, for these two orbits. It is well–known that in the case of symplectic maps the Lyapunov exponents are ordered in pairs of opposite signs [75]. Thus, for a chaotic orbit of the 6D map (3.13) we have $\sigma_1 = -\sigma_6$, $\sigma_2 = -\sigma_5$, $\sigma_3 = -\sigma_4$ with $\sigma_1 \geq \sigma_2 \geq \sigma_3 \geq 0$. So for the evolution of GALI$_k$, equation (2.88) gives

$$\begin{gathered} \mathrm{GALI}_2(t) \propto e^{-(\sigma_1-\sigma_2)t}, \;\; \mathrm{GALI}_3(t) \propto e^{-(2\sigma_1-\sigma_2-\sigma_3)t}, \\ \mathrm{GALI}_4(t) \propto e^{-(3\sigma_1-\sigma_2)t}, \;\; \mathrm{GALI}_5(t) \propto e^{-4\sigma_1 t}, \;\; \mathrm{GALI}_6(t) \propto e^{-6\sigma_1 t}. \end{gathered} \tag{3.14}$$

The positive Lyapunov exponents of the chaotic orbit C1 were found to be $\sigma_1 \approx 0.70$, $\sigma_2 \approx 0.57$, $\sigma_3 \approx 0.32$. From the results of Fig. 3.8a) we see that the functions of equation (3.14) for $\sigma_1 = 0.70$, $\sigma_2 = 0.57$, $\sigma_3 = 0.32$ approximate quite accurately the computed values of GALIs.

For the regular orbit R1 we first considered the general case where no initial deviation vector is tangent to the torus where the orbit lies. Thus, for the behavior of GALI$_k$, $k = 2, \ldots, 6$, Eq. (2.90) yields for $m = 0$

$$\begin{gathered} \mathrm{GALI}_2(t) \propto \text{constant}, \;\; \mathrm{GALI}_3(t) \propto \text{constant}, \;\; \mathrm{GALI}_4(t) \propto \tfrac{1}{t^2}, \\ \mathrm{GALI}_5(t) \propto \tfrac{1}{t^4}, \;\; \mathrm{GALI}_6(t) \propto \tfrac{1}{t^6}. \end{gathered} \tag{3.15}$$

From the results of Fig. 3.8b) we see that the approximations appearing in (3.15) describe very well the evolution of GALIs.

In order to verify the validity of equation (2.90) for $1 \leq m \leq 3$, in the case of regular motion, we evolve orbit R1 and three random initial deviation vectors for a large number of iterations (in our case for 5×10^7 iterations), in order for the three deviation vectors to fall on the tangent space of the torus. Considering the current coordinates of the orbit as initial conditions and using $m = 1$ or $m = 2$ or $m = 3$ of these vectors (that lie on the tangent space of the torus) as initial deviation vectors we start the computation of GALIs' evolution. We note that the rest $6-m$ initial deviation vectors needed for our computation are randomly generated so that they do not lie on the tangent space of the torus. The results of these procedures are presented in Fig. 3.9, where the evolution of GALI_k, $k = 2, \dots, 6$, for different values of m is plotted. Fig. 3.9 clearly illustrate that equation (2.90) describes accurately the behavior of GALIs for regular motion also in the case that some of the initial deviation vectors are initially in the tangent space of the torus where the regular motion takes place.

Let us now consider the case of a chaotic orbit which visits different chaotic regions in the phase space of the map. The orbit with initial conditions $x_1 = x_3 = x_5 = 0.55$, $x_2 = 0.05$, $x_4 = 0.21$, $x_6 = 0.0$ (orbit C2) exhibits this behavior as can be seen from the projections of its first 1000 successive consequents on different 2–dimensional planes plotted in Fig. 3.10.

The projections look erratic, indicating that the orbit is chaotic. We also observe that in all three projections the orbits stays 'trapped' for some iterations in oval–shaped regions and later on goes away entering the big chaotic sea around these regions. This behavior is also depicted in the evolution of the Lyapunov exponents of the orbit (Fig. 3.11a)). The three positive Lyapunov exponents seem to fluctuate around $\sigma_1 \approx 0.033$, $\sigma_2 \approx 0.02$, $\sigma_3 \approx 0.005$ for about 1000 iterations exhibiting 'jumps' to higher values when the orbit enters the big chaotic sea, stabilizing around $\sigma_1 \approx 0.793$, $\sigma_2 \approx 0.624$, $\sigma_3 \approx 0.365$.

Let us now study how the behavior of GALIs is influenced by the fact that orbit C2 visits two different regions of chaoticity characterized by different values of Lyapunov exponents. Since, C2 is a chaotic orbit its GALIs should tend exponentially to zero following the laws of equation (3.14). Starting the computation of GALI_k, $k = 2, \dots, 6$, from the initial point of C2, when the orbit is located in the first chaotic sea, we see that the exponential decay of GALIs is well described by Eq. (3.14) using for σ_1, σ_2, σ_3 the approximate values of the Lyapunov exponents of the first chaotic region (Fig. 3.11b)). On the other hand, using as initial condition of the chaotic orbits its coordinates after 10^6 iterations, when the orbit is located in the second chaotic region, the evolution of GALIs is well approximated by equation (3.14) but for $\sigma_1 = 0.793$, $\sigma_2 = 0.624$, $\sigma_3 = 0.365$, which are the approximations of the Lyapunov exponents of the big chaotic sea (Fig. 3.11c)). So we the σ_i, $i = 1, \dots, k$ used in equation (3.14) are good approximations of the first k Lyapunov exponents of the chaotic region in which the orbit evolves.

3.3 Application to the Dynamics of Coupled Standard Maps

Let us now consider a system of N coupled standard maps described by the following equations

$$\begin{aligned} x^j_{n+1} &= x^j_n + y^j_{n+1}, \\ y^j_{n+1} &= y^j_n + \frac{K_j}{2\pi}\sin(2\pi x^j_n) - \frac{\beta}{2\pi}\{\sin[2\pi(x^{j+1}_n - x^j_n)] + \sin[2\pi(x^{j-1}_n - x^j_n)]\} \end{aligned} \tag{3.16}$$

with $j = 1, ..., N$, fixed boundary conditions $x_0 = x_{N+1} = 0$ and β the coupling parameter between neighboring maps. In what follows, we shall examine the localization properties of this system comparing the dynamics with what is observed when one studies a one–dimensional Hamiltonian system like the FPU lattice.

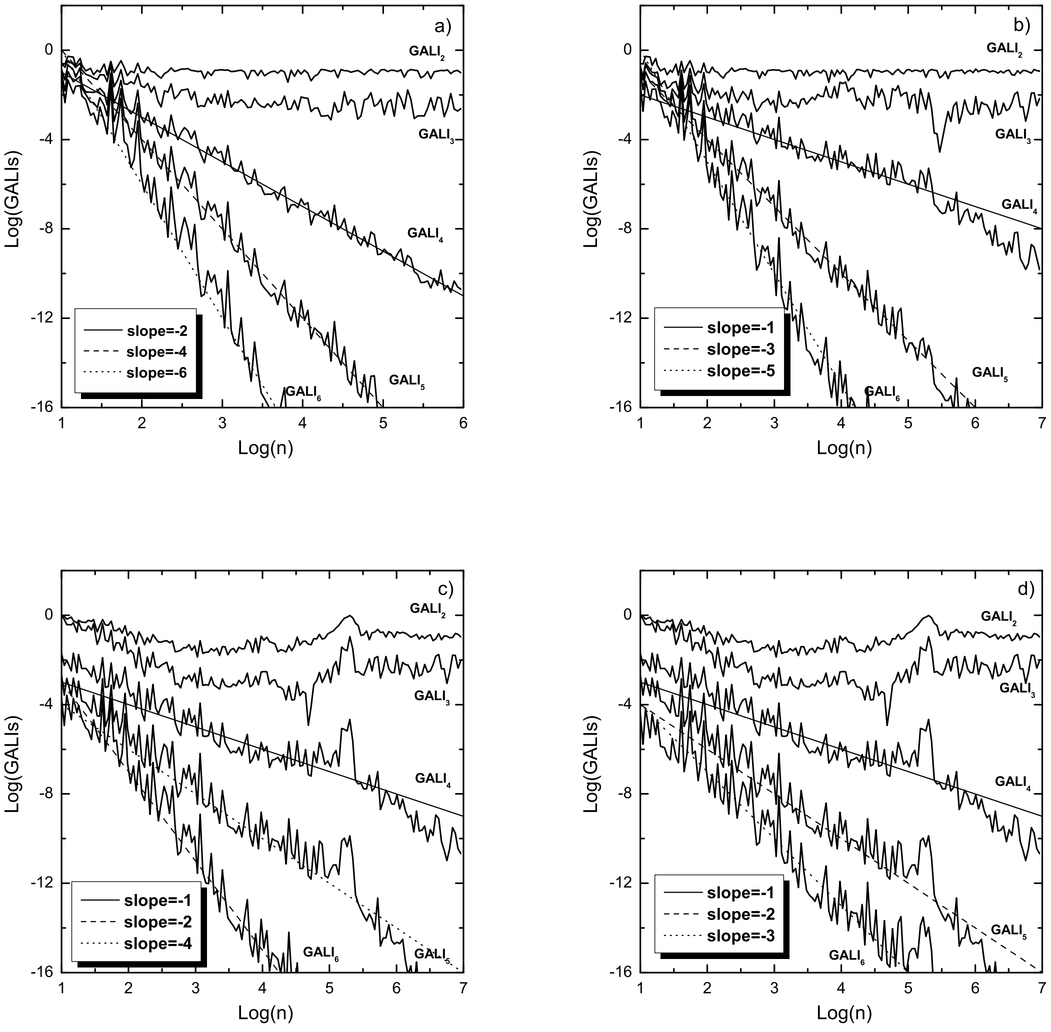

Figure 3.9: Evolution of GALI$_k$, $k = 2, \ldots, 6$, for the regular orbit R1 on a log–log scale, for different values of the number m of deviation vectors initially tangent on the torus on which the motion occurs: a) $m = 0$, b) $m = 1$, c)$m = 2$ and d)$m = 3$. In every panel lines corresponding to particular power laws are also plotted.

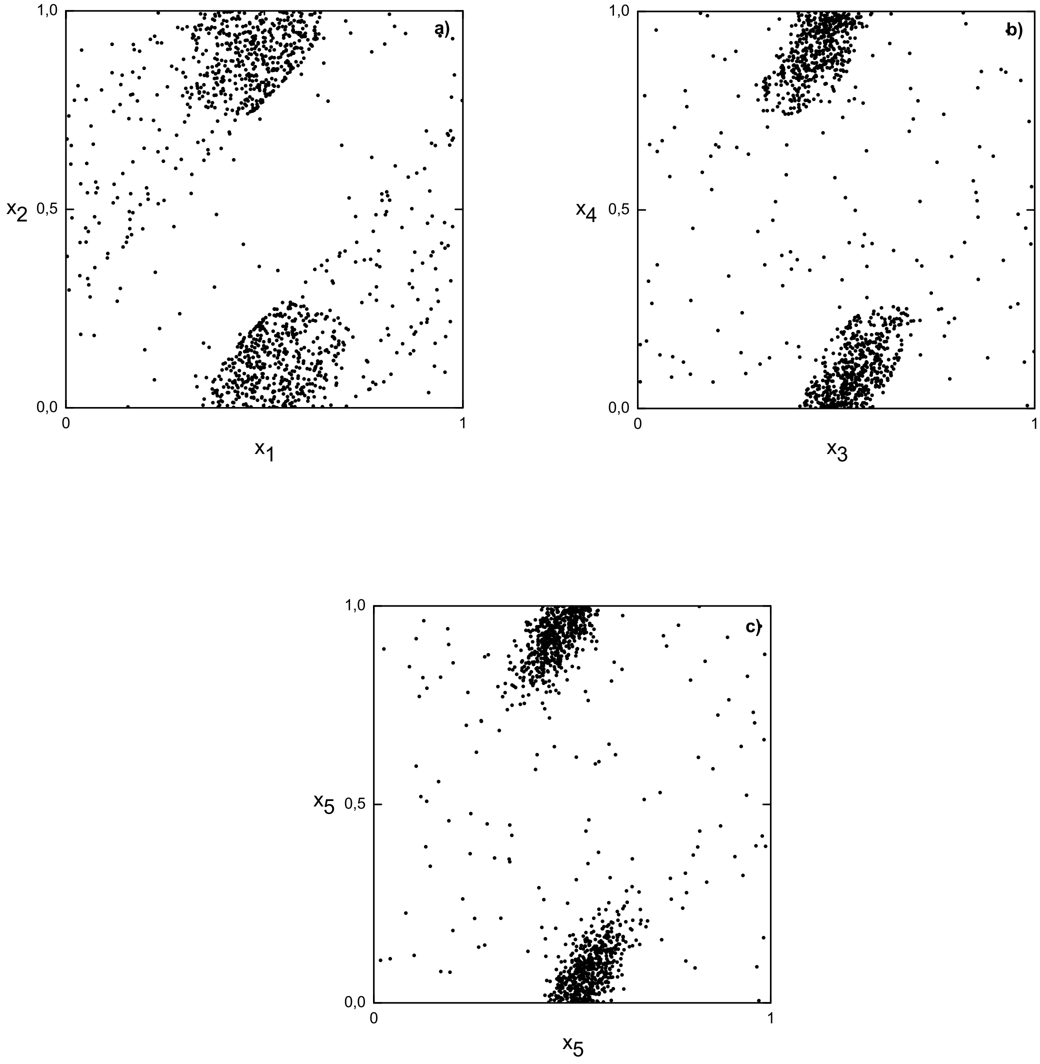

Figure 3.10: Projections on the planes a) (x_1, x_2), b) (x_3, x_4) and c) (x_5, x_6) of the first 1000 successive points of the chaotic orbit C2

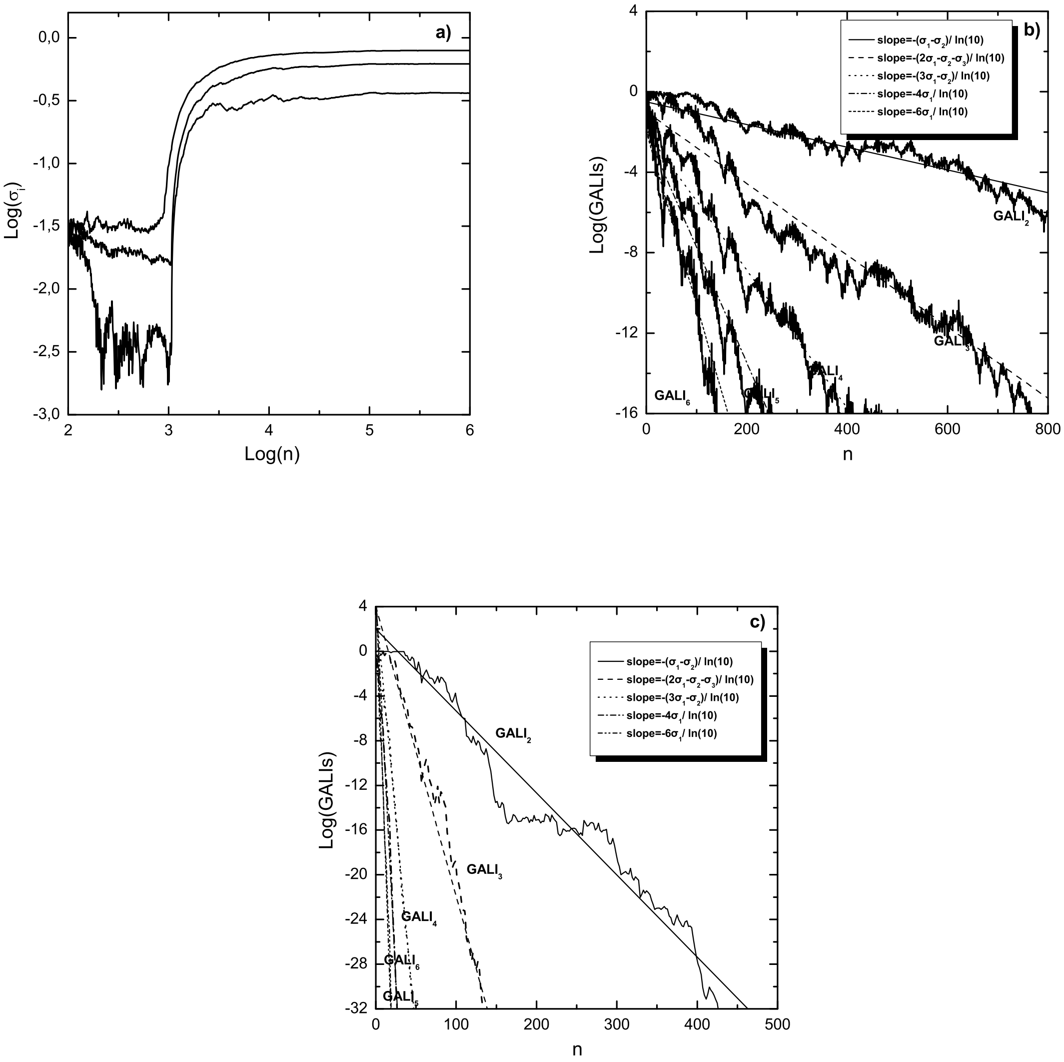

Figure 3.11: a) The evolution of the three positive Lyapunov exponents of the chaotic orbit C2. The evolution of GALI_k, $k = 2, \ldots, 6$, with respect to the number of iteration n for the same orbit when we use as initial condition of the orbit its coordinates at b) $n = 0$ and at c) $n = 10^6$ iterations. The plotted lines in b) and c) correspond to functions proportional to $e^{-(\sigma_1-\sigma_2)t}$, $e^{-(2\sigma_1-\sigma_2-\sigma_3)t}$, $e^{-(3\sigma_1-\sigma_2)t}$, $e^{-4\sigma_1 t}$, $e^{-6\sigma_1 t}$ for $\sigma_1 = 0.033$, $\sigma_2 = 0.02$, $\sigma_3 = 0.005$ in b) and $\sigma_1 = 0.793$, $\sigma_2 = 0.624$, $\sigma_3 = 0.365$ in c).

3.3.1 Initial conditions localized in real space

Let us begin with the question of the existence of stable discrete breathers in this model, when the coupling parameter β is small. Note that our equations have an exact stable fixed point, when all particles are located at $(x, y) = (0.5,0.0)$ (see Fig. 3.2). Taking $N = 20$ coupled standard maps, we may, therefore, look for localized oscillations taking as initial condition (R1): $(x_j, y_j) = (0.5,0.0)$, $\forall j \neq 11$, perturbing only one particle at $(x_{11}, y_{11}) = (0.65, 0.0)$ and fixing the parameters $\beta = 0.001$, setting $K_j = 2$, with $j = 1, ..., 20$. If a stable discrete breather exists, the orbits are expected to oscillate about these initial conditions quasiperiodically for very long times.

Indeed, when we evaluate the GALI$_k$ indices for $n = 10^6$ iterations in Fig. 3.12a and display their evolution for $k = 2, ..., 7$ on a logarithmic scale, we find that GALI$_2$ fluctuates around a non–zero value while all the other GALIs decay to zero following power laws. This implies that the motion is that of a quasiperiodic orbit that lies on a 2–dimensional (2D) torus. In fact, for initial conditions (R2): (x_j, y_j)=(0.5,0.0), $\forall j \neq 11, 12$, perturbing two particles $(x_{11}, y_{11}) = (0.65, 0.0)$, $(x_{12}, y_{12}) = (0.55, 0.0)$ for the same parameters as in the R1 experiment, we detected regular motion that lies on a 3D torus! This is demonstrated by the evolution of the GALIs in Fig. 3.12, where not only GALI$_2$ but also GALI$_3$ fluctuates around a non–zero value.

Such localized regular dynamics becomes evident in Fig. 3.12c, where we exhibit the oscillations of the x_n–coordinate of the 11^{th}, 12^{th} and 13^{th} maps of the system for the last 10^5 iterations of the R2 experiment. As seen in the figure, the motion is indeed quasiperiodic and confined to the middle 3 maps, as all other degrees of freedom do not gain any significant amount of energy. Similarly, we have observed that exciting 3 central particles ($j = 10, 11, 12$) gives a quasiperiodic motion on 4D tori. This is reminiscent of the motion near discrete breathers of Hamiltonian systems and suggests that the excitation of each particle adds one extra frequency to the motion.

3.3.2 Initial conditions localized in Fourier space

Finally, let us investigate the phenomenon of FPU recurrences in our system of coupled standard maps. To do this, we first need to derive the linear normal modes of the model, in order to choose initial conditions that will excite only a small number of them. Thus, keeping only the first term in the Taylor expansion of the *sine*–function in (3.16), we obtain the following system of equations

$$x' = \mathcal{A}x, \tag{3.17}$$

where $x' = (x^1_{n+1}, y^1_{n+1}, ..., x^N_{n+1}, y^N_{n+1})^T$, $x = (x^1_n, y^1_n, ..., x^N_n, y^N_n)^T$ and

$$\mathcal{A} = \begin{bmatrix} K_1+\gamma & 1 & -\beta & 0 & \dots & 0 & 0 & 0 & 0 & 0 \\ K_1+2\beta & 1 & -\beta & 0 & \dots & 0 & 0 & 0 & 0 & 0 \\ -\beta & K_2+\gamma & 1 & -\beta & \dots & 0 & 0 & 0 & 0 & 0 \\ -\beta & K_2+2\beta & 1 & -\beta & \dots & 0 & 0 & 0 & 0 & 0 \\ \vdots & \vdots & \vdots & \vdots & & \vdots & \vdots & \vdots & \vdots & \\ 0 & 0 & 0 & 0 & \dots & -\beta & K_{N-1}+\gamma & 1 & -\beta & 0 \\ 0 & 0 & 0 & 0 & \dots & -\beta & K_{N-1}+2\beta & 1 & -\beta & 0 \\ 0 & 0 & 0 & 0 & \dots & 0 & 0 & -\beta & K_N+\gamma & 1 \\ 0 & 0 & 0 & 0 & \dots & 0 & 0 & -\beta & K_N+2\beta & 1 \end{bmatrix}, \tag{3.18}$$

with $\gamma = 1 + 2\beta$.

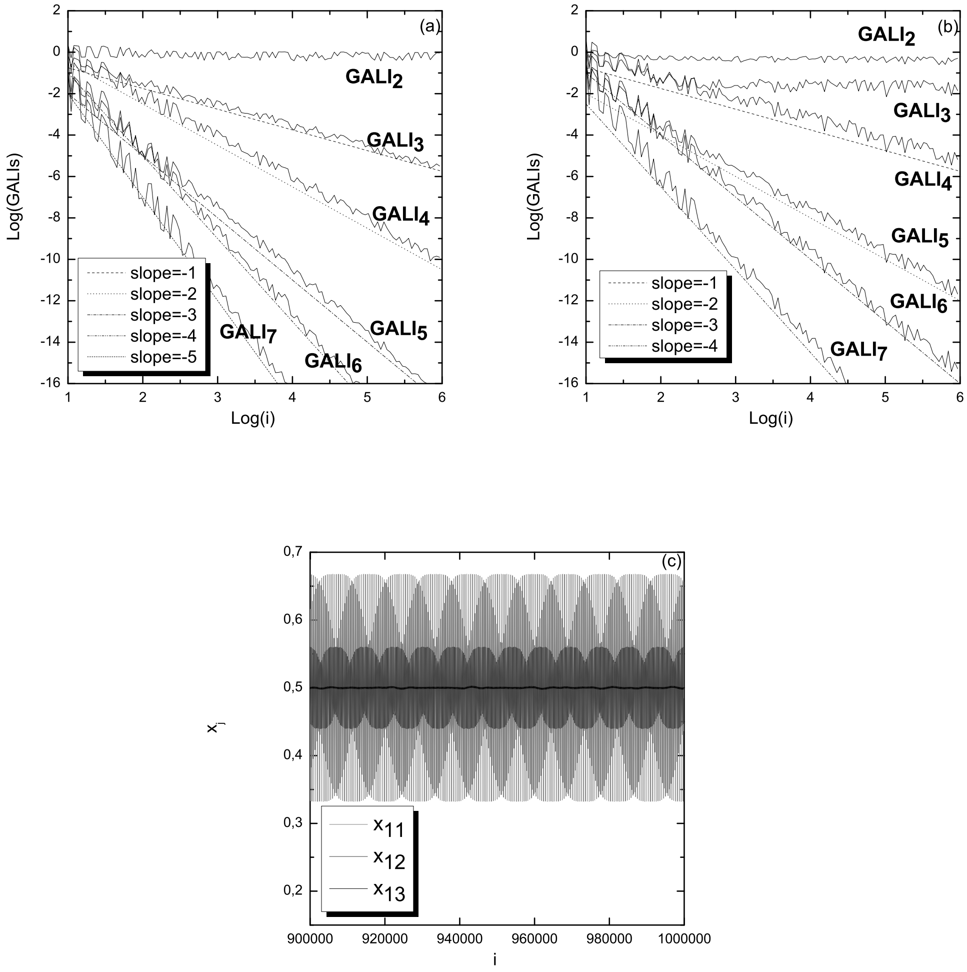

Figure 3.12: (a) GALI$_k$, $k = 2, ..., 7$, for for $N = 20$ – coupled standard maps with $K_j = 2$, $\beta = 0.001$ and initial conditions R1 (see text). GALI$_2$ fluctuates around a non–zero value implying a regular motion that lies on a 2D torus, while the slopes of the algebraically decaying indices are in agreement with (2.90).(b) GALI$_k$ for the initial conditions R2 (see text) imply that the motion lies on a 3D torus, since GALI$_{2,3}$ tend to a non–zero number. This quasiperiodic localized dynamics of R2 is clearly seen in (c), where we plot the x_n oscillations of the 11^{th} (light gray color), 12^{th} (gray color) and 13^{th} (black color) map. From the last 10^5 iterations shown in this figure, it is evident that the main part of the energy is confined only in the “middle” 3 maps and is not shared by any of the other degrees of freedom of the system.

Using now well–known methods of linear algebra, we diagonalize the matrix $\mathcal{A}$ writing $\mathcal{D} = \mathcal{P}^{-1}\mathcal{A}\mathcal{P}$, where $\mathcal{P}$ is an invertible matrix whose columns are the eigenvectors of the matrix $\mathcal{A}$ and $\mathcal{D}$ is diagonal, $\mathcal{D} = diag[\lambda_1, ..., \lambda_{2N}]$, provided the eigenvalues λ_i are real and discrete.

Our case, of course, involves oscillations about a stable equilibrium point and hence the above system has $2N$ discrete complex eigenvalues $\lambda_j = a_j + ib_j$, $\bar{\lambda}_j = a_j - ib_j$ and eigenvectors $w_j = u_j + iv_j$, $\bar{w}_j = u_j - iv_j$, with $j = 1, 2, ..., N$. Thus, $u_1, v_1, ..., u_N, v_N$ form a basis of the space $\mathcal{R}^{2N}$ and the invertible matrix $\mathcal{P} = [v_1, u_1, , ..., v_N, u_N]$ leads us to the Jacobi normal form

$$\mathcal{B} = \mathcal{P}^{-1}\mathcal{A}\mathcal{P} = diag \begin{bmatrix} a_j & -b_j \\ b_j & a_j \end{bmatrix},$$

of a $2N \times 2N$ matric $\mathcal{B}$ with 2×2 blocks along its diagonal. In this way, using the transformation $z = \mathcal{P}^{-1}x$, we can reduce the initial problem to a system of uncoupled equations, whose evolution is described by the equations

$$z' = \mathcal{P}^{-1}\mathcal{A}\mathcal{P}z, \tag{3.19}$$

where $z' = (l^1_{n+1}, k^1_{n+1}, ..., l^N_{n+1}, k^N_{n+1})^T$, $z = (l^1_n, k^1_n, ..., l^N_n, k^N_n)^T$ and z represents the linear normal modes of the map. Thus, in order to excite a continuation of one or more of these modes, we extract the appropriate x–initial condition by the transformation $x = \mathcal{P}z$. The evolution in the uncoupled coordinates is given by the transformation

$$\begin{aligned} l^j_{n+1} &= a_i l^j_n - b_i k^j_n \\ k^j_{n+1} &= b_i l^j_n + a_i k^j_n \end{aligned} \tag{3.20}$$

where each pair of (l^j, k^j) corresponds to a normal mode of the system. Since the map is area–preserving $a_j^2 + b_j^2 = 1$ and we may define the quantity $E^j_n = (l^j_n)^2 + (k^j_n)^2$ as the energy of each mode, which is preserved under the evolution of the linear map, i.e. $E^j_{n+1} = E^j_n$. Thus, to study recurrences, we start with the example of $N = 5$ coupled standard maps, choose a “small” coupling parameter $\beta = 0.00001$ and excite 5 different modes. As a result, we are able to detect a quasiperiodic orbit that lies on a 5D torus, indicated by all the GALI$_k$, $k = 1, ..., 5$, approaching a constant, as shown in Fig. 3.13. This is verified in Fig. 3.13b, where we plot the corresponding energy modes of the coupled system and find that they are nearly invariant, as they would have been in the uncoupled case.

Next, we increase the number of coupled maps from 5 to 20, keeping $\beta = 0.00001$ and choosing different K_j (in triplets of -1.35, -1.45, -1.55), with $j = 1, ..., 20$. Exciting now only *one normal mode* (the 1^{st}), much like the original FPU case, we calculate the GALIs again and find that the orbit is again quasiperiodic, lying on a 6–dimensional torus, as evidenced by the fact that GALI$_k$ for $k = 2, ..., 6$ fluctuate around non–zero values, see Fig. 3.14a. This is, of course, a low–dimensional torus, since generically one expects regular orbits of this system to lie on $N = 20$–dimensional tori! From the calculation of the normal mode energies in this experiment, we observe that the initial energy is now shared by 6 modes and executes recurrences, for as long as we have integrated the equations of motion. The energies of these 6 modes are not shown here since their values are too close to each other to be distinguished in a graphical representation.

Finally, as our last experiment, we increase the coupling parameter to $\beta = 0.01$, for the same choice of initial conditions and K_j values as in Fig. 3.14a. The result is that the influence of the coupling is now quite strong and leads to the breakdown of recurrences and the onset of chaotic behavior. This is clearly depicted in Fig. 3.14b, where the GALI$_k$s of this case exhibit exponential decay, implying the chaotic nature of this orbit.

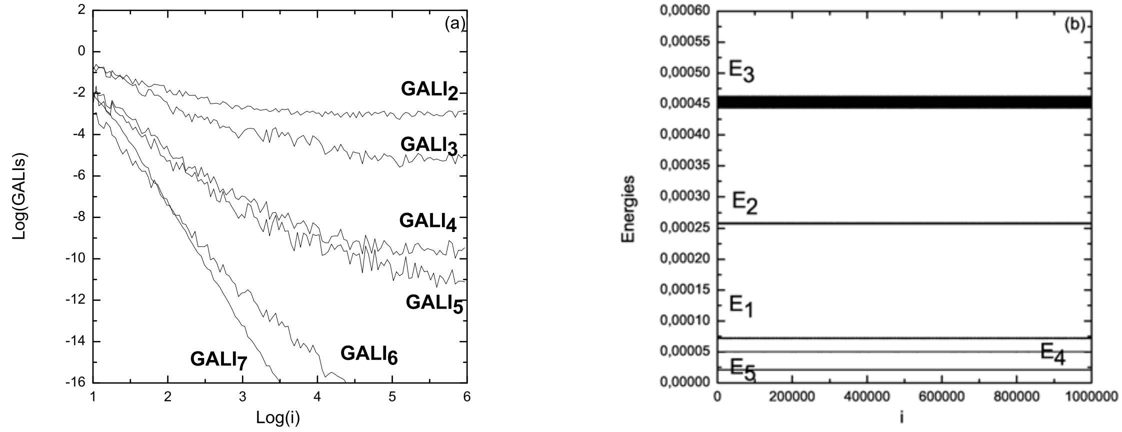

Figure 3.13: (a) GALIs for 5 coupled standard maps with $K_1 = -2.30, K_2 = -2.35, K_3 = -2.40, K_4 = -2.45, K_5 = -2.50)$, $B = 0.00001$ and initial conditions that excite 5 different normal modes. Note that the GALI$_k$ for $k = 2, 3, 4, 5$ fluctuate around a non–zero value implying a regular motion that lies on a 5D torus. (b) The energies for the corresponding normal modes.

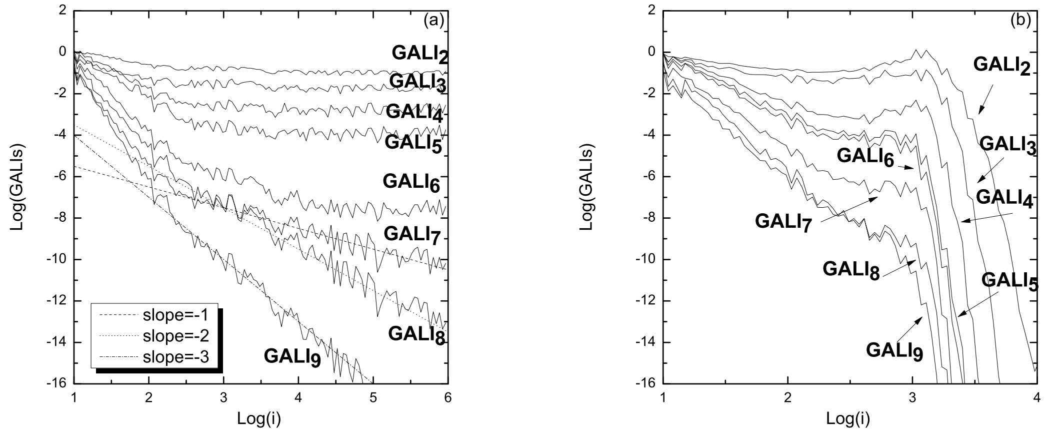

Figure 3.14: (a) Exciting only one mode in a case of 20 coupled standard maps, with $\beta = 0.00001$ and K_j in triplets of $-1.35, -1.45, -1.55$, the GALI$_k$, for $k = 2, ..., 6$ asymptotically become constant, implying that the motion lies on a 6D torus. (b) An orbit with the same initial condition and K_j as in (a) but with a larger coupling parameter, ($\beta = 0.01$), becomes chaotic, as all the GALIs are seen to decay exponentially to zero.

CHAPTER 4

DYNAMICS AND STRUCTURE OF BARRED GALAXIES

4.1 Introduction

Exploring the nature of orbits in galaxies constitutes a very important issue, not only because of the evident astronomical interest in classifying the types of the orbits that exist in such systems, but also because orbits are needed to construct self–consistent models of galaxies. In order to study and understand the structure and dynamics of a galaxy it is necessary to calculate its orbits, periodic, quasi–periodic and chaotic, as well as the percentages of phase space “volume” they occupy.

A significant fraction among the galaxies are barred galaxies. Ferrers’ barred galaxy models have proved very efficient for studying the main properties of real barred galaxies. The detection of periodic orbits and their stability in these models has already been studied in detail by many researchers [95, 113, 112, 92, 94, 93]. It is well–known that stable periodic orbits of low period possess in their neighborhood significant regions of quasi–periodic (or regular) motion. A number of questions, therefore, arises concerning these regions of stability: How far from the stable periodic orbit, can regular motion be sustained? Where are chaotic regions located in phase space and configuration space? What are the model’s parameters that favor larger islands of stability around the main stable periodic orbits? Which kind of chaotic orbits, together with the regular, can emulate realistic bar features and to what extent? How can chaotic orbits be associated with actually observed stars’ orbits and motions that could be observed in real galaxies?

4.2 The Ferrers’ Bar Model

A 3D rotating model of a barred galaxy can be described by the Hamiltonian function

$$H = \frac{1}{2}(p_x^2 + p_y^2 + p_z^2) + V(x, y, z) - \Omega_b(xp_y - yp_x). \tag{4.1}$$

The bar rotates around its z–axis, while the x–direction is along the major axis and the y along the intermediate axis of the galaxy. The p_x, p_y and p_z are the canonically conjugate momenta, V is the potential, Ω_b represents the pattern speed of the bar and H is the total energy of the system

(Jacobi constant). The corresponding equations of motion are

$$\begin{aligned}
\dot{x} &= p_x + \Omega_b y, \\
\dot{y} &= p_y - \Omega_b x, \\
\dot{z} &= p_z, \\
\dot{p_x} &= -\frac{\partial V}{\partial x} + \Omega_b p_y, \\
\dot{p_y} &= -\frac{\partial V}{\partial y} - \Omega_b p_x, \\
\dot{p_z} &= -\frac{\partial V}{\partial z}.
\end{aligned} \tag{4.2}$$

The equations of the evolution of the deviation vectors needed for the calculation of the SALI and GALI indices are given by the corresponding variational equations

$$\begin{aligned}
\dot{\delta x} &= \delta p_x + \Omega \delta y, \\
\dot{\delta y} &= \delta p_y + \Omega \delta x, \\
\dot{\delta z} &= \delta p_z, \\
\dot{\delta p_x} &= -\frac{\partial V}{\partial x \partial x}\delta x - \frac{\partial V}{\partial x \partial y}\delta y - \frac{\partial V}{\partial x \partial z}\delta z + \Omega_b \delta p_y, \\
\dot{\delta p_y} &= -\frac{\partial V}{\partial y \partial x}\delta x - \frac{\partial V}{\partial y \partial y}\delta y - \frac{\partial V}{\partial y \partial z}\delta z - \Omega_b \delta p_x, \\
\dot{\delta p_z} &= -\frac{\partial V}{\partial z \partial x}\delta x - \frac{\partial V}{\partial z \partial y}\delta y - \frac{\partial V}{\partial z \partial z}\delta z.
\end{aligned} \tag{4.3}$$

The potential V of our model consists of three components

1. A *disc*, represented by a Miyamoto disc

   $$V_D = -\frac{GM_D}{\sqrt{x^2 + y^2 + (A + \sqrt{z^2 + B^2})^2}}, \tag{4.4}$$

   where M_D is the total mass of the disc, A and B are the horizontal and vertical scalelengths, and G is the gravitational constant.

2. A *bulge*, which is modeled by a Plummer sphere whose potential is

   $$V_S = -\frac{GM_S}{\sqrt{x^2 + y^2 + z^2 + \epsilon_s^2}}, \tag{4.5}$$

   where ϵ_s is the scalelength of the bulge and M_S is its total mass.

3. A triaxial Ferrers *bar*, the density $\rho(x)$ of which is

   $$\rho(x) = \begin{cases} \rho_c (1 - m^2)^2 & , m < 1 \\ 0 & , m \geq 1 \end{cases}, \tag{4.6}$$

   where $\rho_c = \frac{105}{32\pi} \frac{GM_B}{abc}$ is the central density, M_B is the total mass of the bar and

   $$m^2 = \frac{x^2}{a^2} + \frac{y^2}{b^2} + \frac{z^2}{c^2}, \qquad a > b > c > 0, \tag{4.7}$$

with a, b and c being the semi-axes. The corresponding potential is

$$V_B = -\pi Gabc\frac{\rho_c}{n+1}\int_\lambda^\infty \frac{du}{\Delta(u)}(1-m^2(u))^{n+1}, \tag{4.8}$$

where

$$m^2(u) = \frac{x^2}{a^2+u} + \frac{y^2}{b^2+u} + \frac{z^2}{c^2+u}, \tag{4.9}$$

$$\Delta^2(u) = (a^2+u)(b^2+u)(c^2+u), \tag{4.10}$$

n is a positive integer (with n=2 for our model) and λ is the unique positive solution of

$$m^2(\lambda) = 1, \tag{4.11}$$

outside of the bar ($m \geq$1), and λ=0 inside the bar. The corresponding forces are given analytically in [95].

This model has been used extensively for orbital studies by [113, 112, 92, 94, 93]. Our so–called $MAIN$ model has the following values of parameters G=1, Ω_b=0.054 (54$Km \cdot sec^{-1} \cdot Kpc^{-1}$), a=6, b =1.5, c=0.6, A=3, B=1, ϵ_s=0.4, M_B=0.1, M_S=0.08, M_D=0.82 both for its 2D and 3D versions. The units used, are: 1 kpc (length), 1 Myr (time), $2 \times 10^{11} M_\odot$ solar masses (mass) and the total mass $G(M_S + M_D + M_B)$ is set equal to 1.

The maximal time of integration of the orbits through the equations of motion and the variational equations is set to be T=10,000Myr (or 10 billion yrs), that corresponds to a time less than that of one Hubble time $\approx (13.7 \pm 0.2)$ billion yrs.

4.2.1 The 2 degree of freedom Ferrers model

The 2 DOF Ferrers model is described by the Hamiltonian equation (4.1) setting $(z, p_z) = (0, 0)$, i.e.

$$H = \frac{1}{2}(p_x^2 + p_y^2) + V(x, y) - \Omega_b(xp_y - yp_x). \tag{4.12}$$

The application of the SALI method to the 2 DOF barred potential can describe pictorially the basic properties of the model and help us better understand the generalized 3 DOF model. In Fig. 4.1, we present the example of two orbits of the $MAIN$ model, one regular in panel a), with initial condition:

$$(x, y, p_x, p_y) = (-0.625, -0.06, p_x(H), 0) \quad \text{(orbit R)}$$

and one chaotic in panel b), with initial condition:

$$(x, y, p_x, p_y) = (-0.625, -0.24, p_x(H), 0) \quad \text{(orbit C)},$$

for the Hamiltonian value $H = -0.360$. Their qualitatively different behavior is also shown in Fig. 4.2a), where we have projected their intersections with the Poincaré surface of section in the (y, p_y)–plane. The chaotic orbit C (gray points) tends to fill with scattered points all its available part of the (y, p_y)–plane, while the ordered orbit R (black points) creates a set of points that form a closed invariant curve, on the left part of the picture.

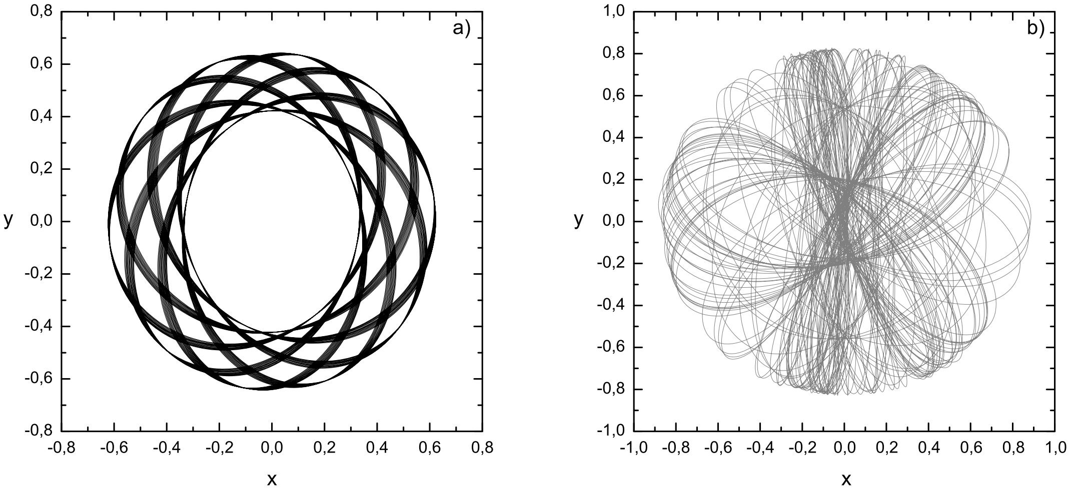

Figure 4.1: Projections of the regular orbit R (panel a)) and of the chaotic one C (panel b)) in the (x, y)–plane.

In Fig. 4.2b), we apply the SALI method to these two orbits and present two characteristic aspects of their different behaviors: For the chaotic orbit C, the SALI tends to zero ($\simeq 10^{-16}$) exponentially after some transient time, while for the regular orbit R, it fluctuates around a positive number. The corresponding maximal LCE, σ_1, for these orbits is shown in Fig. 4.2c), where the $\log(\sigma_1)$ for the regular orbit tends to zero, while for the chaotic orbit it tends to a positive number after a long integration time. Mind that in Fig. 4.2 the Log(SALI) in y–axis of panel b) ranges from -16 to 2, while the $\mathrm{Log}(\sigma_1)$ in panel c) ranges from -7 to 0. The advantage of our method is the ability to detect the chaotic character of the orbit fast, since the SALI reaches the zero–value after a relatively short time, $t \simeq 10^3$. The corresponding maximal LCE σ_1, in both cases and at the same time ($t \simeq 10^3$), has not yet converged and thus one can not safely infer from its value the true nature of the orbit.

By choosing orbits with initial conditions on the line $p_y = 0$ (Fig. 4.3) of the PSS and calculating their SALI values, we were able to detect very small regions of stability that can not be visualized easily on the PSS. Then, taking initial conditions on the whole (y, p_y)–plane (with x=0) and calculating the values of the SALI, we can detect very small regions of stability (or instability) more globally. We are able to construct a map of the chaotic and regular regions similar to the PSS, but with more accuracy and higher resolution. We have chosen many different values of the energy and used a sample of 50,000 initial conditions on the same (y, p_y)–plane of the corresponding PSS. In Fig. 4.4,4.5, on the left column we have plotted the PSS for the Hamiltonian values H= –0.360, –0.335(in Fig. 4.4), –0.300, –0.260 (in Fig. 4.5) and on the right column the corresponding final values of the SALI for the chosen grid of initial conditions. In the right columns of these two plots, the light grey color corresponds to regular orbits, the black color represents the chaotic orbits/regions, while the intermediate colors between the two represent the so–called sticky orbits, i.e. orbits that "stick" onto quasiperiodic tori for long times but their nature is eventually revealed to be chaotic.

Repeating this procedure for many values of the energy, we are able to follow the change of the

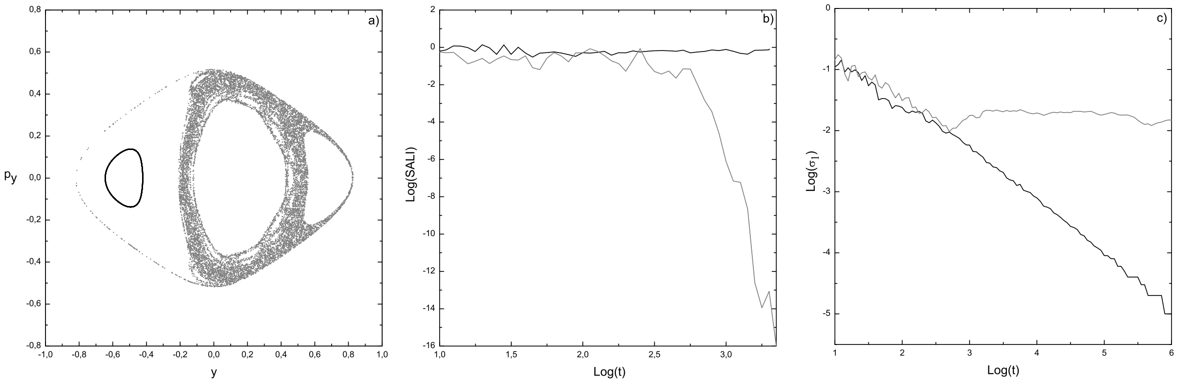

Figure 4.2: a) Poincaré surface of section for the two orbits R (black color) and C (grey color) in the (y, p_y)-plane. The points of the successive intersections of the regular orbit R with plane create a closed curve, while the points of the chaotic orbit C fill with scattered points all its available part of motion. b) The corresponding evolution of SALI for the same orbits. The chaotic orbit C (gray line) decays exponentially and fast to zero while the ordered orbit R (black line) fluctuates round a non-zero number. c) The corresponding evolution of the maximal Lyapunov exponents σ_1 for the same orbits. The chaotic orbit C (gray line) after some iterations tends to a non-zero value and the regular orbit R (black color) reduces linearly and slowly to zero. Mind that the Log(SALI) in y–axis of panel b) ranges from -16 to 2, while the Log(σ_1) in panel c) ranges from -7 to 0.

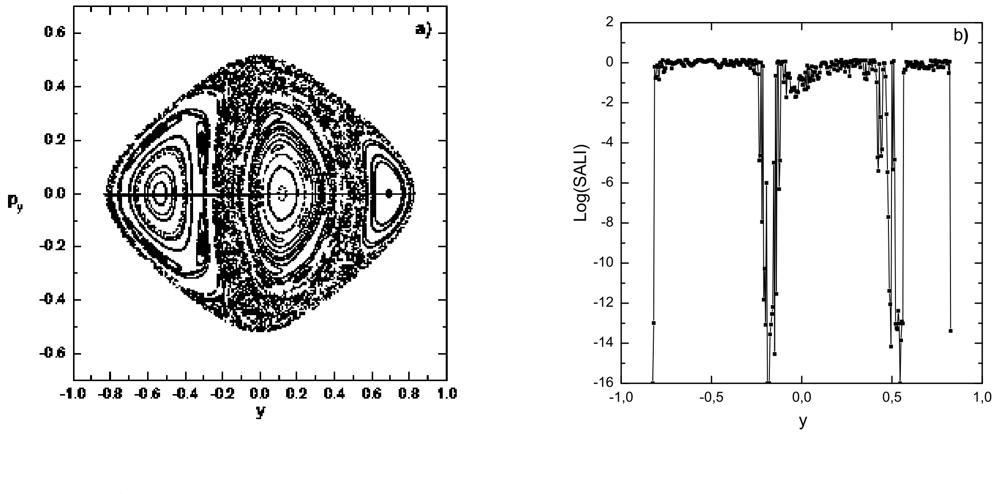

Figure 4.3: a) Poincaré surface of section for the $2D$ Ferrers' model in (y, p_y) plane for $H = -0.360$, b) The variation of the SALI value for initial conditions chosen on the line $p_y = 0$ of the corresponding PSS of panel a).

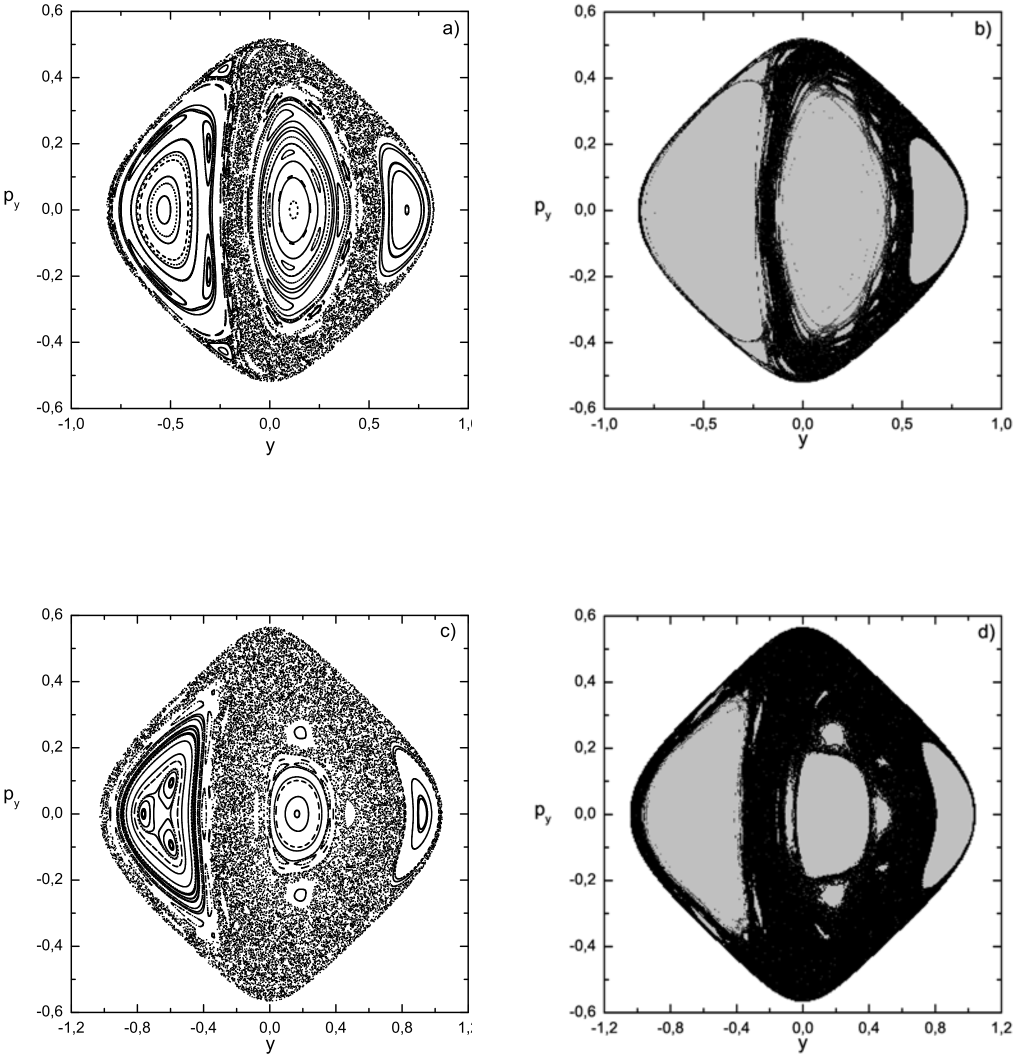

Figure 4.4: Agreement between the results of the Poincaré surface of section (PSS) and SALI. The Poincaré surface of section for the 2D Ferrers model with $H = -0.360$ (panel a)) and $H = -0.335$ (panel c)). Regions of different values of the SALI for 50,000 initial conditions on the (y, p_y)–plane the same values of the Hamiltonian (panels b),d) respectively).The light grey colored areas correspond to regular orbits, while the dark black ones to chaotic. Few gray and dark gray colored points correspond to “sticky” orbits. Note the excellent agreement between the two methods as far as the gross features are concerned, as well as the fact the SALI can easily pick out small regions of stability which the PSS has difficulties detecting.

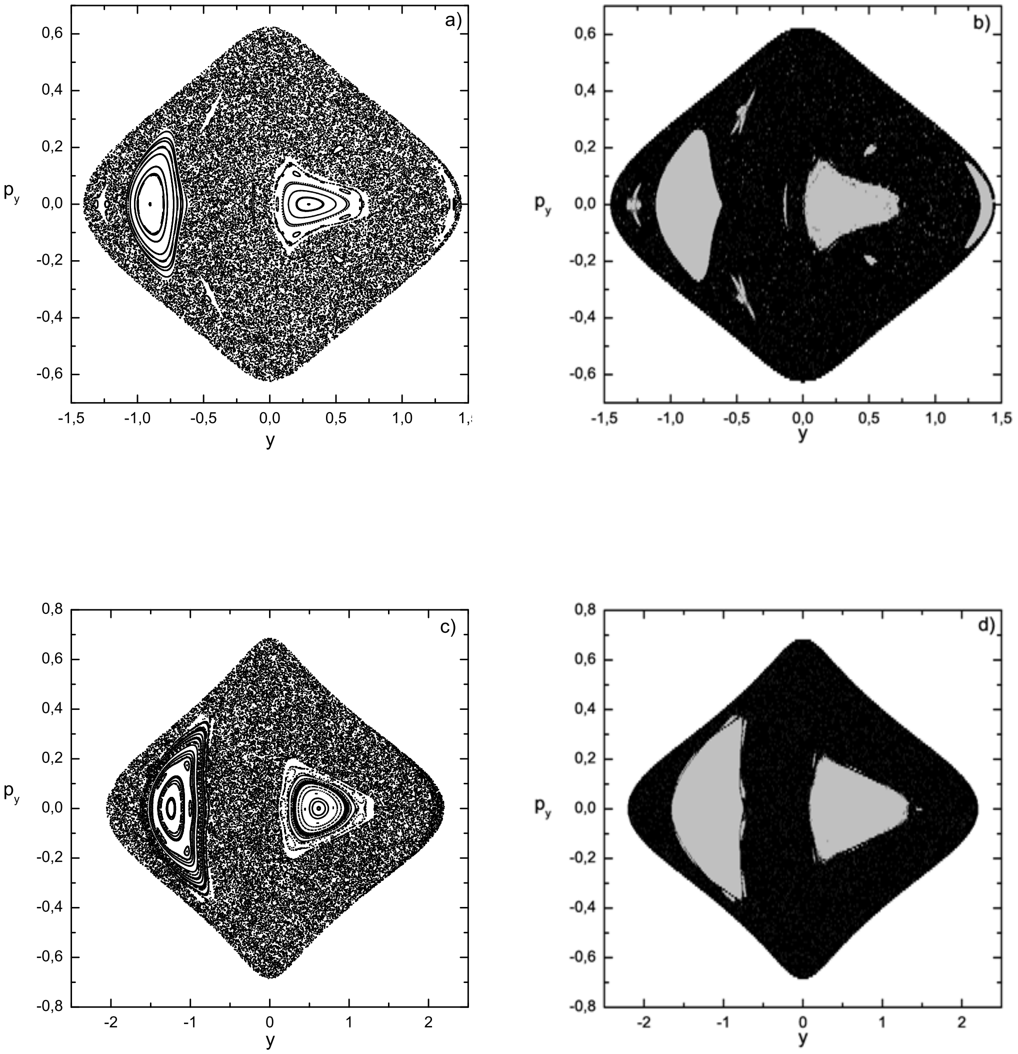

Figure 4.5: Similarly as in Fig. 4.4, the panels in the left column correspond to the Poincaré surface of section for the 2D Ferrers model with $H = -0.300$ (panel a)) and $H = -0.260$ (panel c)). The panels in the right column show again the final value of the SALI for the chosen initial conditions on the (y, p_y)–plane again respectively.

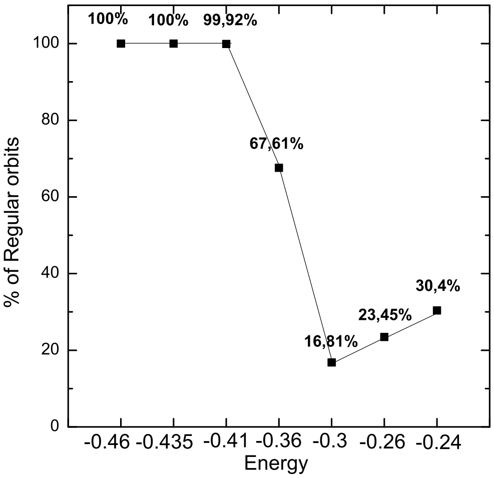

Figure 4.6: Percentages of regular orbits for several values of the energy in 2 dof.

fraction of chaotic and ordered orbits in the phase space as the energy of the model varies. The chosen values of the Hamiltonian functions cover the range of the available energy interval up to the value of the escape energy, ensuring that there are not any escapes for the orbits. Using the SALI method we followed the variation of the presence of chaotic orbits in the phase space as the value of the total energy increases. Although, generally the percentages of the chaotic orbits increases as the energy increases, this behavior diversifies in big energy values. As we can see in the example of $H = -0.300$ and $H = -0.260$. Despite the fact that for $H = -0.260$ lots of stability islands have been vanished, the main big island on the left has been enlarged relatively. The variation of the percentages is presented in Fig. 4.6, where we have chosen seven values for the energy and we present the percentages of the regular orbits. We used the threshold SALI$> 10^{-8}$, in order to characterize an orbit as regular for the measuring of the percentages. We also tried to use a final time for the integration of the orbits that it could offer to us a reliability in the distinction between their regular and chaotic character, i.e. most of the sticky orbits would have the appropriate time to signify their chaotic nature, and at the same time a realistic as possible physically final time of iteration. Following this concept, we chose the maximal time of integration of the orbits to be the T$= 10,000Myr$ (or 10 billion yrs), that corresponds to a time less than one Hubble time $\approx (13.7 \pm 0.2)$ billion yrs. However, the evaluation of the SALI can be significantly faster when an orbit is chaotic (SALI is tends to zero exponentially), since then we can terminate the calculation earlier.

4.2.2 The 3 DOF Ferrers model

We now turn to the 3 DOF model and begin a study of ordered and chaotic domains, which will be completed in paper II of this series. Let us choose, for example, a regular orbit and compare the efficiency of our methods with the maximal LCE's. In Fig. 4.7a),b) we show the behavior of a regular orbit R1, with initial condition:

$$(x, y, z, p_x, p_y, p_z) = (0.58750, 0.0, 0.29770, 0.0, 0.33750, 0.0)$$

at $t = 0$ and of a chaotic orbit C1, with initial condition:

$$(x, y, z, p_x, p_y, p_z) = (0.58750, 0.0, 0.33333, 0.0, 0.20000, 0.0).$$

In this example, the SALI has become almost zero for $t \simeq 10^4$. However, as it is clear in Fig. 4.7b), the higher order GALI_k, $k = 5, 6$, indicate the chaoticity of the orbit already by $t \simeq 10^3$, which is just about the time when the maximal LCE stops decreasing (see 4.7a)).

In Fig. 4.8a), we show the behavior of the log(GALI) indices and their slopes for the regular orbit R1. Note that only GALI_2 remains constant while the $\text{GALI}_{3,4,5,6}$ tend to zero following power laws predicted by equations (2.90)

$$\begin{aligned} &\text{GALI}_2(t) \propto const., \quad \text{GALI}_3(t) \propto \frac{1}{t}, \quad \text{GALI}_4(t) \propto \frac{1}{t^2}, \\ &\text{GALI}_5(t) \propto \frac{1}{t^4}, \qquad \text{GALI}_6(t) \propto \frac{1}{t^6}, \end{aligned} \tag{4.13}$$

for $l = 2$. This means that the orbit's motion lies on a 2D torus even though in 3 DOF Hamiltonian systems one expects the dimension of the torus to be 3. One such example of a 3D torus is provided by the regular orbit R2, with initial condition:

$(x, y, z, p_x, p_y, p_z) = (0.97917, 0, 0.04167, 0, -0.17778, 0)$.

In Fig. 4.8b, we show its GALI indices, where both $\text{GALI}_{2,3} \propto$ constant and the $\text{GALI}_{4,5,6}$ decay linearly following the laws :

$$\text{GALI}_4(t) \propto \frac{1}{t^2},\ \text{GALI}_5(t) \propto \frac{1}{t^4},\ \text{GALI}_6(t) \propto \frac{1}{t^6}, \tag{4.14}$$

for $l = 3$. In order to understand in more detail the above results we calculated the main frequencies of the regular orbits R1 and R2. We found that R2 has significant amplitudes at 3 main frequencies while R1 only at two, as shown in Fig. 4.9f),c) respectively. This difference is also clearly reflected in their (x, y) and (x, z) projections, where the "complexity" of R2 (quasiperiodic motion on a 3D torus) is more pronounced than the one of the orbit R2 (quasiperiodic motion on a 2D torus). Thus, in such cases GALI_3 offers an extra advantage in helping us detect different "degrees" of regularity and does not serve only to distinguish between chaotic and regular motion.

4.3 The distribution of Orbits in Phase Space

For our calculations we used three different classes (Cases) of initial conditions:

- Case *A*:

  50,000 orbits equally spaced in the plane (x, z, p_y) with $(y, p_x, p_z) = (0, 0, 0)$, with $x \in [0.0, 7.0]$, $z \in [0.0, 1.5]$ and $p_y \in [0.0, 0.45]$.

- Case *B*:

  50,000 orbits equally spaced in the plane (x, p_y, p_z) with $(y, z, p_x) = (0, 0, 0)$, with $x \in [0.0, 7.0]$, $p_y \in [0.0, 0.35]$ and $p_z \in [0.0, 0.35]$.

The x is always the bar's major axis. By these two ways, we try to create initial conditions compatible with bar's features. In this way, we attempted to create initial conditions that could support the bar and be mainly trapped by the x_1 tree, i.e. the x_1 family and the x_1v_i, $i = 1, ...$

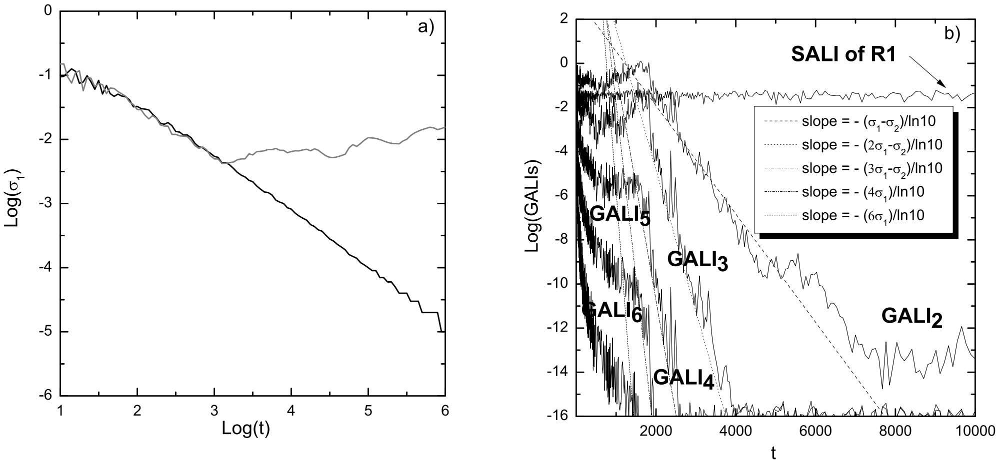

Figure 4.7: a) Behavior of the maximal Lyapunov Exponents, σ_1, of the regular orbit R1 (black line) and the chaotic one C1 (gray line) in the 3 DOF case. b) The corresponding SALI evolution of the R1 and the slopes of the GALIs of the chaotic orbit C1. The maximal positive LCEs of the orbit C1 are $\sigma_1 \approx 0.00910$ and $\sigma_2 \approx 0.00345$. Comparing with a) we see that $\mathrm{GALI}_k, k = 5, 6$ already predict the chaotic nature of the orbit at t $\simeq$ 2000, where the maximal LCE, σ_1, has not yet shown such an indication.

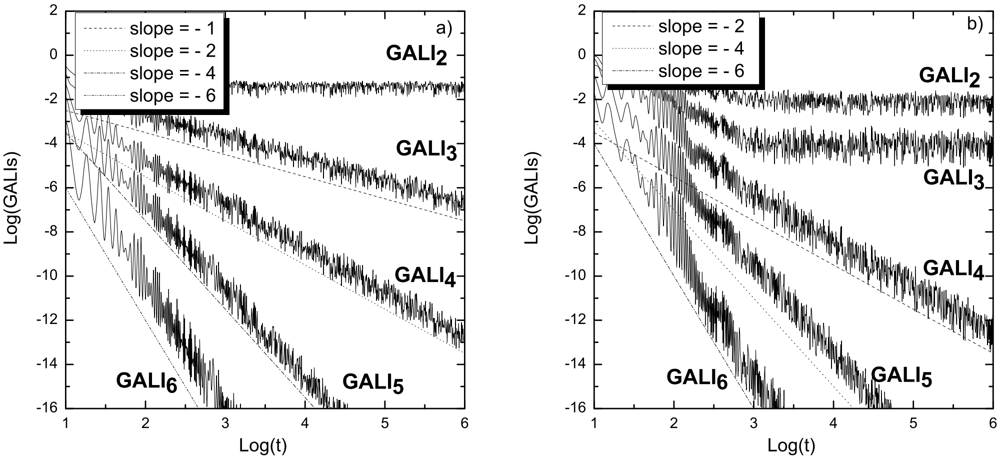

Figure 4.8: a) Slopes of GALIs for the regular orbit R1 lying on a 2D torus with only $\mathrm{GALI}_2 \propto$ constant while the $\mathrm{GALI}_{3,4,5,6}$ decay following a power law. b) Slopes of GALIs for the regular orbit R2 showing that its motion lies on a 3D torus, where $\mathrm{GALI}_{2,3} \propto$ constant.

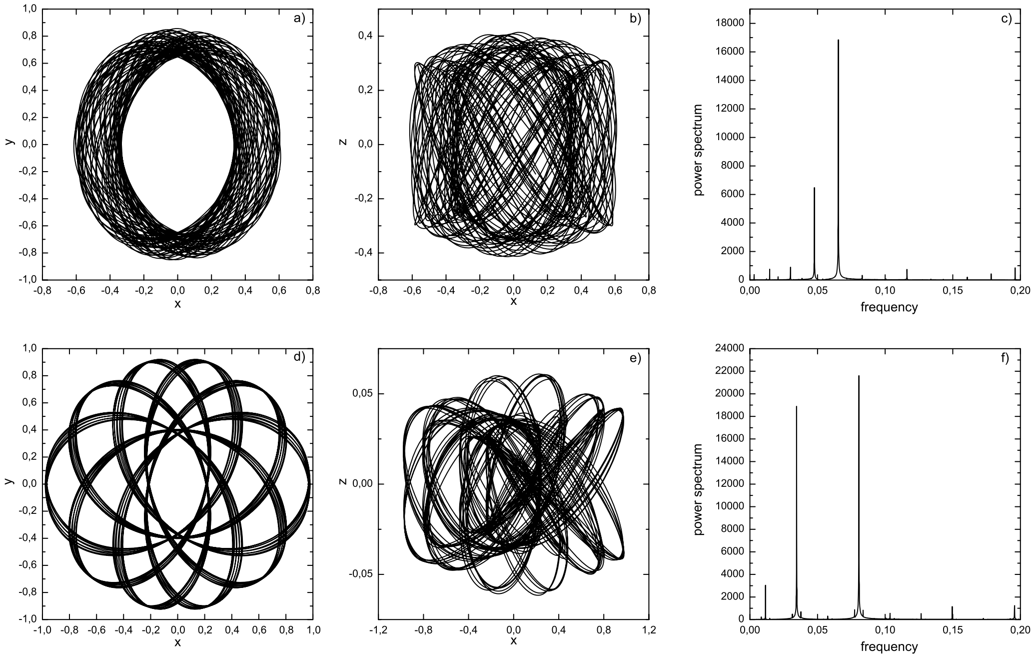

Figure 4.9: Two projections (1st and 2nd columns) of the quasiperiodic orbits R1 (1st row) and R2 (2nd row) and their corresponding frequencies (panels c and f). The R2 has 3 main frequencies and this property is evident in the morphology of its motion in panel d (or e), compared to R1's motion in panel a (or b).

families that bifurcate from it and extend vertically well above the disc region [92]. Although these initial conditions cover all the available energy interval, they are not spread uniformly over it. Note also that a few of these have an energy value beyond the escape energy, and we dismiss them. These, however, constitute less than 0.5% of the total, so that they influence very little our study and the statistics.

- Case C:

  Initial conditions in the configuration space that follow the density profile of the model which is related to studied potential of the system. By this way, we try to accomplish a more realistic representation of a real galaxy. In order to achieve the appropriate density of points we choose a random value of the Hamiltonian H (total energy) to be up to +10% of the escape energy defined by the zero velocity curve. We set initially $(p_y, p_z) = (0, 0)$ and we define the maximum value of the density for the corresponding potential. Then, we give randomly initial conditions for the spatial coordinates (x, y, z) in a grid defined by the axial–lengths of the bar, i.e. $-a \leq x \leq a$, $-b \leq z \leq b$, $-c \leq z \leq c$, where a, b, c are the lengths of the major, intermediate and short axis of the bar and with the use of the *rejection method* [98] we obtain the orbits in the picked (eligible) density. Having all these, in the end we calculate the p_x–momenta by the relation: $p_x = H(x, y, z, p_y, p_z)$.

For all three classes initial conditions we applied three variations to the $MAIN$ initial model (reference model), which we have named as $A - MAIN$, $B - MAIN$ and $C - MAIN$ model respectively. The first variation is a model that it has the short z–axis (c–parameter) of the bar twofold than the $MAIN$ model (models $A - 2C$, $B - 2C$ and $C - 2C$). Another one is a model which intermediate y–axis (b–parameter) of the bar is two times of the initial $MAIN$ model (models $A - 2B$, $B - 2B$ and $C - 2B$). Finally, a model was used in which the value of the mass of the bar (M_B–parameter) is two times greater than in the original $MAIN$ version (models $A - 2MB$, $B - 2MB$ and $C - 2MB$). The full details of all the version of our models can be found in Table 4.1.

The detailed information about the percentages of regular, sticky and chaotic orbits of these models can be found in Fig. 4.11. In order to check that the final number of the initial conditions (50,000) that we use is high enough for obtaining reliable information about the percentages of ordered and chaotic orbits, we used the *bootstrap*–method [98] on several samples, and confirmed their representativeness. In Fig. 4.10, we present synoptically the amount of regular motion among the above different models ($MAIN$, $2C$, $2B$ and $2MB$) for all the three packages of initial conditions (Cases A, B and C). From a first look and before turning to a more detailed discussion of these results, the percentages don't seem to coincide with each other and in some times the trends in regularity are different although parameters variation in the $MAIN$ model is the same. This is due to the different sample of our initial conditions. Cases A, B and C create initial conditions that they populate the phase space in a different manner, i.e. some packages can give initial conditions that populate "better" the region of one stable (or unstable periodic) orbit than another.

4.3.1 Percentages of regular orbits

For the above classes of initial conditions we compute the distribution of regular and chaotic orbits and we find that they attain the following percentages:

Percentages of Case A:

Table 4.1: Parameters for all sets of initial conditions (Cases A, B and C).

Case	model	dof	M_D	M_S	M_B	A	B	ϵ_s	Ω_b	a	b	c
A,B,C	MAIN	3	0.82	0.08	0.1	3	1	0.4	0.054	6	1.5	0.6
A,B,C	2C	3	0.82	0.08	0.1	3	1	0.4	0.054	6	1.5	1.2
A,B,C	2B	3	0.82	0.08	0.1	3	1	0.4	0.054	6	3	0.6
A,B,C	2MB	3	0.72	0.08	0.2	3	1	0.4	0.054	6	1.5	0.6

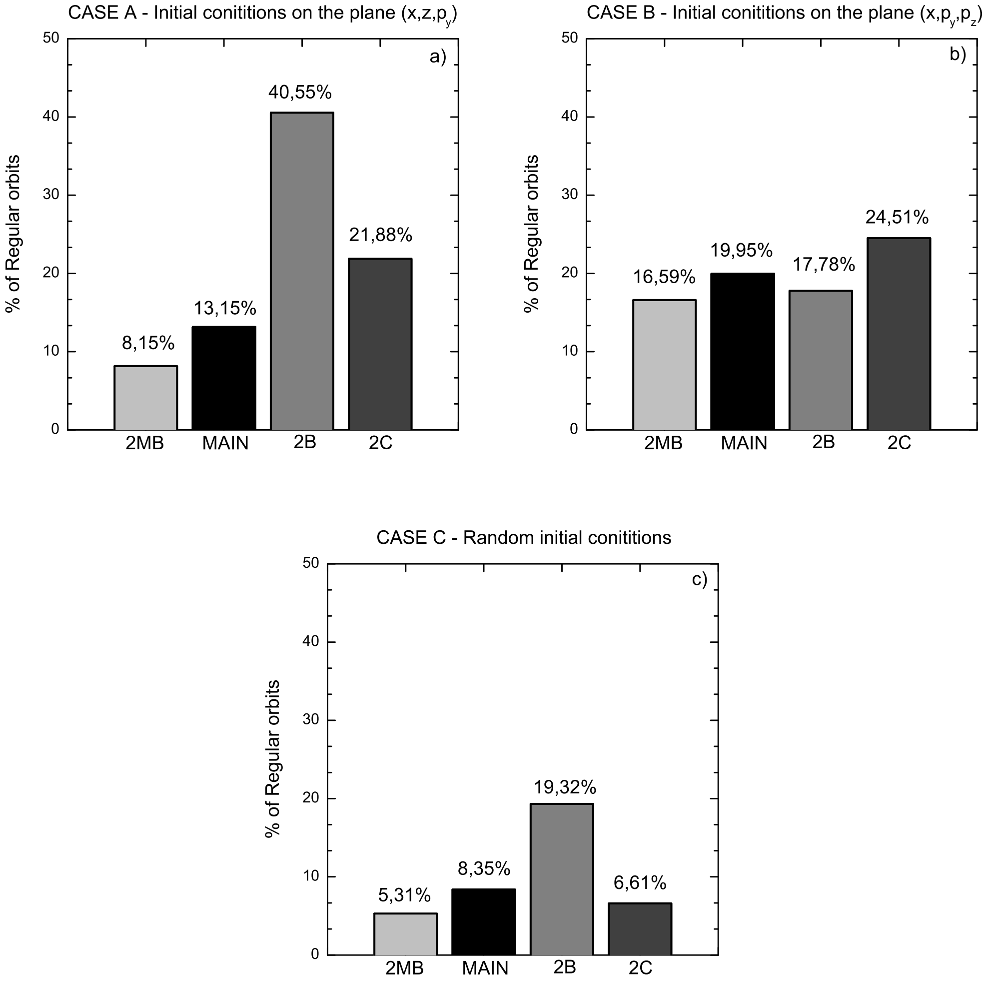

Figure 4.10: Percentages of regular orbits (SALI$\geq 10^{-4}$) for the A, B and C packages of initial conditions (Cases A, B and C) for all the different versions of them (models $MAIN$, $2B$, $2C$, $2GMB$).

In Fig. 4.10a), we present the percentages of the regular orbits for the various packages of initial conditions of the Case A. The distinguishing between them has been done with the threshold SALI$< 10^{-8}$ for the chaotic and SALI$\geq 10^{-4}$ for the regular, while orbits with $10^{8} <$SALI$< 10^{-4}$ are generally considered to be "sticky" orbits. In Fig. 4.11(first column), we present thoroughly the percentages of regular (1st bar), intermediate–sticky (2nd bar) and chaotic (3rd bar) trajectories. Comparing the percentages, we see that the increase of the bar mass (model $2MB$) causes more chaotic behavior. This also confirms the results by [9] in 2 degrees of freedom. On the other hand, when the bar is thicker (model $2C$), i.e. the length of the z–axis larger, the system gets more regular. Finally, we present the corresponding results for a version with larger y–axis (model $2B$) of the basic $MAIN$–model. It turns out again that the increment of the intermediate axis of the bar provides to the system more ordered orbits but not of the same magnitude as the $2C$–model.

Percentages of Case B:

Similarly, in Fig. 4.10b), we present again the percentages of the regular orbits but for the several packages of initial conditions of the Case B now. Using always the same chaos threshold, in Fig. 4.11(second column), we present the detailed percentages in the same way as in Case A. Again the increase of the bar mass (model $2GMB$) causes more chaotic behavior. On the other hand, when the bar is thicker (model $2C$), the system gets again more regular. Finally, we present the corresponding results for a version with larger y–axis (model $2B$) of the basic $MAIN$–model. The different package of initial conditions affects differently in this case. The percentages for model $2B$ are similar with the $MAIN$ model's. The $MAIN$ model contains 19.95% of regular orbits while the $2B$ model 17.78%. We should point out here that besides the difference in the initial conditions between Cases A and B in the coordinates z and p_z, there is also a slight difference in the maximum value of the momenta p_y (up to 0.35 now instead of 0.45 before in Case A).

Percentages of Case C:

As previously, in Fig. 4.10c), we present again the percentages of the regular orbits but for the several packages of initial conditions of the Case C now (look Fig. 4.11(third column) for the further details). Again the increase of the bar mass ($2GMB$ model) causes more chaotic behavior. As the $2B$ model of Case A, a thicker bar in the y direction turns the system more regular. For the version with larger z–axis (model $2C$) of the basic $MAIN$–model there is a small decrease in the percentages of regular orbits (6.61% now from 8.35%. It turns out that this particular way of giving initial conditions doesn't reveal the same trend as the previous.

A first result is that one should consider well what initial conditions want to give and how this shell "covers" well enough the actual phase system of the system. For instance, we initially considered Cases A and B in such way that these initial conditions could mainly well parent the main periodic orbit x_1 (orbits responsible for the barred portrait of the galaxy model) and not very well the retrograde and generally stable family of x_4 periodic orbit [113]. Trying to include a more "global" package of initial condition of the form of Case A that could explore better the system's phase space we tried the following:

- Case A':

  50,000 orbits equally spaced in the plane (x, z, p_y) with $(y, p_x, p_z) = (0, 0, 0)$, with $x \in [0.0, 7.0]$, $z \in [0.0, 1.5]$ and $p_y \in [-0.8, 0.8]$. The present range for the momentums p_y is

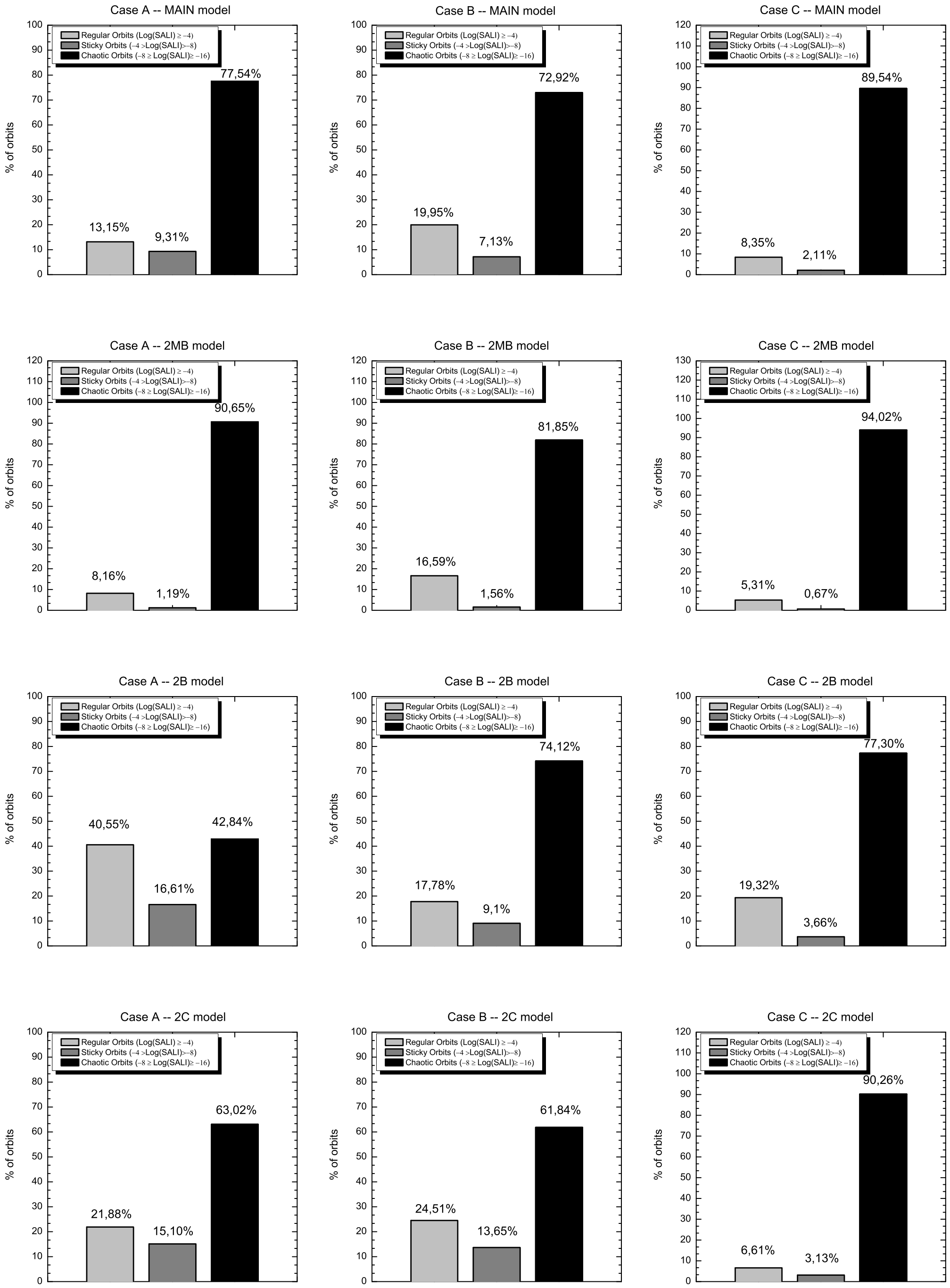

Figure 4.11: Percentages for the Cases A ,B and C for the $MAIN$ (1st row), the $2MB$ (2nd row), $2B$ (3rd row) and $2C$ (4rth row) model. The boxes 1 and 2 contain regular orbits, while boxes 3 and 4 contain chaotic. Box 1 contains strongly regular, box 4 contains strongly chaotic, in boxes 2 and 3 we put the sticky orbits.

Table 4.2: Models with different Ω_b - model parameters values.

model	dof	M_D	M_S	M_B	A	B	ϵ_s	Ω_b	r_L	a	b	c
Ω_1	3	0.82	0.08	0.1	3	1	0.4	0.0367032	1.4a	6	1.5	0.6
Ω_2	3	0.82	0.08	0.1	3	1	0.4	0.0403014	1.3a	6	1.5	0.6
Ω_2	3	0.82	0.08	0.1	3	1	0.4	0.0444365	1.2a	6	1.5	0.6
Ω_4	3	0.82	0.08	0.1	3	1	0.4	0.0493654	1.1a	6	1.5	0.6
Ω_5	3	0.82	0.08	0.1	3	1	0.4	0.0554349	1.0a	6	1.5	0.6

related with the maximum value that is allowed for this to reach associated the zero velocity curve of the system. The amounts of regular orbits are following same trends as in Case A but having small differences in the percentage numbers. The $MAIN$–model has 25.76% regular orbits, the $2MB$–model 16.70%, the $2B$–model 43.54% and the $2C$–model 32.18%.

From our study (details for this are given in next paragraphs), it occurs that, the majority of the regular orbits lie close to (x, y)–plane with small z. The z–direction, for all out outputs, seems to be unstable and very chaotic. Thus, by increasing the c–parameter we increase the number of initial conditions that they are far from the (x, y)-plane, since $-c \leq z \leq c$, in other words the number of chaotic orbits.

4.3.2 Percentages of regular orbits vs. energy

In order to check the variation of the percentages of regular and chaotic orbits as the energy of the model varies, we did the following: We first sorted the energy values for all the initial conditions. Then, we created 30 energy intervals containing equal number of orbits, since our way of giving initial conditions does not imply their uniform distribution in the total energy interval. In every energy interval we calculated the percentages of regular and chaotic orbits, considering as chaotic all the orbits with SALI$< 10^{-8}$. In Fig. 4.12a) we show the percentage of regular orbits in each energy interval, as a function of the mean energy in that interval. Generally, the percentage of regular orbits decreases as the energy increases, but before and after the escape energy (where the Jacobi constant value is $H \simeq -0.20$) there are two peaks. This non–monotonic behavior is related to the appearance or disappearance of stable periodic orbits in the phase space and the size variation of the stability regions around them.

We can compare the results for the percentages of the 3DOF $MAIN$ model with the percentages of 2DOF (since the rest of the parameters are exactly the same) up to the value of the escape energy where we have data for both. There is a similar behavior, the percentages decrease as the energy increases but near the value of the escape energy there is a pick again in both. Of course the way of giving initial conditions in 3DOF offers to us energy values often larger than the escape energy value.

4.3.3 Percentages of regular orbits vs pattern speeds

Furthermore, choosing one class of initial conditions (Case A), we work with different models for several values of the bar's pattern speed Ω_b, see Table 4.2, where we always keep the rest of the model parameters constant. In this versions we try to explore the effect of the value of the pattern speed in the global ordered or chaotic behavior of the system. The corresponding percentages are

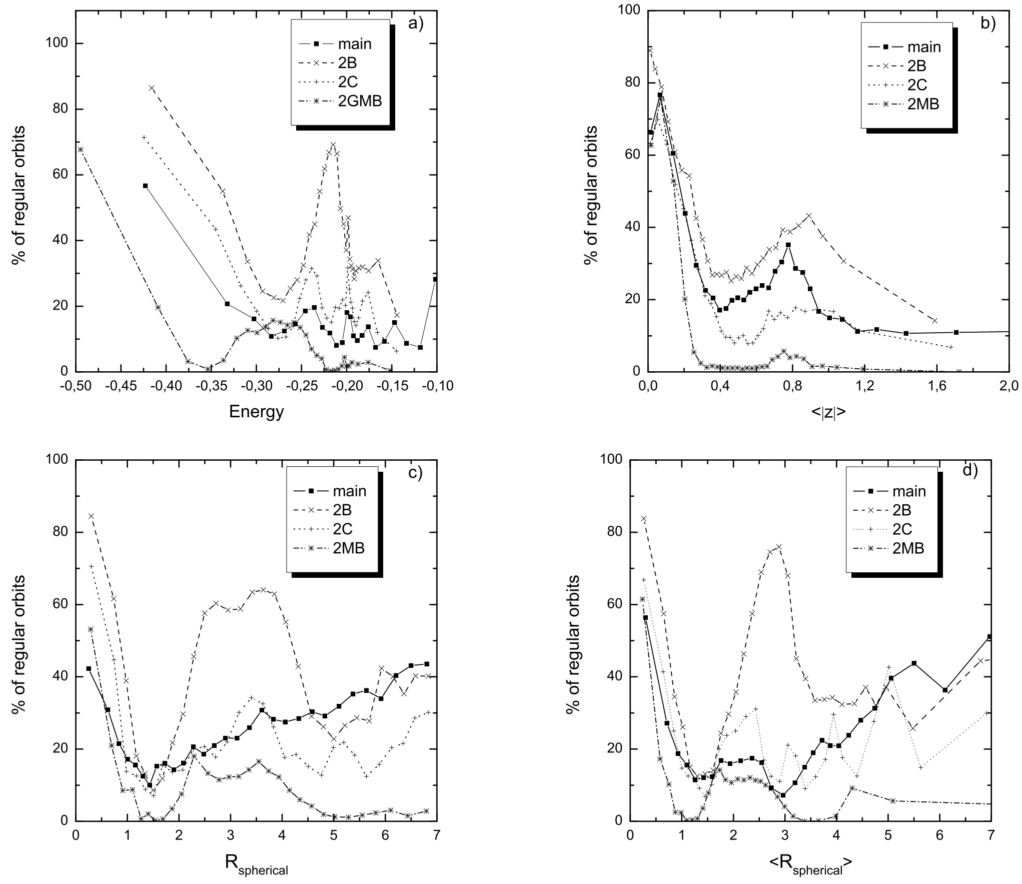

Figure 4.12: Percentages of the regular orbits as the energy (first row/panel), the initial coordinate in the z-axis and their initial spherical radius R_{sph} (middle row), the $< |z| >$ and $< R_{sph} >$ (third bottom) of the orbit's evolution vary for the four versions of the set of initial conditions - Case A.

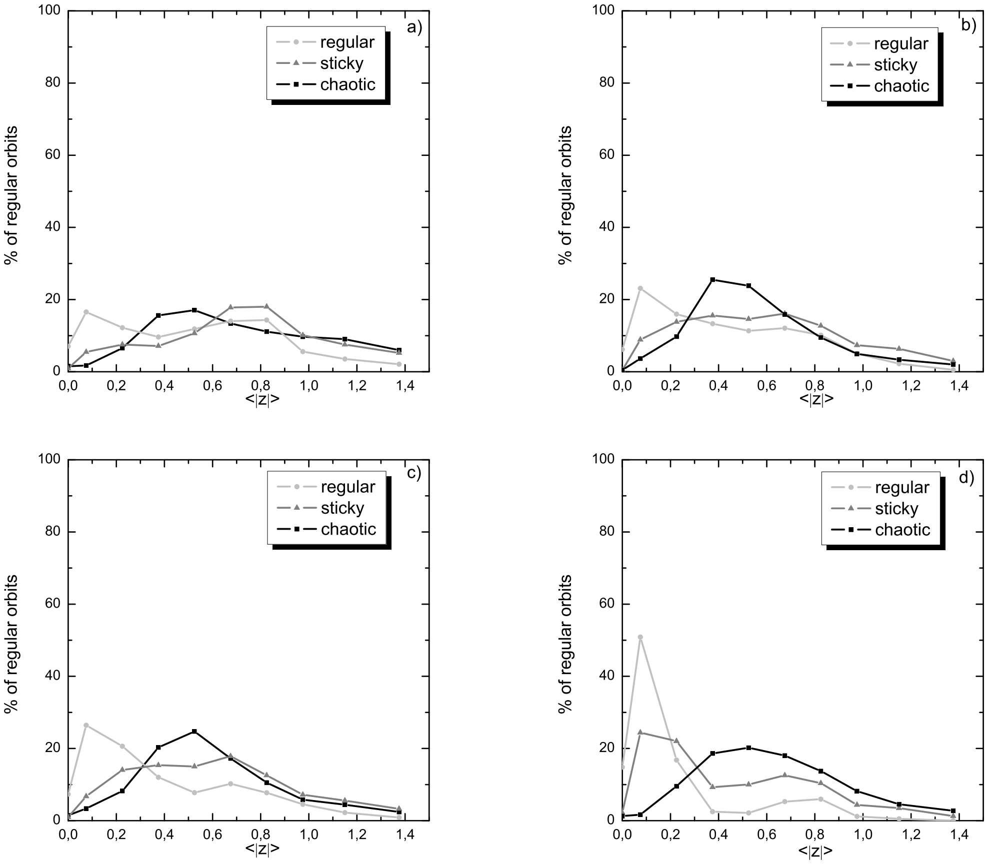

Figure 4.13: Percentages of Case A - for the $MAIN$ (panel a), the $2B$ (panel b), $2C$ (panel c) and $2GMB$ (panel d) model - MAIN version of the ordered, sticky and chaotic orbits for models A,B and C (among the total number of ordered, sticky and chaotic orbits). The curves show how their mean absolute value of the orbits are spread in the short z–axis.

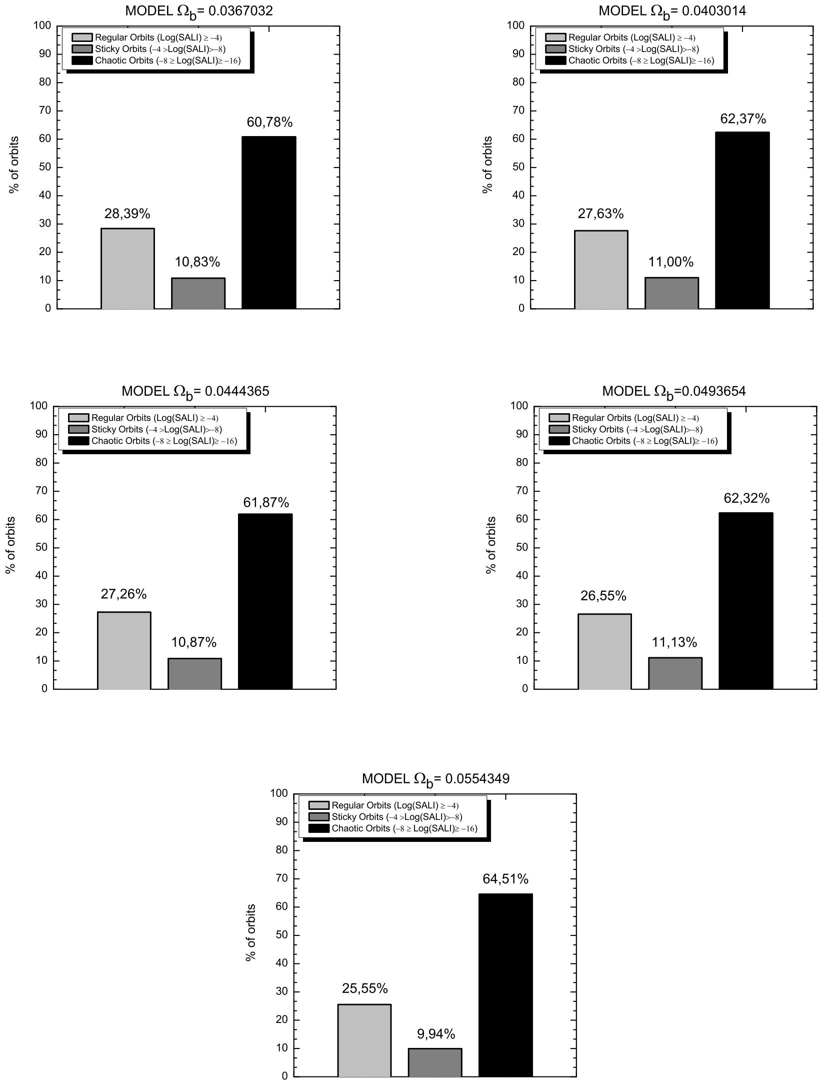

Figure 4.14: The percentages of the chaotic and ordered orbits for the three different values of the pattern speeds. Panel A corresponds to $\Omega_b = 0.0367032$, panel B to $\Omega_b = 0.0403014$, panel C to $\Omega_b = 0.0444365$, panel D to $\Omega_b = 0.0493654$ and panel E to $\Omega_b = 0.0554349$.

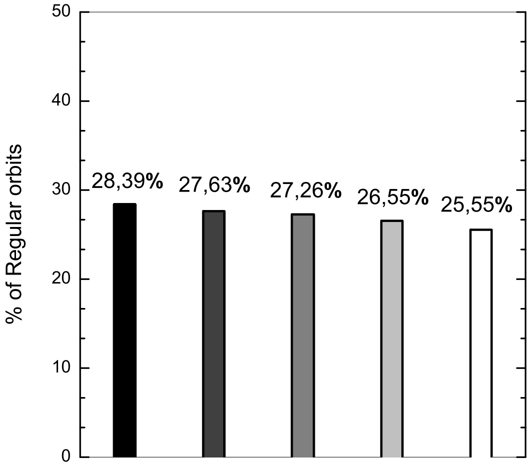

Figure 4.15: Percentages of the regular orbits for Case A (initial conditions on the plane (x, z, p_y) for the 5 Ω_b values,i.e. $\Omega_b = 0.0367032$, $\Omega_b = 0.0403014$,, $\Omega_b = 0.0444365$, $\Omega_b = 0.0493654$ and $\Omega_b = 0.0554349$, for the right to left.

shown in Fig. 4.15. From the orientation of periodic orbits, [24] showed that bars have to end before corotation, i.e. that $r_L > a$, where r_L the Lagrangian, or corotation, radius. Comparing the shape of the observed dust lanes along the leading edges of bars to that of the shock loci in hydrodynamic simulations of gas flow in barred galaxy potentials, [7, 8] was able to set both a lower and an upper limit to corotation radius, namely $r_L = (1.2 \pm 0.2)a$. This restricts the range of possible values of the pattern speed, i.e. $\Omega_b = 0.0367032$, that corresponds to the Lagrangian radius $r_L = 1.4a$ and $\Omega_b = 0.0554349$, that corresponds to $r_L = 1.0a$. Using the extremes of this range, and three extra intermediate values: $\Omega_b = 0.0403014$, $\Omega_b = 0.0444365$ and $\Omega_b = 0.0493654$, that corresponds to the Lagrangian radius $r_L = 1.3a$, $r_L = 1.2a$ and $r_L = 1.1a$ with the parameters that they are given in Table 4.2. We investigated how the pattern speed of the bar affects the system and found that as Ω_b increases the percentage of the regular orbits presents a decreasing trend.

4.3.4 Regular and chaotic orbits in configuration space

We also attempted to explore the way that regular and chaotic orbits are distributed along the z–direction of the configuration space. Following the evolution of each orbit, we calculated the *mean of the absolute value* of their z–coordinate ($< |z| >$). Then, we divided the available $< |z| >$–interval in 30 slices with equal number of orbits in each one of them. This restriction gives us better samples for the estimation of the percentages, implying at the same time that these slices are not equally sized necessarily. For every slice separately we calculated the fraction of regular orbits and in Fig. 4.12b we plot these percentages as a function of the $< |z| >$ in that slice. It reveals that the slices 'near' the (x, y)–plane ($< |z| > \; < 0.35$) contain mainly 'regular' orbits. Contrarily, slices for larger values of mean absolute z values host mainly chaotic motion.

Furthermore, we looked at these percentages as a function of the initial spherical radius ($R_{spherical}$) and the mean spherical radius over the evolution ($< R_{spherical} >$) (Fig. 4.12c,d). Again, dividing

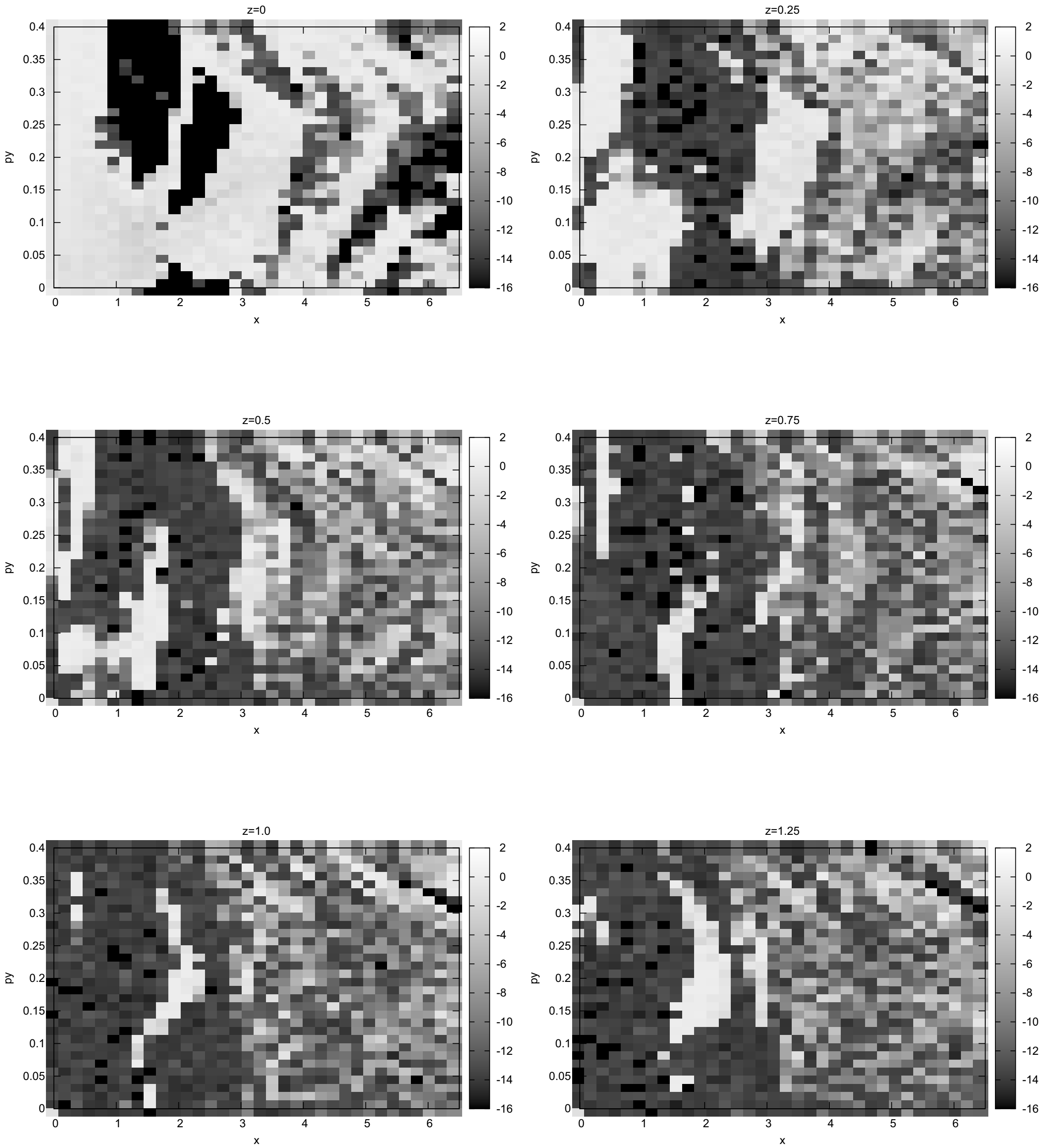

Figure 4.16: Slices of the (x, p_y)-plane for different z values. Dark regions corresponds to the chaotic initial conditions, light gray to the regular and the intermediate colors to the sticky. The color bar represents the values of the SALI in logarithmic scale.

in 30 slices the total range of the $R_{spherical}$, in a similar manner as the $< |z| >$, we calculated the percentages of regular orbits. We plot this for every slice, as a function of the mean $R_{spherical}$ of that slice. We see that the fraction of regular orbits decreases strongly with increasing $R_{spherical}$ up to $R_{spherical} < 1.5$ where it reaches a minimum, while for $1.5 < R_{spherical} < 7$ this percentage starts increasing gradually. This result is in good agreement with the results in Fig. 4.12d, where the horizontal axis corresponds to the value of the mean spherical radius over time of the orbital evolution.

In order to localize the distribution of regular and chaotic orbits in the z–direction, we take the set of initial conditions Case A (version 2C for this example) (x, z, p_y) and we create a mesh in the (x, p_y)–plane with different slices in the z–direction that start from $z = 0$ up to $z = 1.25$ with $step = 0.25$. In Fig. 4.16, we see that as the level that we choose initial conditions on the z-axis increases (starting from the first row and from left to right panels), large islands of stability on the (x, p_y)–plane shrink, especially the big island in the central area, where x is approximately between the values 0 and 2. This trend is almost monotonic up to the z–slice $z \approx 1$ (Fig. 4.16, third row, left panel). For $z = 1.25$ (Fig. 4.16, third row, right panel) the stability region approximately between 1.5 and 2 starts to grow. This result is related and in agreement with the one in Fig. 4.12b, where we have plotted the percentages of regular orbits with the $< |z| >$, i.e. the orbits' mean values in the z-direction during their evolution in time.

Comparing finally, the results in Case A–$MAIN$ model in Fig. 4.13 of the strong ordered (SALI$\geq 10^{-4}$), strong chaotic (SALI$< 10^{-8}$) and sticky or weak chaotic ($10^{-8} \leq$SALI$< 10^{-4}$) orbits (the percentages corresponds in this case to the total number of regular, chaotic and sticky orbits and not to the total amount of orbits) of versus the mean of the absolute value $- < |z| >$ that the orbits spend on the z–axis, it turns out that generally the most part of the regular orbits are near the plane, i.e. $< |z| > \leq 0.3$ roughly. By increasing the lengths of the intermediate or the short axis of the bar, the percentages of the regular orbits don't dramatically change, while when the mass of the bar is increased they are enclosed mostly near to (x, y)–plane than in all the other cases.

4.4 Comparison with Observations

In this section, we attempt to use the obtained information from the dynamical study of the chaotic and regular orbit motion and locate this kind of motion in "real observed stars". A way that this goal could be achieved is by comparing the velocity or momentum distribution of chaotic and regular trajectories in real space. In order to do this we will choose two samples of orbits, one being chaotic and the other regular. But before doing this, let us look more carefully at some characteristics that "typical regular and chaotic" orbits possess:

In Fig. 4.17, we show a "typical" regular orbit with initial condition:

$$(x, z, p_y) = (0.391670, 0.083330, 0.133330).$$

In the first row, we show its $(x, y), (x, z)$–space projections and its GALIs evolution. In the second row, its maximal Lyapunov exponent with its Fourier analysis for the x and z coordinate respectively for the total time evolution. Finally in the third row, the Fourier analysis for three separate time intervals of the orbit evolution of the x–coordinate. All methods are in agreement with the fact that the orbit is regular and they confirm its morphology. The motion is quasiperiodic and the maximal Lyapunov exponent tends asymptotically to zero. The GALI$_{2,3}$ are constant, implying regular motion on a 3 dimensional torus while GALI$_{4,5,6}$ go linearly to zero following power lows as the theory predicts. Its frequency spectra shows clearly the main frequencies of the motion, some occuring in the analysis of the z–coordinate.

Lets now study a “typical” chaotic in Fig. 4.18 in a similar manner with initial condition:

$$(x, z, p_y) = (0.587500, 1.291670, 0.000000).$$

By all methods the orbit looks chaotic first due to its morphology. The scattered motion in the (x, y, z)–plane sis highly irregular and the orbit fills densely the available space. The maximal Lyapunov exponent tends now to a non–zero positive value, while all GALIs indices decay exponentially to zero. Finally, the Fourier analysis shows a spectrum that is continuous without any clear or discrete frequency.

Comparing the above morphologies one can easily predict that the velocity dispersions of these two orbits can't be the same, since the chaotic one seems already to have more spread motion in space, i.e. larger distribution of velocities. But do all chaotic orbits have this kind of irregular profile? The answer is generally not. In Fig. 4.19, we present an example of such a chaotic orbit with initial condition:

$$(x, z, p_y) = (2.350000, 0.088830, 0.133330),$$

which does not look as typically irregular as the previous one. All the known chaos detectors define this trajectory as chaotic although its morphology doesn't imply such behavior. The reason is that the chaotic detectors check the neighboring orbits quite fast and can predict quickly the true nature of the orbit. The phenomenon of slow diffusion is very common in this kind of galaxy models and we found that a big number of this kind of orbits are indeed diffusing so slowly that one should wait too long to observe this behavior (many Hubble times). Some time it's because of the “stickiness” phenomenon: These orbits remain close to islands of stability for long times and thus it takes longer for them to reveal their chaotic nature. Summarizing the above, there is a significant number of chaotic orbits that, by an observational point of view, look more “regular” than “chaotic”, at least when examined during the time interval that we interested in.

In order to relate the “truly” dynamical state of an orbit with orbital motion observed either in simulations or real observations, we study their velocity distributions. For that reason, we should first be able to separate among the chaotic orbits the ones that quickly reveal their nature, since these are the ones that behave irregularly when they are observed. For that reason, we use the Fourier analysis and apply the following procedure:

- We take a representative sample of orbits in one of our models (Case A - MAIN model), which are chaotic according to the GALI method. In this sample there could be some chaotic orbits that are “regular–like” and which we want to exclude.

- On this sample, we perform Fourier analysis to distinguish algorithmically these chaotic orbits that are expected to have a spectrum like a regular orbit, i.e. with discrete frequencies ω_i.

- Based on their Fourier analysis, we calculate initially the total sum of the frequencies amplitudes $\sum_{i=1}^{N} a_i$. Then, we find the maximum amplitudes of the frequencies. We choose the frequency with the first maximum, find all its harmonics and exclude them. Then we locate the frequency with the second maximum amplitude (if one exists) and exclude its harmonics also and so on. Then, we take out the neighbor of these peaks with the noise as well and the frequency spectra is filtered by now. Adding the maximum amplitudes that we have found (one, two or three) and dividing this sum by the sum of total amplitudes of the frequencies we find a percentage.

- It turns out that for regular or “regular–like” orbits this percentage is close to 90–100%, since everything that remains after the filtering procedure is almost the amplitudes of the main frequencies. For the “typical” chaotic orbit, however, this percentage is rather small, i.e. from 0 to 40% generally.

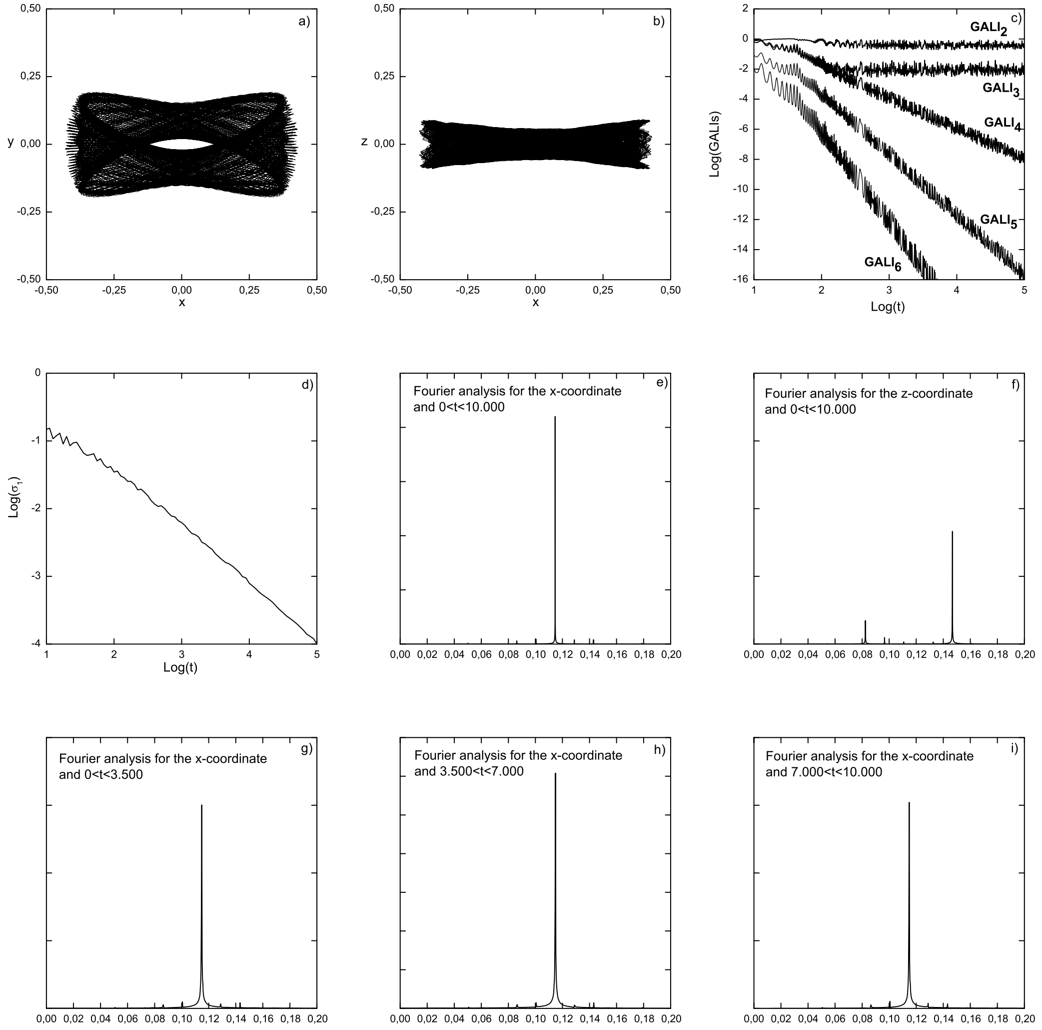

Figure 4.17: Regular orbit with initial condition $(x, z, p_y) = (0.391670, 0.083330, 0.133330)$

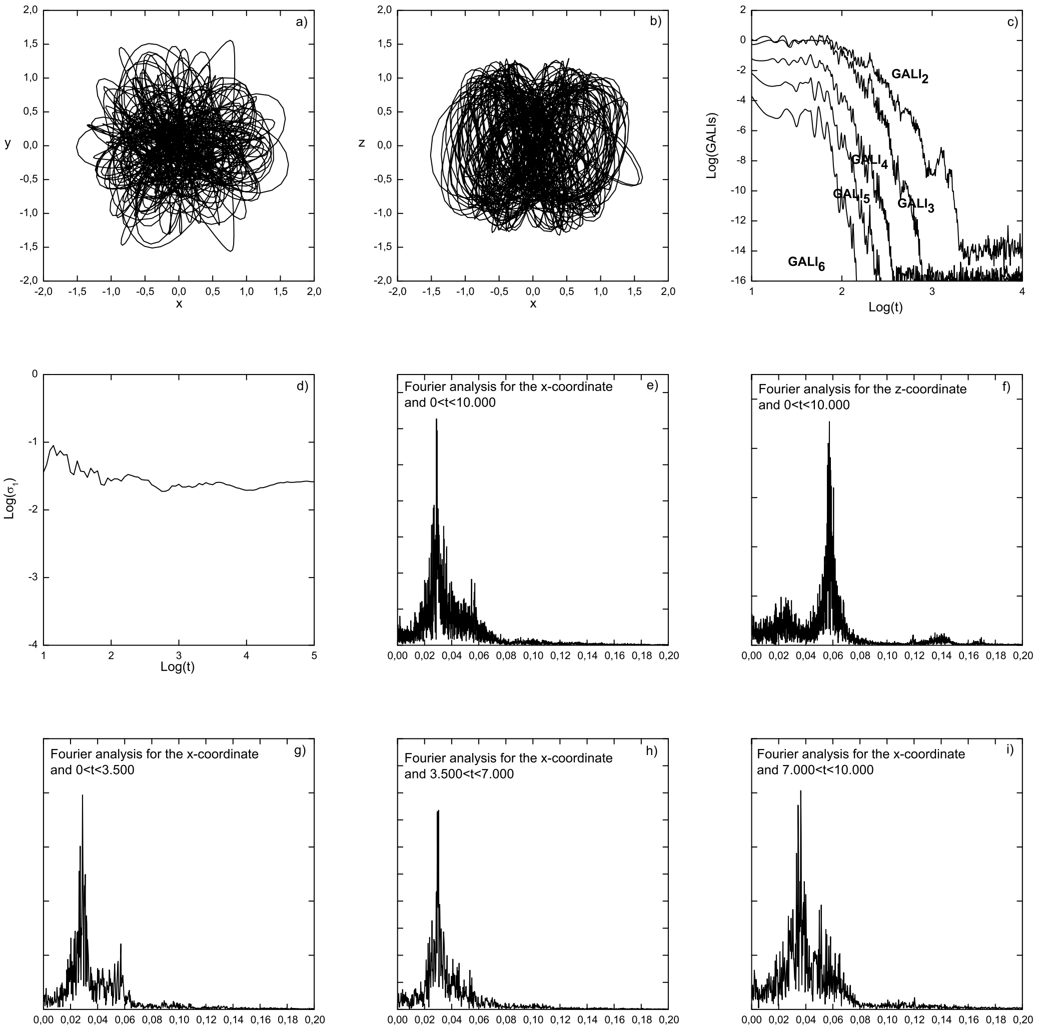

Figure 4.18: Chaotic orbit with initial condition $(x, z, p_y) = (0.587500, 1.291670, 0.000000)$

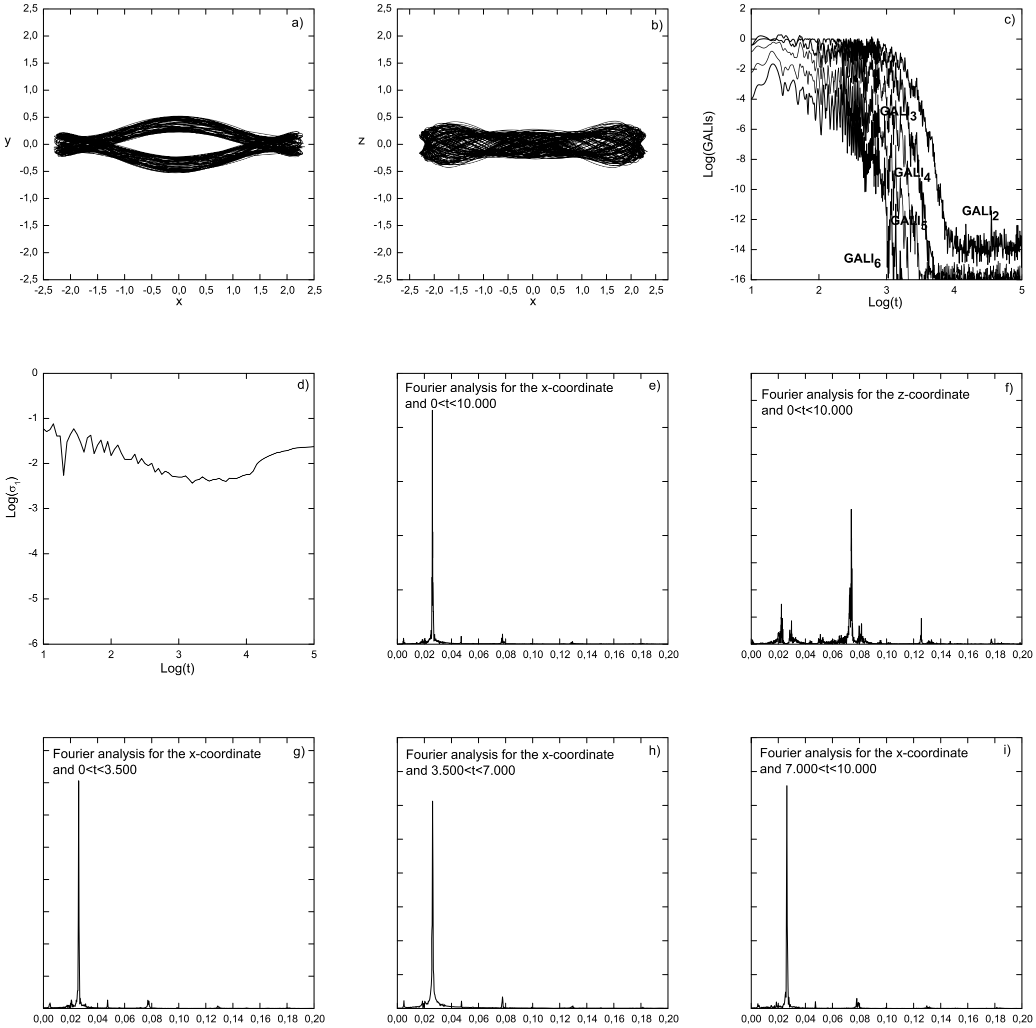

Figure 4.19: A chaotic but "regular–like" orbit in its morphology with initial condition $(x, z, p_y) = (2.350000, 0.088830, 0.133330)$

Having already a sample of regular orbits and using the above procedure as a tool, we can distinguish and reject the "regular–like" orbits (as we described before) among the chaotic ones. We, thus, have an appropriate sample of suitable observational chaotic orbits for our purpose.

4.4.1 Distribution of chaotic and regular obits in configuration space

In this section, we present the different behaviors of the regular and chaotic orbits in the configuration space intersecting several slices along the z–axis. We took a sample of 100 regular and 100 strong chaotic orbits and created a mesh of 1000×1000 boxes on the (x, y)–plane (-6,5$\leq x, y \leq$6.5) at four slices in the positive direction of the z–axis ($0 \leq z \leq 2$). Then, we followed their evolution for the total time of integration t=$10,000$ and measured their visits in each box. The regular orbits show a preference in visiting specific regions on the (x, y)–plane and avoiding the central region. This is more evident in the z–direction, where they are concentrated mainly around two regions. On the other hand, the chaotic orbits tend to spread more uniformly in the (x, y)–plane and pass more frequently through the center. Their distribution on the vertical axis is also more uniform compared to the regular orbits. From our choice of regular orbits in this check, we excluded orbits with initial conditions of the form $(x, z, p_y) = (0, z, 0)$, since they oscillate vertically continuously crossing the plane and that would increase dramatically the density of visits there. This property would prohibit the clear distinction between the different distribution of chaotic and regular motion. In Fig. 4.20 we present the density distribution of chaotic and regular orbits for a slice "near" the (x, y)–plane with small relative thickness in the z–direction, i.e. $z < 0.25$.

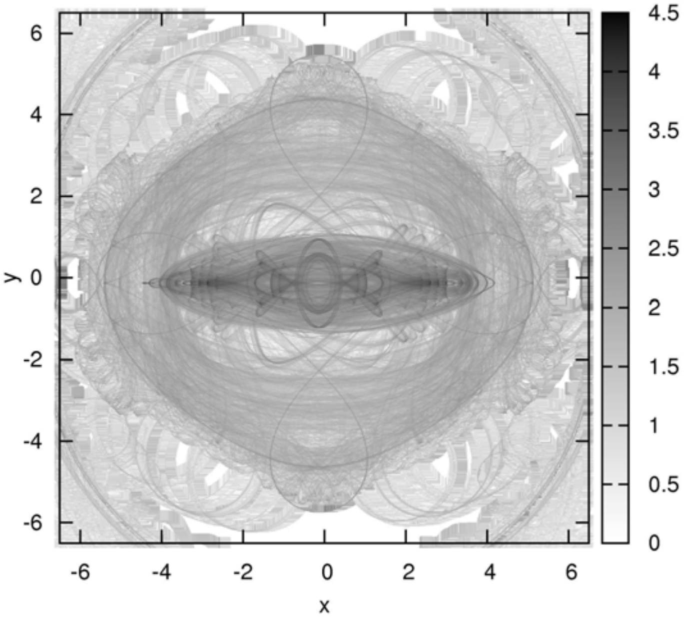

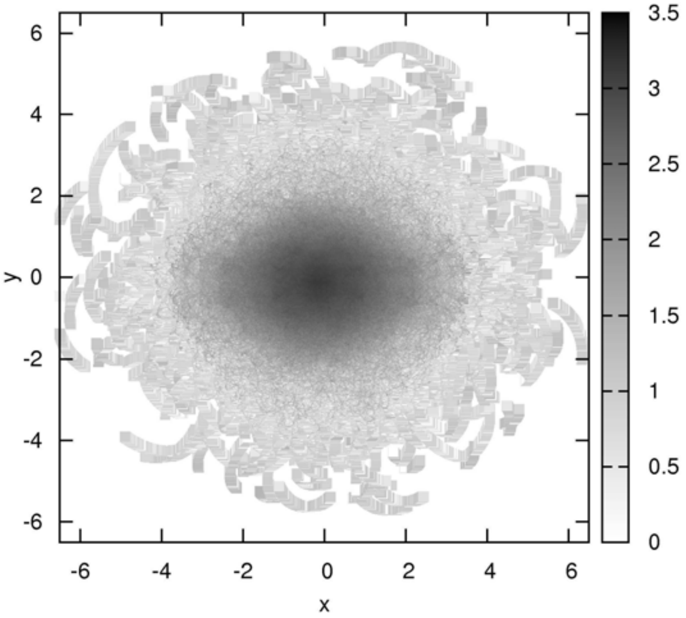

Figure 4.20: Visits of regular (top) and chaotic (bottom) orbits in a grid of 1000×1000 boxes on the (x, y)–plane for a slice with a "small" extension in the positive z–axis ($z < 0.25$). Dark gray boxes correspond to regions where the orbits pass with higher density (the color bar is in logarithmic scale).

4.4.2 Velocity distribution in configuration space

We picked three boxes/spots along the two different directions. Taking a sample of 100 regular and 100 chaotic orbits (by the above described procedure), we integrated them for the total time interval t= $10,000$ and kept the velocities v_x, v_y, v_z each time that they pass through the chosen boxes. By this way, we created diagrams of the v_x, v_y, v_z distribution (Fig 4.21).

Boxes along the x-axis:

Box 1: $x \in [0.5, 0.7]$, $y \in [-0.1, 0.1]$, $z \in [-0.1, 0.1]$
Box 2: $x \in [1.0, 1.2]$, $y \in [-0.1, 0.1]$, $z \in [-0.1, 0.1]$
Box 3: $x \in [2.0, 2.2]$, $y \in [-0.1, 0.1]$, $z \in [-0.1, 0.1]$

Considering that the sample of the orbits could move either in the same direction with the bar (having velocities with positive values – like those quasiperiodic orbits around the periodic orbit x_1) or inversely (with negative velocities, like those quasiperiodic orbits around the retrograde periodic orbit x_4), it is expected to observe both positive and negative values for both the regular and chaotic orbits. The regular orbits seem to be populated in two peaks around zero while the chaotic are spread in more uniform way around the zero value (see Fig. 4.21a,b,c). The velocities of regular orbits, depending on the chosen box, could some times be located in values around zero.

It seems that usually regular orbits tend to form one or more (depending on the variety and complexity of the orbits) relatively steep "Gaussian–like distribution(s)". On the other hand, the velocities of the chaotic orbits tend to form a quite different and outspread velocity–distribution.

Similar results were obtained when we chose three boxes like just above but now along the y–axis.

Boxes along the y-axis:

Box 1: $x \in [-0.1, 0.1]$, $y \in [0.5, 0.7]$, $z \in [-0.1, 0.1]$
Box 2: $x \in [-0.1, 0.1]$, $y \in [1.0, 1.2]$, $z \in [-0.1, 0.1]$
Box 3: $x \in [-0.1, 0.1]$, $y \in [2.0, 2.2]$, $z \in [-0.1, 0.1]$

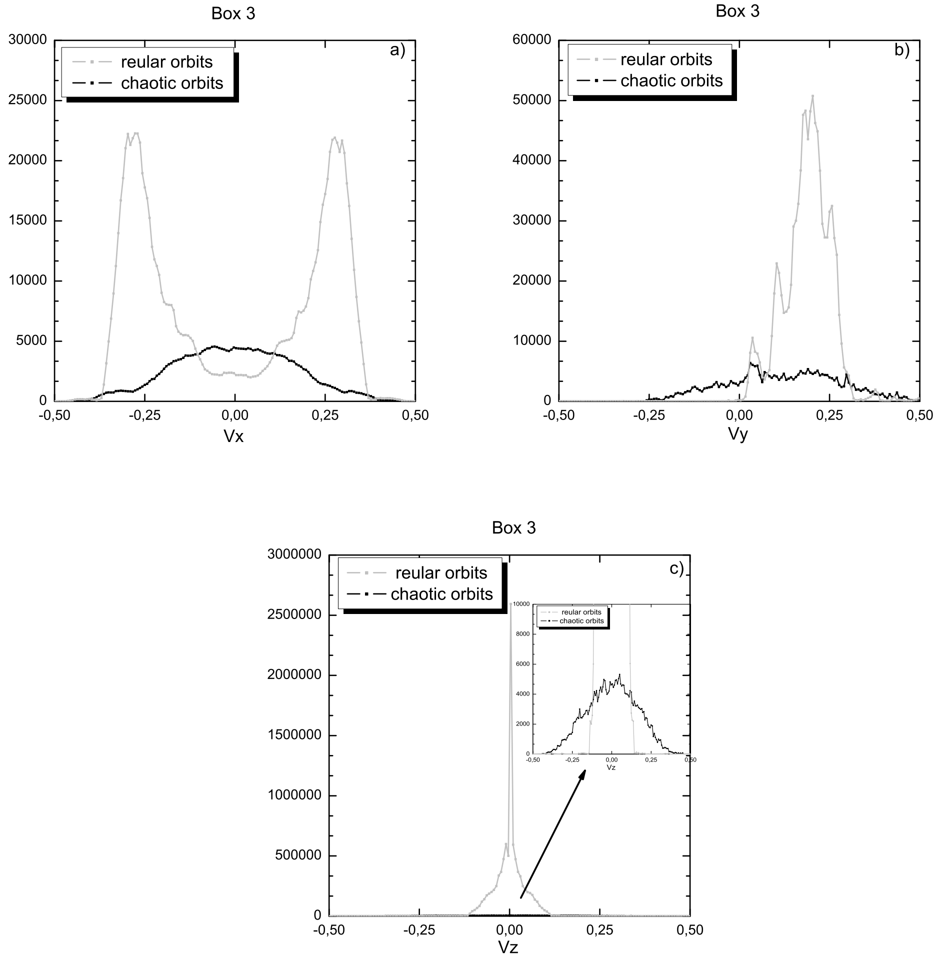

Figure 4.21: Velocity distributions for regular and chaotic orbits for Box 3 along the x–axis.

CHAPTER 5

CONCLUSIONS AND FUTURE OUTLOOK

In this thesis, we have attempted a thorough study of regular and chaotic motion in systems of area–conserving coupled symplectic maps and in models of barred galaxies described by Hamiltonian dynamics. The special properties of the coupled maps, i.e. the convenience of their computation and the universality of their dynamics, gave us the chance to apply and explore, in a full extent, the abilities of the GALI method in distinguishing rapidly and efficiently between regular and chaotic motion. Understanding initially, its behavior in low–dimensional examples, we turned to the case of N coupled standard maps and we were able to distinguish quickly and reliably, not only chaotic from regular behavior but also among different types of regular motion depending on the dimensionality of the tori in the $2N$–dimensional phase space. In order to achieve this goal, we worked with two different types of initial conditions: a) localized in real space, exciting a “small” number of particles (called breathers) and studying their regular or chaotic motion and b) localized in Fourier space (called q–breathers), exciting only a “small” number of normal modes and studying recurrence phenomena.

Using then our dynamical indicators, we studied thoroughly the Ferrers’ barred galaxy models from a dynamical point view and tried to relate our theoretical results with real astronomical data that could be observed. In order to accomplish this, we applied the SALI and GALI criteria for their qualitative and quantitative distinction of the orbits in phase space. In 2 degrees of freedom Ferrers’s models, we were able to identify tiny regions of regular or chaotic motion, which are not clearly visible on Poincaré surfaces of section. We have also computed percentages of regular, “sticky” and chaotic orbits varying the values of the main parameters, such as the energy (in the 2D model) or the length and the mass of the bar component (in the 3D model). Chaos turns out to be dominant in galaxy models whose bar component is more massive, while models with thicker width or longer bar length present generally more regular behavior.

Additionally in the 3D model, we used $\text{GALI}_{2,3}$ to show that these are cases where the torus on which a regular orbit lies is 2–dimensional, while the expected dimension of the tori is 3. Concerning chaotic orbits the $\text{GALI}_{3,4,5,6}$ indices decay faster than SALI (or GALI_2) and are able to detect chaos at times when this is not yet evident by the calculation of the maximal Lyapunov characteristic exponents. We also studied how the regular motion varies as the energy increases, and found that the percentages of regular initial conditions decrease up to a certain energy value and then start to increase again. We also found that bars that rotate faster are more chaotic and that, generally, percentages of regular motion (in terms of initial conditions in phase space) decrease sharply at small radial distances from the center of the galaxy and also do not extend relatively far in the z–direction.

We then extended our study of the chaotic and regular orbits in 3D galaxy models and focus on answering questions of relevance to astronomy. Different meshes of initial conditions were used for the detailed and global understanding of the full phase space. Addressing our applications to strictly astronomical properties of the orbits in order to understand better their physical interpretation, we analyzed the Fourier spectrum of the regular and chaotic trajectories. Different types of chaotic motion in the (x, y, z)–configuration space were studied and chaotic orbits were found that one could say behave in a "regular" way, at least for time intervals with a physical significance, i.e. one Hubble time. By these combined techniques, we were able to separate a "purely" chaotic orbital motion from regular studying their different characteristics as observed in real galaxies, such as: their morphology and velocity (or momentum) distributions in configuration space. We showed that momentum distribution diagrams can be used as a tool in N body simulations to locate a possibly "pure" chaotic motion in a real galaxy.

Although many tools and aspects of the theory of the nonlinear dynamical systems and methods of chaos detection were studied and applied in this thesis for the understanding of barred galaxies, there are still plenty of open problems to be explored and questions to be answered. Double barred galaxies has been recently studied in [36, 37, 73, 74] which can also be analyzed using our tools in order locate chaotic motion in the full 3 degree of freedom potential. There could also be applications in galaxy models with black holes at their center, while it would be interesting to study in detail their halo effect in the global stability of the phase space and the amount of chaotic (or regular) motion in the configuration space that could be associated with realistic astronomical data. Furthermore, these techniques can also be applied to self–consistent N body simulations [7, 8] to compare their efficiency and results with those of the analytical potentials.

CHAPTER 6

APPENDICES

6.1 Appendix I: Potentials – Density Pairs

6.1.1 Miyamoto–Nagai model

The Miyamoto–Nagai potential (1975) [84, 85], is described by the following equation:

$$\Phi(R,z) = -\frac{GM}{\sqrt{R^2 + (A + \sqrt{B^2 + z^2})^2}}, \tag{6.1}$$

where $R^2 = x^2 + y^2$ is the radius of the disc, G is the gravitational constant, M is the mass disc and the parameters A and B characterize the disc's shape. The corresponding density distribution function is computed by the Poisson's equation and it has the form:

$$\rho = (\frac{B^2 M}{4\pi})\frac{AR^2 + (A + 3\sqrt{z^2 + B^2})((A + \sqrt{z^2 + B^2})^2}{[R^2 + (A + \sqrt{z^2 + B^2})^2]^{5/2}(z^2 + B^2)^{3/2}} \tag{6.2}$$

The first and the second derivatives of the potential are:

$$\begin{aligned}
\Phi_x &= \frac{GMx}{[R^2+(A+\sqrt{B^2+z^2})^2]^{3/2}} \\
\Phi_y &= \frac{GMy}{[R^2+(A+\sqrt{B^2+z^2})^2]^{3/2}} \\
\Phi_z &= GMz(1+\frac{A}{\sqrt{B^2+z^2}})(\frac{1}{[R^2+(A+\sqrt{B^2+z^2})^2]^{3/2}}) \\
\Phi_{xx} &= \frac{GM}{R^2+(A+\sqrt{B^2+z^2})^2]^{3/2}}(1-\frac{3x^2}{[R^2+(A+\sqrt{B^2+z^2})^2]}) \\
\Phi_{yy} &= \frac{GM}{R^2+(A+\sqrt{B^2+z^2})^2]^{3/2}}(1-\frac{3y^2}{[R^2+(A+\sqrt{B^2+z^2})^2]}) \\
\Phi_{zz} &= \frac{GM}{R^2+(A+\sqrt{B^2+z^2})^2]^{3/2}}\{(1+\frac{A}{\sqrt{B^2+z^2}})-\frac{3z^2}{[R^2+(A+\sqrt{z^2+B^2})^2]} \qquad (6.3) \\
&\times \ (1+\frac{A}{\sqrt{B^2+z^2}})^2-\frac{Az^2}{(\sqrt{B^2+z^2})^{3/2}}\} \\
\Phi_{xy} &= \frac{-3GMxy}{[R^2+(A+\sqrt{B^2+z^2})^2]^{5/2}} \\
\Phi_{xz} &= \frac{-3GMxz}{[R^2+(A+\sqrt{B^2+z^2})^2]^{5/2}}(1+\frac{A}{\sqrt{B^2+z^2}}) \\
\Phi_{yz} &= \frac{-3GMyz}{[R^2+(A+\sqrt{B^2+z^2})^2]^{5/2}}(1+\frac{A}{\sqrt{B^2+z^2}})
\end{aligned}$$

6.1.2 Bulge sphere

The potential of the Plummer sphere is:

$$\Phi = -\frac{GM_S}{\sqrt{R^2+\epsilon_s^2}}, \qquad (6.4)$$

where $R^2 = x^2 + y^2 + z^2$, ϵ_s is the scalelength of the bulge, G is the gravitational constant and M is its total mass.

6.1.3 Ferrers' ellipsoid

A triaxial Ferrers *bar*, the density $\rho(x)$ of which is [39]:

$$\rho(x) = \begin{cases} \rho_c(1-m^2)^n & ,m<1 \\ 0 & ,m\geq 1 \end{cases}, \qquad (6.5)$$

where $\rho_c = \frac{105}{32\pi}\frac{GM}{abc}$ is the central density, M is the total mass of the bar, n represents the homogeneity degree and

$$m^2 = \frac{x^2}{a^2}+\frac{y^2}{b^2}+\frac{z^2}{c^2}, \qquad a>b>c>0, \qquad (6.6)$$

with a, b and c being the semi-axes. Following Chandrasekhar (1969), the density distribution represents an inhomogeneous ellipsoidal figure with potential:

$$\Phi = -\pi Gabc\frac{\rho_c}{n+1}\int_{\lambda}^{\infty}\frac{du}{\Delta(u)}(1-m^2(u))^{n+1}, \qquad (6.7)$$

where

$$m^2(u) = \frac{x^2}{a^2+u} + \frac{y^2}{b^2+u} + \frac{z^2}{c^2+u}, \tag{6.8}$$

$$\Delta^2(u) = (a^2+u)(b^2+u)(c^2+u), \tag{6.9}$$

λ is the unique positive solution of $m^2(\lambda) = 1$, if $m \geq 1$, that is, if the particle is outside of the bar and $\lambda = 0$ inside the bar. From the above, it is clear that the potential, in fact, is a function of the position of the particle (x, y, z) and of the parameter λ. Thus, we can conclude that this potential satisfies the property $\partial_\lambda \Phi = 0$. Furthermore, using a multinomial expansion of the $(1 - m^2(u))^{n+1}$, we can simplify the expression of the potential.

$$\begin{aligned} (1-m^2(u))^{n+1} &= (1 - \frac{x^2}{a^2+u} + \frac{y^2}{b^2+u} + \frac{z^2}{c^2+u})^{n+1} \\ &= \sum_{i+j+k+l=n+1} \frac{(n+1)!}{i!j!k!l!} 1^i (\frac{x^2}{a^2+u})^j (\frac{y^2}{b^2+u})^k (\frac{z^2}{c^2+u})^l (-1)^{n-i+1} \\ &= \sum_{i+j+k+l=n+1} \frac{(n+1)!}{i!j!k!l!} (-1)^{n-i+1} x^{2j} y^{2k} z^{2l} (\frac{1}{a^2+u})^j (\frac{1}{b^2+u})^k (\frac{1}{c^2+u})^l \end{aligned} \tag{6.10}$$

Substituting this expression into the potential, we get

$$\begin{aligned} \Phi &= -\pi Gabc \frac{\rho_c}{n+1} \int_\lambda^\infty \frac{du}{\Delta(u)} \{ \sum_{i+j+k+l=n+1} \frac{(n+1)!}{i!j!k!l!} (-1)^{n-i+1} x^{2j} y^{2k} z^{2l} \frac{1}{(a^2+u)^j} \frac{1}{(b^2+u)^k} (\frac{1}{(c^2+u)^l} \} \\ &= -\pi Gabc\rho_c \sum_{i+j+k+l=n+1} \frac{n!}{i!j!k!l!} (-1)^{n-i} x^{2j} y^{2k} z^{2l} \int_\lambda^\infty \frac{du}{\Delta(u)} \frac{1}{(a^2+u)^j (b^2+u)^k (c^2+u)^l} \\ &= -\pi Gabc\rho_c \sum_{i+j+k+l=n+1} \frac{n!}{i!j!k!l!} (-1)^{n-i} x^{2j} y^{2k} z^{2l} W_{jkl} \end{aligned} \tag{6.11}$$

where w_{jkl} depends on λ and is defined as

$$W_{jkl} = \int_\lambda^\infty \frac{du}{\Delta(u)} \frac{1}{(a^2+u)^j (b^2+u)^k (c^2+u)^l}. \tag{6.12}$$

We have computed W_{jkl} like Pfenniger (1984) [95], and they depend on the elliptic integrals of first and second order, E and F, respectively. As we already mentioned, W_{jkl} depend on λ, and at the same time, λ depends on the point (x, y, z). In order to get the derivatives, we have to compute the derivatives of W_{jkl} with respect to x, y and z:

$$\begin{aligned} \frac{\partial W_{jkl}}{\partial x} &= \frac{\partial W_{jkl}}{\partial \lambda} \frac{\partial \lambda}{\partial x} \\ \frac{\partial W_{jkl}}{\partial y} &= \frac{\partial W_{jkl}}{\partial \lambda} \frac{\partial \lambda}{\partial y} \\ \frac{\partial W_{jkl}}{\partial z} &= \frac{\partial W_{jkl}}{\partial \lambda} \frac{\partial \lambda}{\partial z} \end{aligned} \tag{6.13}$$

So, we need to calculate the quantities $\frac{\partial W_{jkl}}{\partial\lambda}$, $\frac{\partial\lambda}{\partial x}$, $\frac{\partial\lambda}{\partial y}$ and $\frac{\partial\lambda}{\partial z}$:

$$\begin{aligned}
\frac{\partial W_{jkl}}{\partial\lambda} &= -\frac{1}{(a^2+\lambda)^{i+1/2}(b^2+\lambda)^{j+1/2}(c^2+\lambda)^{k+1/2}}\\
\frac{\partial\lambda}{\partial x} &= \frac{\frac{2x}{a^2+\lambda}}{\frac{x^2}{(a^2+\lambda)^2}+\frac{y^2}{(b^2+\lambda)^2}+\frac{z^2}{(c^2+\lambda)^2}}\\
\frac{\partial\lambda}{\partial y} &= \frac{\frac{2y}{b^2+\lambda}}{\frac{x^2}{(a^2+\lambda)^2}+\frac{y^2}{(b^2+\lambda)^2}+\frac{z^2}{(c^2+\lambda)^2}}\\
\frac{\partial\lambda}{\partial z} &= \frac{\frac{2z}{c^2+\lambda}}{\frac{x^2}{(a^2+\lambda)^2}+\frac{y^2}{(b^2+\lambda)^2}+\frac{z^2}{(c^2+\lambda)^2}}
\end{aligned}$$

Since, $\partial\Phi\ \partial\lambda = 0$:

$$0 = \frac{\partial\Phi}{\partial\lambda} = -\pi Gabc\rho_c \sum_{i+j+k+l=n+1} \frac{n!}{i!j!k!l!}(-1)^{n-i}x^{2j}y^{2k}z^{2l}\frac{\partial W_{jkl}}{\partial\lambda}$$

Therefore, we compute the first and second derivatives, for example, with respect to the variable x:

$$\begin{aligned}
\frac{d\Phi}{dx} &= \frac{\partial\Phi}{\partial x} + \frac{\partial\Phi}{\partial\lambda}\frac{\partial\lambda}{\partial x}\\
&= -\pi Gabc\rho_c \sum_{i+j+k+l=n+1} \frac{n!}{i!j!k!l!}(-1)^{n-i}(2j)x^{2j-1}y^{2k}z^{2l}W_{jkl}\\
\frac{d^2\Phi}{dx^2} &= -\pi Gabc\rho_c\{ \sum_{i+j+k+l=n+1} \frac{n!}{i!j!k!l!}(-1)^{n-i}(2j)(2j-1)x^{2j-2}y^{2k}z^{2l}W_{jkl}\\
&+ \frac{\partial\lambda}{\partial x}(\sum_{i+j+k+l=n+1} \frac{n!}{i!j!k!l!}(-1)^{n-i}(2j)x^{2j-1}y^{2k}z^{2l}\frac{\partial W_{jkl}}{\partial\lambda})\}
\end{aligned}$$

Homogeneous bar potential $n = 0$

We obtain the expression of the potential for $n = 0$ by substituting $n = 0$ in the general expression:

$$\begin{aligned}
\Phi(x,y,z) &= -\pi Gabc\rho_c \sum_{i+j+k+l=1} \frac{0!}{i!j!k!l!}(-1)^{-i}x^{2j}y^{2k}z^{2l}W_{jkl}\\
&= -\pi Gabc\rho_c(-W_{000} + x^2W_{100} + y^2W_{010} + z^2W_{001})
\end{aligned}$$

Setting $C = -\pi G abc\rho_c$, the first and second derivatives of this potential are:

$$\begin{aligned}
\Phi_x &= 2CxW_{100} \\
\Phi_y &= 2CyW_{010} \\
\Phi_z &= 2CzW_{001} \\
\Phi_{xx} &= 2C(W_{100} + x\frac{\partial W_{100}}{\partial \lambda}\frac{\partial \lambda}{\partial x}) \\
\Phi_{yy} &= 2C(W_{010} + y\frac{\partial W_{010}}{\partial \lambda}\frac{\partial \lambda}{\partial y}) \\
\Phi_{zz} &= 2C(W_{001} + z\frac{\partial W_{001}}{\partial \lambda}\frac{\partial \lambda}{\partial z}) \\
\Phi_{xy} &= 2Cx\frac{\partial W_{100}}{\partial \lambda}\frac{\partial \lambda}{\partial y}, \Phi_{yx} = 2Cy\frac{\partial W_{010}}{\partial \lambda}\frac{\partial \lambda}{\partial x} \\
\Phi_{xz} &= 2Cx\frac{\partial W_{100}}{\partial \lambda}\frac{\partial \lambda}{\partial z}, \Phi_{zx} = 2Cz\frac{\partial W_{001}}{\partial \lambda}\frac{\partial \lambda}{\partial x} \\
\Phi_{yz} &= 2Cy\frac{\partial W_{010}}{\partial \lambda}\frac{\partial \lambda}{\partial z}, \Phi_{zy} = 2Cz\frac{\partial W_{001}}{\partial \lambda}\frac{\partial \lambda}{\partial y}
\end{aligned} \tag{6.14}$$

Inhomogeneous bar distribution, $n = 1$

In a similar manner as before we set now $n = 1$ in the general case.

$$\begin{aligned}
\Phi(x,y,z) &= -\pi G abc\rho_c \sum_{i+j+k+l=2} \frac{1!}{i!j!k!l!}(-1)^{1-i}x^{2j}y^{2k}z^{2l}W_{jkl} \\
&= -\pi G abc\rho_c(-\frac{1}{2}W_{000} + x^2W_{100} + y^2W_{010} + z^2W_{001} - \\
&- x^2y^2W_{110} - x^2z^2W_{101} - y^2z^2W_{011} - \frac{1}{2}x^4W_{200} - \frac{1}{2}y^4W_{020} - \frac{1}{2}z^4W_{002})
\end{aligned} \tag{6.15}$$

Setting again $C = -\pi G abc\rho_c$, the first and second derivatives of this potential are:

$$
\begin{aligned}
\Phi_x &= 2Cx(W_{100} - x^2 W_{200} - y^2 W_{110} - z^2 W_{101} \qquad (6.16)\\
\Phi_y &= 2Cy(W_{010} - x^2 W_{110} - y^2 W_{020} - z^2 W_{011}\\
\Phi_z &= 2Cz(W_{001} - x^2 W_{101} - y^2 W_{011} - z^2 W_{002}\\
\Phi_{xx} &= 2C(W_{100} - 3x^2 W_{200} - y^2 W_{110} - z^2 W_{101} + x\frac{\partial\lambda}{\partial x}(\frac{\partial W_{100}}{\partial\lambda} - x^2\frac{\partial W_{200}}{\partial\lambda} - y^2\frac{\partial W_{110}}{\partial\lambda} - z^2\frac{\partial W_{101}}{\partial\lambda}))\\
\Phi_{yy} &= 2C(W_{010} - x^2 W_{200} - 3y^2 W_{020} - z^2 W_{011} + y\frac{\partial\lambda}{\partial y}(\frac{\partial W_{010}}{\partial\lambda} - x^2\frac{\partial W_{110}}{\partial\lambda} - y^2\frac{\partial W_{020}}{\partial\lambda} - z^2\frac{\partial W_{011}}{\partial\lambda}))\\
\Phi_{zz} &= 2C(W_{001} - x^2 W_{101} - y^2 W_{011} - 3z^2 W_{002} + z\frac{\partial\lambda}{\partial z}(\frac{\partial W_{001}}{\partial\lambda} - x^2\frac{\partial W_{101}}{\partial\lambda} - y^2\frac{\partial W_{011}}{\partial\lambda} - z^2\frac{\partial W_{002}}{\partial\lambda}))\\
\Phi_{xy} &= 4CxyW_{110} + 2Cx\frac{\partial\lambda}{\partial y}(\frac{\partial W_{100}}{\partial\lambda} - x^2\frac{\partial W_{200}}{\partial\lambda} - y^2\frac{\partial W_{110}}{\partial\lambda} - z^2\frac{\partial W_{101}}{\partial\lambda}))\\
\Phi_{xz} &= 4CxzW_{101} + 2Cx\frac{\partial\lambda}{\partial z}(\frac{\partial W_{100}}{\partial\lambda} - x^2\frac{\partial W_{200}}{\partial\lambda} - y^2\frac{\partial W_{110}}{\partial\lambda} - z^2\frac{\partial W_{101}}{\partial\lambda}))\\
\Phi_{yz} &= 4CyzW_{011} + 2Cy\frac{\partial\lambda}{\partial z}(\frac{\partial W_{010}}{\partial\lambda} - x^2\frac{\partial W_{110}}{\partial\lambda} - y^2\frac{\partial W_{020}}{\partial\lambda} - z^2\frac{\partial W_{011}}{\partial\lambda}))
\end{aligned}
$$

Inhomogeneous bar ending sharply, $n = 2$

Substituting $n = 2$ to the general case, we get:

$$
\begin{aligned}
\Phi(x,y,z) &= \frac{C}{6}\{W_{000} - 6x^2y^2z^2W_{111} + \qquad (6.17)\\
&+ x^2[x^2(3W_{200} - x^2W_{300}) + 3(y^2(2W_{110} - y^2W_{120} - x^2W_{210}) - W_{100})] +\\
&+ y^2[y^2(3W_{020} - y^2W_{030}) + 3(z^2(2W_{011} - z^2W_{012} - y^2W_{021}) - W_{010})] +\\
&+ z^2[z^2(3W_{002} - z^2W_{003}) + 3(x^2(2W_{101} - x^2W_{201} - z^2W_{102}) - W_{001})]\},
\end{aligned}
$$

where $C = -\pi G abc\rho_c$.

The first and second derivatives of this potential are:

$$
\begin{aligned}
\Phi_x &= -Cx[W_{100} + x^2(x^2W_{300} + 2(y^2W_{210} - W_{200})) + \\
&+ y^2(y^2W_{120} + 2(z^2W_{111} - W_{110})) + z^2(z^2W_{102} + 2(x^2W_{201} - W_{101}))] \\
\Phi_y &= -Cy[W_{010} + x^2(x^2W_{210} + 2(y^2W_{120} - W_{110})) + \\
&+ y^2(y^2W_{030} + 2(z^2W_{021} - W_{020})) + z^2(z^2W_{012} + 2(x^2W_{111} - W_{011}))] \\
\Phi_z &= -Cz[W_{001} + x^2(x^2W_{201} + 2(y^2W_{111} - W_{101})) + \\
&+ y^2(y^2W_{021} + 2(z^2W_{012} - W_{011})) + z^2(z^2W_{003} + 2(x^2W_{102} - W_{002}))] \\
\Phi_{xx} &= -C[W_{100} + x^2(5x^2W_{300} + 6(y^2W_{210} - W_{200})) + \\
&+ y^2(y^2W_{120} + 2(z^2W_{111} - W_{110})) + z^2(z^2W_{102} + 6x^2W_{201} - 2W_{101})] - \\
&- \frac{\partial\lambda}{\partial x}Cx[\frac{W_{100}}{\partial\lambda} + x^2(x^2\frac{W_{300}}{\partial\lambda} + 2(y^2\frac{W_{210}}{\partial\lambda} - \frac{W_{200}}{\partial\lambda})) + \\
&+ y^2(y^2\frac{W_{120}}{\partial\lambda} + 2(z^2\frac{W_{111}}{\partial\lambda} - \frac{W_{110}}{\partial\lambda})) + z^2(z^2\frac{W_{102}}{\partial\lambda} + 2(x^2\frac{W_{201}}{\partial\lambda} - \frac{W_{101}}{\partial\lambda}))] \\
\Phi_{yy} &= -C[W_{010} + x^2(x^2W_{210} + 6(y^2W_{120} - W_{110})) + \\
&+ y^2(5y^2W_{030} + 6z^2W_{021} - 6W_{020}) + z^2(2x^2W_{111} + z^2W_{012} - 2W_{011})] - \\
&- \frac{\partial\lambda}{\partial y}Cy[\frac{W_{010}}{\partial\lambda} + x^2(x^2\frac{W_{210}}{\partial\lambda} + 2(y^2\frac{W_{120}}{\partial\lambda} - \frac{W_{110}}{\partial\lambda})) + \\
&+ y^2(y^2\frac{W_{030}}{\partial\lambda} + 2(z^2\frac{W_{021}}{\partial\lambda} - \frac{W_{020}}{\partial\lambda})) + z^2(z^2\frac{W_{012}}{\partial\lambda} + 2(x^2\frac{W_{111}}{\partial\lambda} - \frac{W_{011}}{\partial\lambda}))] \\
\Phi_{zz} &= -C[W_{001} + x^2(x^2W_{201} + 2y^2W_{111} - 2W_{101}) + \\
&+ y^2(y^2W_{0210} + 6z^2W_{012} - 2W_{011}) + z^2(5z^2W_{003} + 6x^2W_{102} - 6W_{002})] - \\
&- \frac{\partial\lambda}{\partial z}Cz[\frac{W_{001}}{\partial\lambda} + x^2(x^2\frac{W_{201}}{\partial\lambda} + 2(y^2\frac{W_{111}}{\partial\lambda} - \frac{W_{101}}{\partial\lambda})) + \\
&+ y^2(y^2\frac{W_{021}}{\partial\lambda} + 2(z^2\frac{W_{012}}{\partial\lambda} - \frac{W_{011}}{\partial\lambda})) + z^2(z^2\frac{W_{003}}{\partial\lambda} + 2(x^2\frac{W_{102}}{\partial\lambda} - \frac{W_{002}}{\partial\lambda}))] \\
\Phi_{xy} &= -4Cxy(x^2W_{210} + y^2W_{120} + z^2W_{111} - W_{110}) - \\
&- \frac{\partial\lambda}{\partial y}Cx[\frac{W_{100}}{\partial\lambda} + x^2(x^2\frac{W_{300}}{\partial\lambda} + 2(y^2\frac{W_{210}}{\partial\lambda} - \frac{W_{200}}{\partial\lambda})) + \\
&+ y^2(y^2\frac{W_{120}}{\partial\lambda} + 2(z^2\frac{W_{111}}{\partial\lambda} - \frac{W_{110}}{\partial\lambda})) + z^2(z^2\frac{W_{102}}{\partial\lambda} + 2(x^2\frac{W_{201}}{\partial\lambda} - \frac{W_{101}}{\partial\lambda}))] \\
\Phi_{xz} &= -4Cxz(x^2W_{201} + y^2W_{111} + z^2W_{102} - W_{101}) - \\
&- \frac{\partial\lambda}{\partial z}Cx[\frac{W_{100}}{\partial\lambda} + x^2(x^2\frac{W_{300}}{\partial\lambda} + 2(y^2\frac{W_{210}}{\partial\lambda} - \frac{W_{200}}{\partial\lambda})) + \\
&+ y^2(y^2\frac{W_{120}}{\partial\lambda} + 2(z^2\frac{W_{111}}{\partial\lambda} - \frac{W_{110}}{\partial\lambda})) + z^2(z^2\frac{W_{102}}{\partial\lambda} + 2(x^2\frac{W_{201}}{\partial\lambda} - \frac{W_{101}}{\partial\lambda}))] \\
\Phi_{yz} &= -4Cyz(x^2W_{111} + y^2W_{021} + z^2W_{012} - W_{011}) - \\
&- \frac{\partial\lambda}{\partial z}Cx[\frac{W_{001}}{\partial\lambda} + x^2(x^2\frac{W_{201}}{\partial\lambda} + 2(y^2\frac{W_{111}}{\partial\lambda} - \frac{W_{101}}{\partial\lambda})) + \\
&+ y^2(y^2\frac{W_{021}}{\partial\lambda} + 2(z^2\frac{W_{012}}{\partial\lambda} - \frac{W_{011}}{\partial\lambda})) + z^2(z^2\frac{W_{003}}{\partial\lambda} + 2(x^2\frac{W_{102}}{\partial\lambda} - \frac{W_{002}}{\partial\lambda}))]
\end{aligned}
\tag{6.18}
$$

6.2 Appendix II: Elliptic Functions and Integrals

Elliptic integral of the first kind

The elliptic integral of the first kind F is defined as

$$F(\phi, k) = \int_0^{\phi} \frac{d\theta}{\sqrt{1 - k^2 \sin^2 \theta}}, \quad 0 < k^2 < 1 \tag{6.19}$$

where k is called *modulus* of this integral, while the quantity $K = K(k) = F(\pi/2, k)$ is called *complete elliptic integral of the first kind* [1].

Elliptic integral of the second kind

The elliptic integral of the second kind F is defined as

$$E(\phi, k) = \int_0^{\phi} \sqrt{1 - k^2 \sin^2 \theta} \tag{6.20}$$

and the quantity $E = E(k) = E(\pi/2, k)$ is called *complete elliptic integral of the second kind.*

The derivative of the complete elliptic integral of the first kind:

$$\frac{\mathrm{d}K(k)}{\mathrm{d}k} = \frac{E(k)}{k(1 - k^2)} - \frac{K(k)}{k} \tag{6.21}$$

while the derivative of the complete elliptic integral of the second kind:

$$\frac{\mathrm{d}E(k)}{\mathrm{d}k} = \frac{E(k) - K(k)}{k} \tag{6.22}$$

The elliptic functions are standard forms of elliptic functions. The three basic functions are denoted $\mathrm{cn}(u, k)$, $\mathrm{dn}(u, k)$, and $\mathrm{sn}(u, k)$. They arise from the inversion of the elliptic integral of the first kind:

$$u = F(\phi, k) = \int_0^{\phi} \frac{d\theta}{\sqrt{1 - k^2 \sin^2 \theta}}, \tag{6.23}$$

where $\phi = am(u, k) = am(u)$ is the Jacobi amplitude, giving $\phi = F^{-1}(u, k) = am(u, k)$. From this, it follows that

$$\begin{aligned} \sin\phi &= \sin(am(u, k)) = sn(u, k) & (6.24)\\ \cos\phi &= \cos(am(u, k)) = cn(u, k) & (6.25)\\ \sqrt{1 - k^2 \sin^2 \phi} &= \sqrt{1 - k^2 \sin^2(am(u, k))} = \mathrm{dn}(u, k) & (6.26) \end{aligned}$$

These functions are doubly periodic generalizations of the trigonometric functions satisfying:

$$\begin{aligned} sn(u, 0) &= \sin u & (6.27)\\ cn(u, 0) &= \cos u & (6.28)\\ dn(u, 0) &= 1 & (6.29) \end{aligned}$$

The standard Jacobi elliptic functions satisfy the identities:

$$sn^2u + cn^2u = 1 \tag{6.30}$$

$$k^2 sn^2u + dn^2u = 1 \tag{6.31}$$

$$k^2 cn^2u + k^{'2} = dn^2u \tag{6.32}$$

$$cn^2u + k^{'2} sn^2u = dn^2u. \tag{6.33}$$

where $k^{'} = \sqrt{1-k^2}$ is the complementary elliptic modulus of the complementary elliptic integral $K^{'} = K(k^{'}) = F(\pi/2, k^{'})$. The derivatives of the Jacobi elliptic functions are:

$$\frac{d\ snu}{du} = cnudnu \tag{6.34}$$

$$\frac{d\ cnu}{du} = -snudnu \tag{6.35}$$

$$\frac{d\ dnu}{du} = -k^2 snucnu \tag{6.36}$$

while the Fourier expands of these functions are:

$$sn(u,k) = \frac{2\pi}{kK}\sum_{s=0}^{\infty}\frac{q^{s+1/2}}{1-q^{2s+1}}\sin(\frac{\pi}{2K}(2s+1)u) \tag{6.37}$$

$$cn(u,k) = \frac{2\pi}{kK}\sum_{s=0}^{\infty}\frac{q^{s+1/2}}{1+q^{2s+1}}\sin(\frac{\pi}{2K}(2s+1)u) \tag{6.38}$$

where the parameter q is the elliptic *nome* and it is equal to:

$$q = e^{-\pi\frac{K^{'}}{K}}. \tag{6.39}$$

BIBLIOGRAPHY

[1] M. Abramowitz and I. Stegun. *Handbook of Mathematical Functions.* Dover, New York, 1965.

[2] Ch. Antonopoulos and T. Bountis. Stability of Simple Periodic Orbits and Chaos in a Fermi–Pasta–Ulam Lattice. *Physical Review E*, 73:056206, 2006.

[3] Ch. Antonopoulos, T. Bountis, and Ch. Skokos. Chaotic Dynamics of N–Degree of Freedom Hamiltonian Systems. *Int. J. Bif. Chaos*, 16(6):1–18, 2006.

[4] Ch. Antonopoulos, T. Bountis, and Ch. Skokos. Detecting Order and Chaos by the Linear Dependence Index. *ROMAI*, 2(2):1–13, 2006.

[5] Ch. Antonopoulos, T. Manos, and Ch. Skokos. SALI: An Efficient Indicator of Chaos with Application to 2 and 3 Degrees of Freedom Hamiltonian Systems. *Proceedings of the 1st International Conference: From Scientific Computing to Computational Engineering, Patras Univ. Press*, III, 2005. Editor: Tsahalis D. T.

[6] V.I. Arnol'd. *Mathematical Methodes of Classical Mechanics.* Graduate texts in Mathematics. New York: Springer, 1979.

[7] E. Athanassoula. Morphology of Bar Orbits. *MNRAS*, 259:328–344, 1992.

[8] E. Athanassoula. The Existence and Shapes of Dust Lanes in Galactic Bars. *MNRAS*, 259:345–364, 1992.

[9] E. Athanassoula, O. Bienayme, L. Martinet, and D. Pfenniger. Orbits as Building Blocks of a Barred Galaxy Model. *Astronomy and Astrophysics*, 127:349–360, 1983.

[10] R. Bario. Sensitivity tools vs. poincaré sections. *Chaos Solit. Fract.*, 25:711–726, 2005.

[11] R. Bario. Painting chaos: a gallery of sensitivity plots of classical problems. *Int. J. Bif. Chaos*, 16:2777–2798, 2006.

[12] G. Benettin, L. Galgani, A. Giorgilli, and J.M. Strelcyn. *Meccanica*, 15:9–20, March 1980.

[13] G. Benettin, L. Galgani, A. Giorgilli, and J.M. Strelcyn. *Meccanica*, 15:21–30, March 1980.

[14] G.P. Berman and F.M. Izrailev. The Fermi–Pasta–Ulam Problem: 50 Years of Progress. *Chaos*, 15:015104, 2005.

[15] J. Binney and S. Tremaine. *Galactic Dynamics*. Princeton: Princeton University Press, 1987.

[16] T. Bountis. *Non* L*inear* D*ifferential* E*quations (in greek)*. Pnevmatikos, 1997.

[17] T. Bountis and H. Segur. Logarithmic Singularities and Chaotic Behavior in Hamiltonian Systems. A.I.P. Conf. Proc., 1982. Editors: Tabor M. and Treves Y., 88, 279–292, A.I.P. New York.

[18] T. Bountis and Ch. Skokos. Application of the SALI Chaos Detection Method to Accelerator Mappings. *Nucl. Instr. Meth. Phys. Res. – Sect. A*, 561:173–179, 2006.

[19] R. Capuzzo-Dolcetta, L. Leccese, D. Merritt, and A. Vicari. Application of the SALI Chaos Detection Method to Accelerator Mappings. *The Astrophysical Journal*, 666:165–180, 2007.

[20] B.V. Chirikov. A Universal Instability of Many–Dimensional Oscillator Systems. *Physics Reports*, 52:263–379, 1979.

[21] H. Christodoulidi and T. Bountis. Low–Dimensional Quasiperiodic Motion in Hamiltonian Systems. *ROMAI*, 2(2):37, 2006.

[22] P. M. Cincotta and C. Simó. Simple Tools to Study Global Dynamics in Non–Axisymmetric Galactic Potentials – I. *Astron. Astroph. Suppl. Ser.*, 147:205–228, 2000.

[23] P.M. Cincotta, C.M. Giordano, and C. Simó. Phase space structure of multi–dimensional systems by means of the mean exponential growth factor of nearby orbits. *Physica D*, 182:151–178, 2003.

[24] G. Contopoulos. How Far Do Bars Extend. *Astronomy and Astrophysics*, 81:198–209, 1980.

[25] G. Contopoulos. *Order and Chaos in Dynamical Astronomy*. Springer Verlag, New York, 2002.

[26] G. Contopoulos and B. Barbanis. Lyapunov Characteristic Numbers and the Structure of Phase Space. *Astronomy and Astrophysics*, 222:329–343, 1989.

[27] G. Contopoulos, L. Galgani, and A. Giorgilli. On the Number of Isolating Integrals in Hamiltonian Systems. *Phys. Rev. A*, 18:1183–1189, 1978.

[28] G. Contopoulos, E. Grousousakou, and N. Voglis. Invariant Spectra in Hamiltonian Systems. *Astronomy and Astrophysics*, 304:374, 1995.

[29] G. Contopoulos and P. Magnenat. Simple Three–Dimensional Periodic Orbits in a Galactic–Type Potential. *Celest. Mech. Dyn. Astron.*, 37:387–414, 1985.

[30] G. Contopoulos and T. Papayannopoulos. Orbits in Weak and Strong Bars. *Astronomy and Astrophysics*, 92:33–46, 1980.

[31] G. Contopoulos and N. Voglis. Spectra of stretching numbers and helicity angles in dynamical systems. *Cel. Mech. Dyn. Astron.*, 64:1–20, 1996.

[32] G. Contopoulos and N. Voglis. A fast method for distinguishing between ordered and chaotic orbits. *Astronomy and Astrophysics*, 317:73–81, 1997.

[33] G. Contopoulos and N. Voglis. *Galaxies and Chaos.* Lecture notes in Physics, Springer Verlag, New York, 2003.

[34] R. Dvorak, B. Funk, F. Freistetter, and G. Contopoulos. New Insights on the Chaotic Behavior of the Standard Map. Proceedings of the 3rd Austrian-Hungarian Workshop on Trojans and related Topics, 2003. eds. F. Freistetter, R. Dvorak and B. Érdi.

[35] C. Efthymiopoulos, T. Bountis, and T. Manos. Explicit Algorithmic Construction of Polynomial First Integrals from the Painlevé–Laurent Series. *Regular and Chaotic Dynamics*, 9(3):385–398, 2004.

[36] A. El-Zant and I. Shlosman. Dark Halo Shapes and the Fate of Stellar Bars. *The Astronomical Journal*, 577:626–650, 2002.

[37] A. El-Zant and I. Shlosman. Long–lived Double-Barred Galaxies: Critical Mass and Length Scales. *The Astronomical Journal*, 595:L41–L44, 2003.

[38] E. Fermi, J. Pasta, and S. Ulam. Studes of nonlinear problems. *Los Alamos document LA – 1940*, 15, 1955. See also: “Nonlinear Wave Motion”, [1974], *Am. Math. Soc. Providence*, 15, Lectures in Appl. Math., ed. Newell A. C.

[39] N. M. Ferrers. *Quart. J Pure Appl. Math.*, 14:1, 1877.

[40] S. Flach and A. Gorbach. Discrete Breathers in Fermi–Pasta–Ulam Lattices. *Chaos*, 15:1, 2005.

[41] S. Flach, M.V. Ivanchenko, and O.I. Kanakov. q–Breathers in Fermi–Pasta–Ulam Chains: Existence, Localization and Stability. *Phys. Rev. E*, 73(3):036618, 2006.

[42] M. Fouchard, E. Lega, Ch. Froeschlé, and Cl. Froeschlé. On the Relationship Between Fast Lyapunov Indicator and Periodic Orbits for Continuous Flows. *Celest. Mech. Dyn. Astron.*, 83:205–222, 2002.

[43] F. Freistetter. Fractal dimensions as chaos indicators. *Cel. Mech. Dyn. Astron.*, 78:211–225, 2000.

[44] C. Froeschlé, Ch. Froeschlé, and E. Lohinger. Generalized Lyapunov Characteristic Indicators and Corresponding Kolmogorov like Entrophy of the Standard Mapping. *Celest. Mech. Dyn. Astron.*, 56:307–314, 1993.

[45] C. Froeschlé, R. Gonczi, and E. Lega. The fast lyapunov indicator: a simple tool to detect weak chaos. Application to the structure of the main asteroidal belt. *Planet. Space Sci.*, 45:881–886, 1997.

[46] C. Froeschlé and E. Lega. Twist Angles: a Method for Distinguishing Islands, Tori and Weak Chaotic Orbits. Comparison with Other Methods of Analysis. *Astronomy and Astrophysics*, 334:355–362, 1998.

[47] C. Froeschlé and E. Lega. On the structure of symplectic mappings. The fast lyapunov indicator: a very sensitive tool. *Cel. Mech. Dyn. Astron.*, 78:167–195, 2000.

[48] C. Froeschlé, E. Lega, and R. Gonczi. Fast Lyapunov Indicators. Application to Asteroidal Motion. *Celest. Mech. Dyn. Astron.*, 67:41–62, 1997.

[49] C. Gautero, J.L. anf Froeschlé. Linear stability of high-dimensional symplectic systemse. *Nuovo Cimento*, 105:657–666, 1990.

[50] G.A. Gottwald and I. Melbourne. A new test for chaos in deterministic systems. *Proc. Roy. Soc. London A*, 460:603–611, 2004.

[51] G.A. Gottwald and I. Melbourne. Testing for chaos in deterministic systems with noise. *Physica D*, 212:100–110, 2005.

[52] M. Guzzo, E. Lega, and C. Froeschlé. On the numerical detection of the effective stability of chaotic motions in quasi–integrable systems. *Physica D*, 163:1–25, 2002.

[53] M. Hénon. Exploration numérique du problème restreint. ii. masses égales, stabilité des orbites périodiques. *Annal Astrophysique*, 28:992, 1965.

[54] M. Hénon and C. Heiles. The Applicability of the Third Integral of Motion: Some Numerical Experiments. *The Astronomical Journal*, 69(1):73–79, 1964.

[55] J. Hietarinta. Direct Methods for the Search of the Second Invariant. *Physics Reports*, 147:87–154, 1987.

[56] J.E. Howard. Discrete virial theorem. *Cel. Mech. Dyn. Astron.*, 92:219–241, 1987.

[57] J.E. Howard and R.S. Mackay. Linear stability of symplectic maps. *Journal of Mathematical Physics*, 28(5):1036–1051, 1987.

[58] C. Kalapotharakos and N. Voglis. Global Dynamics in Self–Consistent Models of Elliptical Galaxies. *Cel. Mech. Dyn. Astron.*, 92(32), 2005.

[59] C. Kalapotharakos, N. Voglis, and G. Contopoulos. Chaos and Secular Evolution of Triaxial N–Body Dalactic Models due to an Imposed Central Mass. *MNRAS*, 428:905–923, 2004.

[60] C. Kalapotharakos, N. Voglis, and G. Contopoulos. Appropriate SCF Basis Sets for Orbital Studies of Galaxies and a ‘quantum–mechanical’ Method to Compute them. *MNRAS*, 383:971–988, 2008.

[61] H. Kantz and P. Grassberger. Internal Arnold Diffusion and Chaos Thresholds in Coupled Symplectic Maps. *J. Phys. A: Math. Gen*, 21:L127–133, 1988.

[62] G.I. Karanis and Ch.L. Vozikis. Fast detection of chaotic behavior in galactic potentials. *Astron. Nachr*, 329:403–412, 2008.

[63] T. Kotoulas and G. Voyatzis. Comparative study of the 2:3 and 3:4 resonant motion with Neptune: An application of symplectic mappings and low frequency analysis. *Cel. Mech. Dyn. Astron.*, 88:343–163, 2004.

[64] B. Kovács. About the efficiency of Fast Lyapunov Indicator surfaces and Small Alignment Indicator surfaces. *PADEU*, 19:221–236, 2007.

[65] J. Laskar. The Chaotic Motion of the Solar System – A Numerical Estimate of the Size of the Chaotic Zones. *Icarus*, 88:266–291, 1990.

[66] J. Laskar. Frequency Analysis for Multi–Dimensional Systems. Global Dynamics and Diffusion. *Physica D*, 67:257–281, 1993.

[67] J. Laskar. Introduction to frequency map analysis. In: Simó c. (ed.) Hamiltonian systems with three or more degrees of freedom. Plenum Press, 1999.

[68] J. Laskar, C. Froeschlé, and A. Celletti. The Measure of Chaos by the Numerical Analysis of the Fundamental Frequencies. Application to the Standard Mapping. *Physica D*, 56:253–269, 1992.

[69] E. Lega and C. Froeschlé. Comparison of convergence towards invariant distributions for rotation angles, twist angles and local lyapunov characteristic numbers. *Planet. Space Sci.*, 46:1525–1534, 1998.

[70] A. J. Lichtenberg and M. A. Lieberman. *Regular and Stochastic Motion.* Springer – Verlag, New York, 1991. 2^{nd} edition.

[71] E. Lohinger, C. Froeschlé, and R. Dvorak. Generalized Lyapunov Exponents Indicators in Hamiltonian Dynamics – An Application to a Double Star System. *Celest. Mech. Dyn. Astron.*, 56:315–322, 1993.

[72] G. Lukes-Gerakopoulos, N. Voglis, and C. Efthymiopoulos. The production of Tsallis entropy in the limit of weak chaos and a new indicator of chaoticity. *Physica A*, 387:1907–1925, 2008.

[73] W. Maciejewski and E. Athanassoula. Regular Motions in Double Bars - I. Double–Frequency Orbits and Loops. *MNRAS*, 380:999–1008, 2007.

[74] W. Maciejewski and E. Athanassoula. Regular Motions in Double Bars - II. Survey of Trajectories and 23 Models. *MNRAS*, 2008. in press.

[75] R.S. MacKay and J.D. Meiss. *Hamiltonian Dynamical Systems.* Adam Hilger, Bristol, 1987.

[76] T. Manos and E. Athanassoula. Detecting Chaotic and Ordered Motion in Barred Galaxies. Semaine de l'Astrophysique Francaise Journees de la SF2A, 2005. Edited by F. Casoli, T. Contini, J.M. Hameury and L. Pagani. Published by EdP-Sciences, Conference Series, 631–632.

[77] T. Manos and E. Athanassoula. Chaos and the Dynamical Evolution of Barred Galaxies. Proceedings of the 5th Marseille International Cosmology conference: The Fabulous Destiny of Galaxies: Bridging Past and Present, 2006. Edited by V. LeBrun, A. Mazure, S. Arnouts and D. Burgarella, Paris: Frontier Group, 541–542.

[78] T. Manos and E. Athanassoula. Barred galaxies: Studying the Chaotic and Ordered Nature of Orbits. Recent Advances in Astronomy and Astrofysics: 7th International Conference of the Hellenic Astronomical Society, 2007. Published by AIP Conference Proceedings, 848, 662–668.

[79] T. Manos and E. Athanassoula. Dynamical Study of 2D and 3D Barred Galaxy Models. *Proceedings of the international conference: Chaos in Astronomy*, 2008. Springer – Special Issue(in press).

[80] T. Manos, Ch. Skokos, E. Athanassoula, and T. Bountis. Studying the Global Dynamics of Conservative Dynamical Systems Using the SALI Chaos Detection Method. *Nonlinear Phenomena in Complex Systems*, 11(2):171–176, 2008.

[81] T. Manos, Ch. Skokos, and T. Bountis. Application of the Generalized Alignment Index (GALI) Method to the Dynamics of Multi–Dimensional Symplectic Maps. Proceedings of the international conference – Chaos, Complexity and Transport: Theory and Applications, 2008. World Scientific Publishing, 356–364.

[82] T. Manos, Ch. Skokos, E., and T. Bountis. Global Dynamics of Coupled Standard Maps. *Proceedings of the international conference: Chaos in Astronomy*, 2008. Springer – Special Issue(in press).

[83] M.L. Mateo. Dwarf galaxies of the local group. *Annual Review of Astronomy and Astrophysics*, 36, 1998.

[84] M. Miyamoto and R. Nagai. Three–Dimensional Models for the Distribution of Mass in Galaxies. *PASJ*, 27:533–543, 1975.

[85] R. Nagai and M. Miyamoto. A Family of Self–Graviatiting Stellar Systems with Axial Symmetry. *PASJ*, 28:1–17, 1976.

[86] J.A. Núñez, P.M. Cincotta, and F.C. Wachlin. Information entropy. An indicator of chaos. *Cel. Mech. Dyn. Astron.*, 64:43–53, 1996.

[87] P. Olver. *Applications of Lie Groups to Differential Equations (Graduate Texts in Mathematics)*. Springer Verlag, New York, 1993. 2nd edition.

[88] V.I. Oseledec. *Trans. Moscow Math. Soc.*, page 197, 1968.

[89] P. Panagopoulos, T. Bountis, and Ch. Skokos. Existence and Stability of Localized Oscillations in 1–Dimensional Lattices with Soft Spring and Hard Spring Potentials. *J. Vib. and Acoust.*, 126:520, 2004.

[90] T. Papayannopoulos and M. Petrou. On the Nature of Orbits in Realistic Bar Potentials. *Astronomy and Astrophysics*, 119:21, 1983.

[91] P.A. Patsis, C. Efthymiopoulos, G. Contopoulos, and N. Voglis. Dynamical spectra of barred galaxies. *Astronomy and Astrophysics,*, 326:493–500, 2002.

[92] P.A. Patsis, Ch. Skokos, and E. Athanassoula. Orbital Dynamics of Three–Dimensional Bars – III. Boxy/Peanut Edge-on Profiles. *MNRAS*, 337(2):578–596, 2002.

[93] P.A. Patsis, Ch. Skokos, and E. Athanassoula. On the 3D Dynamics and Morphology of Inner Rings. *MNRAS*, 346(4):1031–1040, 2003.

[94] P.A. Patsis, Ch. Skokos, and E. Athanassoula. Orbital Dynamics of Three–Dimensional Bars – IV. Boxy Isophotes in Face-on Views. *MNRAS*, 342(1), 2003.

[95] D. Pfenniger. The 3D Dynamics of Barred Galaxies. *Astronomy and Astrophysics*, 134(2):373–386, 1984.

[96] D. Pfenniger. The Velocity Fields of Barred Galaxies. *Astronomy and Astrophysics*, 141(1):171–188, 1984.

[97] H. Poincaré. Les Méthodes Nouvelles de la Mécanique Céleste. 1892. Paris: Gauthier – Villars.

[98] W. H. Press, S. A. Teukolsky, W. T. Vetterling, and B. P. Flannery. *Numerical* R*ecipes in* F*ortran 77:* T*he* A*rt of* S*cientific* C*omputing.* Cambridge: University Press, 1986. Second Edition, Volume 1 of Fortran Numerical Recipes.

[99] A. Ramani, B. Grammaticos, and T. Bountis. The Painlevé Property and Singularity Analysis of Integrable and Non–Integrable Systems. *Physics Reports (Review Section of Physics Letters)*, 180(3):159–245, 1989.

[100] Zs. Sándor, B. Érdi, and C. Efthymiopoulos. The phase space structure around l4 in the restricted three–body problem. *Celest. Mech. Dyn. Astron.*, 78:113–123, 2000.

[101] Zs. Sándor, B. Érdi, A. Széll, and B. Funk. The Relative Lyapunov Indicator: An Efficient Method of Chaos Detection. *Celest. Mech. Dyn. Astron.*, 90(1):127–138, 2004.

[102] I.V. Sideris. Characterization of chaos: A new, fast and effective measure. *In: Gottesman ST, Buchler J–R (eds.) Nonlinear Dynamics in Astronomy and Astrophysics, Annals of the New York Academy of Science, The New York Academy of Sciences*, 1045:79, 2005.

[103] I.V. Sideris. Measure of orbital stickiness and chaos strength. *Phys. Rev. E*, page 066217, 2006.

[104] Ch. Skokos. Alignment Indices: A New, Simple Method for Determining the Ordered or Chaotic Nature of Orbits. *J. Phys. A*, 34:10029–10043, 2001.

[105] Ch. Skokos. On the stability of periodic orbits of high dimensional autonomous hamiltonian systems. *Physica D*, 159(3–4), 2001.

[106] Ch. Skokos, Ch. Antonopoulos, and T. Bountis. Geometrical Properties of Local Dynamics in Hamiltonian Systems: the Generalized Alignment Index (GALI) Method. *Physica D*, 231(30):30–54, 2007.

[107] Ch. Skokos, Ch. Antonopoulos, and T. Bountis. Detecting Chaos, Determining the Dimensions of Tori and Predicting Slow Diffusion in Fermi–Pasta–Ulam Lattices by the Generalized Alignment Index Method. *European Physical Journal – Special Topics . (in press), nlin.CD/0802.1646*, 2008.

[108] Ch. Skokos, Ch. Antonopoulos, T. Bountis, and Vrahatis M.N. Detecting Order and Chaos in Hamiltonian Systems by the SALI Method. *J. Phys. A*, 37:6269–6284, 2004.

[109] Ch. Skokos, Ch. Antonopoulos, T. Bountis, and M.N. Vrahatis. How does the Smaller Alignment Index (SALI) Distinguish Order from Chaos? *Prog. Theor. Phys. Supp.*, 150:439–443, 2003.

[110] Ch. Skokos, Ch. Antonopoulos, T. Bountis, and M.N. Vrahatis. Smaller Alignment Index (SALI): Determining the Ordered or Chaotic Nature of Orbits in Conservative Dynamical Systems. Proceedings of the Conference Libration Point Orbits and Applications, 2003. Editors: Gomez G. Lo M. W. and Masdemont J. J.

[111] Ch. Skokos, Ch. Antonopoulos, T. Bountis, and M.N. Vrahatis. Smaller Alignment Index (SALI): Determining the Ordered or Chaotic Nature of Orbits in Conservative Dynamical Systems. Proceedings of the 4th GRACM, 2003. Editor: D. T. Tsahalis, IV, 1496.

[112] Ch. Skokos, P.A. Patsis, and E. Athanassoula. On the 3d Dynamics and Morphology of Inner Rings – II. *MNRAS*, 333(4):861–870, 2002.

[113] Ch. Skokos, P.A. Patsis, and E. Athanassoula. On the 3D Dynamics and Morphology of Inner Rings – I. *MNRAS*, 333(4):847–860, 2002.

[114] Á. Süli. Motion indicators in the 2D standard map. *PADEU*, 17:47–62, 2006.

[115] Á. Süli. Speed and efficiency of chaos detection methods. In: Proceedings of the 4th Austrian Hungarian workshop on Celestial Mechanics, Süli, Á, Freistetter, F., Pál, A. (eds.), Publications of the Astronomy Department of the Eötvös University, 2006.

[116] A. Széll, B. Érdi, Zs. Sándor, and B. Steves. *MNRAS*, 347:380–388, 2004.

[117] P.J. Teuben and R.H. Sanders. Dynamical Rules for Brred Spiral Galaxies. *MNRAS*, 212:257–273, 1985.

[118] N. Voglis and G. Contopoulos. Invariant spectra of orbits in dynamical systems. *J. Phys. A*, 27:4899–4909, 1994.

[119] N. Voglis, G. Contopoulos, and C. Efthymiopoulos. Detection of Ordered and Chaotic Motion Using the Dynamical Spectra. *Phys. Rev. E*, 57(1):372–377, 1998.

[120] N. Voglis, G. Contopoulos, and C. Efthymiopoulos. Method for distinguishing between ordered and chaotic orbits in four–dimensional maps. *Phys. Rev. E*, 57:372–377, 1998.

[121] N. Voglis, G. Contopoulos, and C. Efthymiopoulos. Detection of Ordered and Chaotic Motion Using the Dynamical Spectra. *Celestial Mechanics and Dynamical Astronomy*, 73:211–220, 1999.

[122] N. Voglis, M. Harsoula, and G. Contopoulos. Orbital Structure in Barred Galaxies. *MNRAS*, 381(2):757–770, 2007.

[123] N. Voglis, C. Kalapotharakos, and I. Stavropoulos. Mass Components in Ordered and in Chaotic Motion in Galactic N–Body Models. *MNRAS*, 337(2):619–630, 2002.

[124] N. Voglis, I. Stavropoulos, and C. Kalapotharakos. Chaotic Motion and Spiral Structure in Self–Consistent Models of Rotating Galaxies. *MNRAS*, 372(2):901–922, 2006.

[125] G. Voyatzis and S. Ichtiaroglou. On the spectral analysis of trajectories in near–integrable Hamiltonian systems. *J. Phys. A*, 25:5931–5943, 1992.

[126] Ch.L. Vozikis, H. Varvoglis, and K. Tsiganis. The power spectrum of geodesic divergences as an early detector of chaotic motion. *Astronomy and Astrophysics*, 359:386–396, 2000.

[127] E.T. Whittaker. *Analytical Foundations of Celestial Mechanics*. Princeton University, Press, Princeton Ney Jersey, 1947.

[128] Y. Zou, D. Pazó, M.C. Romano, M. Thiel, and J. Kurths. Distinguishing quasiperiodic dynamics from chaos in short–time series. *Phys. Rev. E*, 76:016210, 2007.

[129] Y. Zou, M. Thiel, M.C. Romano, and J. Kurths. Characterization of stickiness by means of recurrence. *Chaos*, 17:043101, 2007.

LIST OF FIGURES